INVESTIGATION OF THERMAL CONVERSION PROCESS TECHNOLOGY USING BIOMASS WASTE AND BIO-PRODUCT APPLICATIONS

A Dissertation

by

HYUNGSEOK NAM

Submitted to the Office of Graduate and Professional Studies of
Texas A&M University
in partial fulfillment of the requirements for the degree of

DOCTOR OF PHILOSOPHY

Chair of Committee,	Sergio C. Capareda
Committee Members,	Calvin B. Parnell
	Sandun D. Fernando
	Mahmoud M. El-Halwagi
Head of Department,	Stephen W. Searcy

August 2016

Major Subject: Biological and Agricultural Engineering

ABSTRACT

The increasing demand for energy, the consequential depletion of fossil fuels, and the generation of waste materials has led to an interest in renewable and clean energy. In this work, thermochemical conversion processes of torrefaction, pyrolysis, and gasification were investigated to convert the agricultural and municipal wastes into three solid, liquid, and gas products. Also, the utilization of those products was studied to find the value added products.

Dairy manure was selected to be used as a thermochemical fuel source after removing the moisture content and sand content. The optimal initial manure condition was determined for developing a pilot-scale manure handling system. Also, a slagging and bed agglomeration prediction study indicated a low potential of ash. A fluidized bed gasification study using the processed dairy manure was performed, and the constructed empirical equations for syngas compositions were developed to predict the quality of syngas. A steam gasification was also conducted, and showed a higher H_2 concentration compared to air gasification at the same operating condition. The CO_2 gas removal from syngas was also successfully conducted.

Torrefaction with two wastes was conducted to observe the effects of temperatures and times on the yields and characteristics of products. The biomass waste processed at the highest temperature (290 ^oC) was converted into a comparable fuel source, showing the highest heating value of 28.6 MJ/kg. A pyrolysis study using rice straw was conducted using auger, batch, and fluidized bed reactors to compare the

product yields and their properties. The slow process resulted in higher yields of bio-char (45 – 48 %), while the fast process produced a larger quantity of bio-oil (43%). The heating value of bio-oils from slow pyrolysis showed a relatively higher HHV than fast pyrolysis.

The pyrolysis products of bio-char and bio-oil were further studied. First, the bio-char pyrolyzed was chemically activated. The highest surface area was determined as 1330 m^2/g. Then, the adsorption and electrical performance of the activated carbon were evaluated. The activated carbon removed almost 95% of the pharmaceutical pollutants. The specific capacitance property of the carbon was obtained as 93 F/g. Last, nickel impregnated on the developed activated carbon was used to upgrade vacuum distilled microalgae pyrolytic bio-oil.

DEDICATION

This work is dedicated to my lovely wife, Jihye Han, who supported and encouraged me during my stay in College Station. To my father and mother, Dr. Ki-Woo Nam and Jung-Hee Park, and my mother-in-law, Myeong-Ok Won, for their love, guidance and continuous support through my vital educational years. To my two boys, David Leehyun Nam and Soohyun Joshua Nam, for giving me the inspiration to succeed.

ACKNOWLEDGEMENTS

I would like to thank my sincere gratitude to all who made this dissertation possible. I would express special thanks to my distinguished major advisor, Dr. Sergio C. Capareda, and the committee members, Dr. Calvin B. Parnell, Dr. Sandun Fernando, and Dr. Mahmoud M. El-Halwagi for your continuous support, patience, guidance, and many comments throughout my Ph.D. period. I would like to extend my gratitude to a visiting professor from CQ University, Dr. Nanjappa Ashwath, for his guidance and inspiring ideas. In addition, I wish to express my gratitude to Dr. Amado L. Maglinao for all of his help and guidance on most of experimental projects. I also appreciate Texas AgriLife Research, USDA-ARS, and OGAPS for the research funding and fellowship. Thanks to the BAEN department faculty and staff for the generous assistance.

I would like to thank my lab friends in the BETA lab for their helps, instructions, and helpful comments and encouragements, Dr. Jewel Capunitan, Dr. Bjorn Santos, Dr. Monet Maguyon, Dr. Jersson Placido, Jinjuta Kongkasawan, Julius Choi, Butch Bataller, Alexander Ido, Dr. Joel Alcaraz, Seaborn Carter, Mari Rowena Tanquilut, Wency Carmelo, Keynty B. Magtoto, David A. Rodriguez, Toni-An Salcedo, and Divine Genuino. Thank you all the student workers who worked together for reactor fabrication and miscellaneous works during my Ph.D. studies, David Lacey, Ryan Kendrick, William Hartlage, Caleb Groves, John Padgett, and Amanda Bast. Also, I want to express my gratitude to undergrad researchers, Changkyu Kim and Thomas Marchetti for their assistances. Thank you very much to all. I wouldn't complete my Ph.D. studies without

all of you supports and helps. For the last and not least, I would love to thank my English teacher, Diana Vance, for helping the completion of my published papers and dissertation.

Finally, thanks to my family, both the Nam and Han families, for their encouragement and the unconditional love. Special thanks to my lovely wife and two boys for inspiring me to make the necessary effort to bring this dissertation to fruition.

TABLE OF CONTENTS

Page

LIST OF FIGURES

Page

LIST OF TABLES

Page

1. INTRODUCTION

The Second Industrial Revolution in the mid-nineteenth century spurred invention of the new combustion engine and the assembly line both requiring fossil fuels, which are still the main source of energy [1]. The increasing use of energy and the consequences of the depletion of fossil fuels and global environmental problems caused people to show an interest in renewable energy for commercial production. Biomass as an alternative and sustainable energy source is the fourth largest energy source (14%) in the world [2]. Several advantages of using biomass as an energy source are lower environmental impact, sustainability, CO_2 neutral, and a low sulfur content resource. Additionally, it produces less NO_x emissions than fossil fuel power generation. Even negative CO_2 emissions from the thermochemical process could be achieved if plants using photosynthesis consume the released CO_2 from the process [3]. Biomass wastes used for bioenergy industry include a group of fast-growing biomass (switchgrass), agricultural residues or by-products (straw, and stalk), animal manure (sludge, and manure), and industry/residential wastes (MSW), which are considered as clean energy sources. On the other hand, problems with most biomasses are low energy density, hydroscopic properties, low density, and seasonal production [4]. Therefore, both the advantages and problems need to be considered when selecting a potential biomass feedstock for bioenergy production. For the last few decades, several thermochemical conversion techniques such as torrefaction, pyrolysis, and gasification were developed to convert biomass waste into different types of energy.

1.1. Research Plan

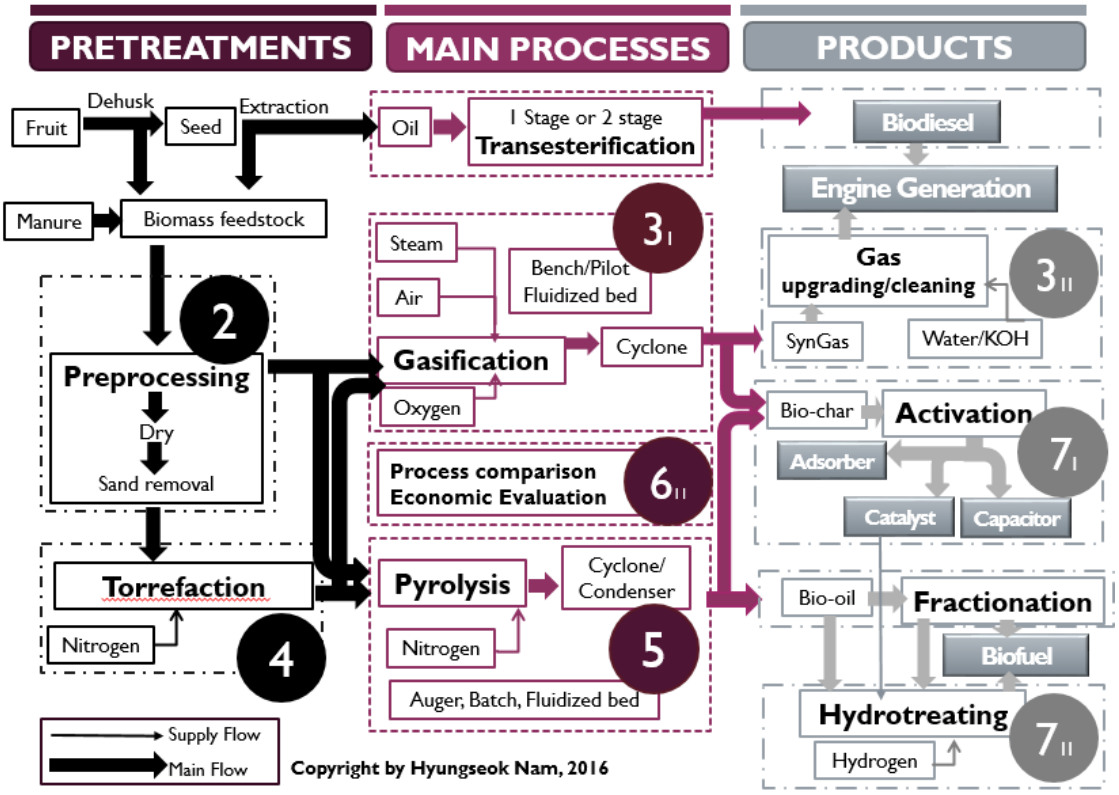

Figure 1.1. Energy conversion process from biomass wastes.

This research is a comprehensive assessment of thermochemical conversion processes through different type of reactors using various feedstock. A schematic diagram of the experimental design is shown in Figure 1.1. The targeted biomass of the diagram is dairy manure or fruit from oil crops, which contains a seed and husk. As a thermal conversion process study, the torrefaction (Chapter 4), gasification (Chapter 3), and pyrolysis (Chapter 5) studies was conducted with its product utilizations (Chapter 7) of developing activated carbons for a capacitor, adsorption material, and catalyst used

for distilled bio-oil upgrading. Further study on pilot-scale dairy manure handling process (Chapter 2), product comparison and economic evaluation (Chapter 6) of gasification were also investigated.

The overall goal of the current study is to understand the different processes using different biomass wastes, and their product properties and applications. A specific objectives were aimed to:

1. Design and develop the pilot-scale process to upgrade sand mixed and low heating value dairy manure for a thermal conversion, and its complete fuel analysis for a thermal conversion process;
2. Determine the air-enriched and steam gasification optimum conditions of oxygen, temperature, and fuel-to-air ratio (equivalence ratio);
3. Evaluate the effect of lignocellulosic wastes, temperature and time parameters on the improved properties through torrefaction process;
4. Evaluate the differences of reactor types of auger, batch, and fluidized bed reactors for pyrolysis process, and analyze and compare the product yields and properties;
5. Compare the product mass and energy yields, and their properties from different wastes, reactors, and process methods of pyrolysis and gasification;
6. Investigate the application of char and bio-oil products for activated carbon, electrode material, and catalyst used for vacuum distilled bio-oil.

1.2. Literature Review

1.2.1. A review of various biomass feedstock

Rice and cotton as representative biomasses are two major agricultural products in China and India [5]. Along with the large production, 727 million tons of rice straw was globally produced in 2009 [6]. Even though rice straw can be used for bedding, feed, and compost, it is left on the ground or burned in many underdeveloped or developing countries. Furthermore, its fibrous property causes difficulty when feeding the straw into thermochemical reactors [7]. Many alternative uses of rice straw wastes have been reported recently [8]. Rice straw has excellent potential for soil erosion control, sediment traps, and soil improvement. The straw prevents water erosion and soil loss by retaining moisture, reducing evaporation, controlling soil temperature, preserving fertilizer, and providing useful soil organic matter as it decomposes. Grantz et al. [9] demonstrated that the use of recalcitrant mulch, such as straw, improved the growth of plants in arid and semiarid lands. Also, covering soil with a thick layer of straw helps in weed control. Other alternative applications of rice straw include paper and composite materials. According to FAO, 15.6 million tons of non-wood fibers were used for paper and pulp production in the world. Interestingly, the production of rice straw exceeds its use every year. A large amount of rice straw in many underdeveloped or developing countries has often been left as is or burned in the field. The applications mentioned above still produce other types of wastes. On the other hand, the annual worldwide production of cotton is about 24 million tons [10] and the annual cotton residue in the U.S. exceeds 5.6 million tons [11] . Burying the cotton residue is prohibited by law in

the U.S. in order to manage the overwintering insects and diseases, such as boll weevils and pink bollworms.

Microalgae is a potential biofuel source that many researchers have focused on due to 1) its fast growth rate (a 5 to 30 times higher production rate than oil crops [12]) and a high lipid content of over 60% by weight of lignocellulosic biomass [13]. As microalgae covers extensive areas of lakes in many countries, pyrolysis of microalgae can be an alternative solution for improving the ecological environment.

The Beauty Leaf Tree (BLT) is a wild species that grows in a variety of soils and environmental conditions in tropical areas all over the world [14]. The BLT has inedible fruit containing a seed and a husk. Although oil from the seed has been used for medicinal purposes, the husk and seed cake are considered waste material. The oil from BLT fruit for bio-diesel has been researched many times [15-17] while the bio-oil from BLT plant has rarely been studied [18].

Dairy manure has been regarded as an important protein source for crop production for many years [19]. However, large stall cow feedlots and dairies are widely known as major pollution sources of air, soil, and water. The concentrated dairy farms produce more daily dairy manure wastes than are needed, even though this waste has been regarded as an important fertilizer source for crop production for many years [19]. However, with limited land area, the wastes overload the land with excess phosphorus, which is detrimental to agricultural production and has a negative impact on the land itself [20]. The number of dairy cows in the United States was reported to be more than 9 million head in 2013 [21]. The states with the largest number of dairy cows are

California (19%), Wisconsin (14%), New York (7%), Idaho (6%), Pennsylvania (6%), and Texas (5%). This gives a rough idea of the source of the total production of dairy manure per year at 23 million solid dry metric tons in the USA and 1.4 million dry metric tons in Texas [22].

1.2.2. Structural compositions of lignocellulose biomass

(a)

(b)

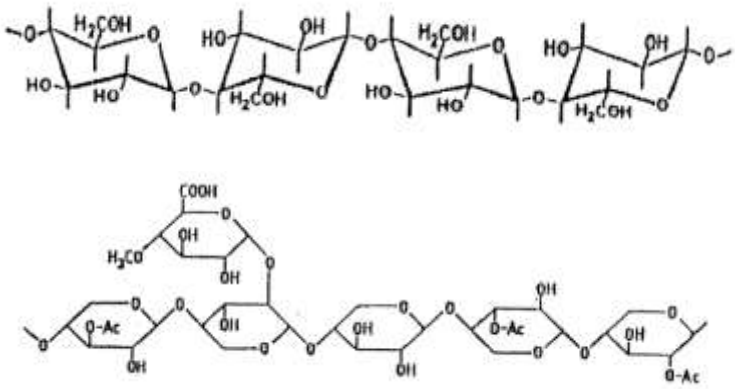

Figure 1.2. Chemical structure of (a) cellulose and (b) hemicellulose [24].

The main structural chemical components of the lignocellulose biomass consist of cellulose, hemicellulose, and lignin that make up 60 -90 wt.% of biomass [23]. The schematic chemical structures of cellulose and hemicellulose are shown in Figure 1.2. Other chemicals comprising biomass wastes include extractives, protein, and ash. The most abundant composition of biomass is normally cellulose, which is a crystalline glucose polymer $(C_6H_{10}O_5)_n$. The next most abundant composition is hemicellulose or lignin. Short branched chains of glucose and other sugar molecules $(C_5H_8O_4)_n$ is referred

to as hemicellulose, which is an amorphous polymer with various sugar composition of xylose, arabinose, galactose, mannose, and glucose. Lignin is a highly branched aromatic polymer that normally comprises 10 – 25wt.% of biomass [23]. The extractives, which can be soluble in water and ethanol, contain resins, fats, acids, phenolic, and other chemicals [24].

It has been known that the ranges of the decomposing temperature of hemicellulose, cellulose and lignin are 200 – 300^{o}C, 300 – 400^{o}C, and over 200^{o}C, respectively, as it can be seen in Figure 1.3 [25,26]. Cellulose and hemicellulose structure abruptly decompose in short ranges of temperatures, while lignin structure reacts slowly over the large temperature profile. Based on this characteristics of chemical structures, the thermochemical processes of torrefaction or pyrolysis can be selectively applied to produce products that are more valuable.

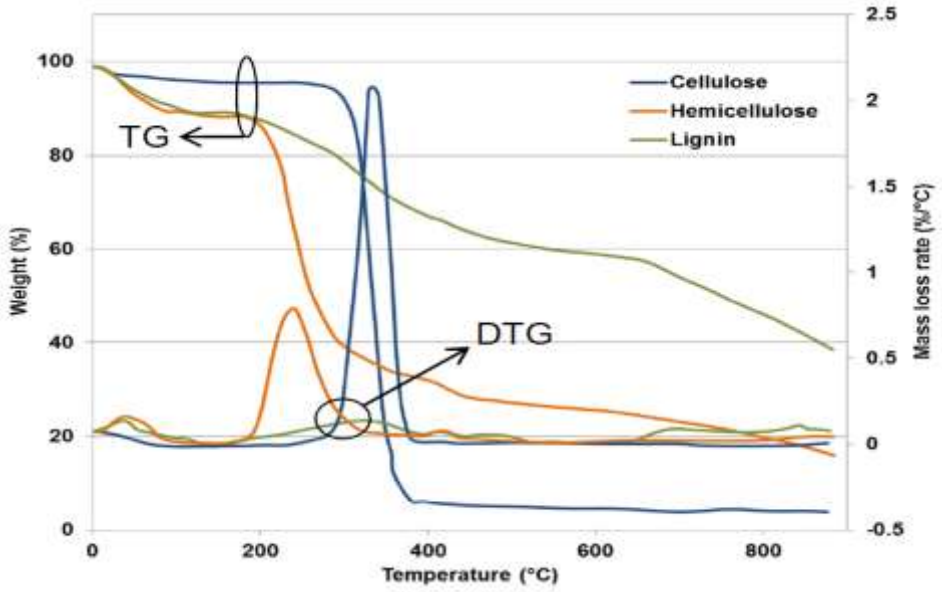

Figure 1.3. Weight loss of lignocellulose biomass structure compositions [25].

1.2.3. Thermochemical processes

Thermochemical technology has three big categories: pyrolysis (or torrefaction), gasification, and combustion, which are available for any solid wastes. Different products can be obtained depending on the process the material goes through as shown in Table 1.1. Combustion based power plants are generally used to burn the carbonaceous feedstock to create heat for steam power generation, while gasification produces synthesis gas after a complex series of reactions. Five major gas reactions are water-gas, water-gas shift, Boudouard, hydrogasification reactions and methanation [27]. The syngas from gasification is relatively easier to clean up than the flue gas from the combustion process. The pyrolysis process employing energy from syngas is mainly used for producing bio-oil and bio-char products. These products can be converted into more valuable chemicals and char based products. As a pretreatment of biomass, torrefaction has also gained attentions in recent years. A combination of these technologies would not just increase the efficiency of each process but also help in dealing with the many different types of solid wastes on earth.

Table 1.1. Thermochemical process and product utilization

Pyrolysis		Gasification	Combustion
Torrefaction	Pyrolysis		
• 0% air • 200 – 320°C • Mostly biomass	• 0% air • 300 – 600°C • Most wastes	• Partial air (30%) • 600°C – over 1000°C • Most wastes and coal (<10% moisture)	• 100% air • 800°C and over • Coal (low ash)
Char	**Char, Oil, Gas**	**Syngas**	**Heat**
⇩	⇩	⇩	⇩
• Soil amendment • Solid fuel	• Extraction • Upgrading • Boiler/engine for power	• Boiler/engine for power • Fisher Trosch to methanol	• Boiler for power

Gasification

Gasification is another thermochemical conversion process in an oxygen deficient environment at high temperatures. Almost all the organic biomass or waste can be used in this process because of its high temperature. The parameters of the gasification process are usually temperature and equivalence ratio in addition to reactor types and gasifying agents (steam, air, and oxygen) [28]. Four reaction stages were proposed to explain the gasification process: drying, volatilization, combustion, and reduction [29]. The major product is combustible synthesis gas (syngas) consisting mainly of carbon monoxide, hydrogen, traces of methane, and other hydrocarbon gases [30]. Air gasification normally produces a low heating value gas from 3 to 7 MJ/m^3 while oxygen gasification can increase the heating value from 10 to 15 MJ/m^3 [27]. However, biomass waste gasification must deal with drawbacks of biomass feedstock (high ash, moisture, and size reduction). The system has specific parameter conditions for each waste feedstock with regard to chemical and physical properties such as different particle size.

The parameters of the gasification process are usually temperature and equivalence ratio in addition to reactor types and gasifying agents (steam, air, and oxygen) [28]. Four reaction stages were proposed to explain the gasification process: drying, volatilization, combustion, and reduction [29]. Air gasification normally produces a low heating value gas from 4 to 7 MJ/m^3 while oxygen gasification can increase the heating value from 10 to 18 MJ/m^3 [31]. However, biomass waste gasification must deal with drawbacks. The system has specific parameter conditions for

each waste feedstock with regard to chemical and physical properties such as different particle size.

Le Charelier's principle [32] suggests that a higher temperature is supported from the exothermic reactions of reactants, and it also affects on the endothermic reactions of products. Five major gas chemical reactions as shown in Equation (1.1 – 1.5) are differently synthesized depending on the operating conditions [27]. The combination of water-gas reaction and Boudouard reaction can be express to the water gas shift reaction Equation (1.2) [27,33]. At a higher temperature, the carbon dioxide gas would reach a steady phase and decrease due to the water-gas shift and dry reforming reactions of Equation (1.2 and 1.6) [34]. Also, some increase of hydrogen concentration can be caused from the endothermic reaction of carbonization reaction of Equation (1.7).

Water-gas reaction	$C + H_2O \leftrightarrow CO + H_2$	+131 MJ/kmol	(1.1)
Water-gas shift reaction	$CO+H_2O \leftrightarrow CO_2+ H_2$	-41MJ/kmol	(1.2)
Boudouard reaction	$C +CO_2 \leftrightarrow 2CO$	+172 MJ/kmol	(1.3)
Hydrogasification	$C + 2H_2 \leftrightarrow CH_4$	+75MJ/kmol	(1.4)
Methanation	$CO + 3H_2 \leftrightarrow CH_4 + H_2O$	-227 MJ/kmol	(1.5)
Dry reforming	$CH_4 + CO_2 \leftrightarrow 2CO +2H_2$	-793MJ/kmol	(1.6)
Carbonization	$C_nH_m \rightarrow nC + m/2H_2$	Endothermic	(1.7)

The principal reactor types used for biomass gasification systems are fixed bed (down and up draft) and fluidized bed. A steam co-gasification process was conducted

with a mixture of coal-petcoke-biomass (45-45-10%) at different pressure (0.5 – 0.2 MPa) and temperature conditions (1123 – 1273 K) [35]. Temperature and oxygen concentration were determined to be the most influential variables on the gas products. An air-blown pilot-scale fluidized bed reactor was used to gasify rice husk biomass based on the response surface methodology (RSM) [36]. The highest heating value of syngas was 3.78 MJ/Nm^3 with the cold gas efficiency of 40%, which was obtained at an optimum condition of ER=0.24 and an air velocity of 0.19 m/s. A downdraft gasifier was investigated to understand the effects of operating conditions on the syngas using an oil palm frond feedstock [37]. A pilot scale fluidized bed gasifier was used with sorghum, cotton gin trash and cattle manure, which produced on average 4.2 MJ/Nm^3 [38]. The preheated gasifying air at 500 ^oC improved the syngas quality of H_2, CO, and CH_4 by 10, 21, and 25%, respectively, while the use of 20% wet biomass reduced by almost half the quality of syngas compared to the use of 10% wet biomass.

The power is generated when the gas is injected into a power generator including internal combustion engines. The first commercial-scale Integrated Gasification Combined Cycle (IGCC) plant using coal in the United States began operation in the 1990s [39]. The SO_x and NO_x emissions are lower and the efficiency is higher compared to those from the coal combustion-based power plants. Also, the production of CO_2 can be cut by 40 % or more per unit of output at the IGCC plant compared to a conventional coal power plant [40].

Pyrolysis and torrefaction

Pyrolysis has gained interest in recent years due to the energy rich useful products of bio-oil and bio-char. The thermochemical process is done with a temperature range from 200^{o}C to 600^{o}C and a condition of no oxygen. Pyrolysis processes are categorized into three types according to the heat transfer rate: slow, medium, and fast. The rate of thermal decomposition that determines the pyrolysis product changes depend on conditions such as feedstock type, temperature, residence time, reactor type, and heat transfer rate. Many studies used the chemical composition of a lignocellulosic biomass to understand the relationships of mass and energy yields with such conditions as temperature, residence time, moisture, and input gas type [41-44]. It is widely known that bio-oil is the key product from the pyrolysis process. However, bio-char is also considered as the main product in other applications such as soil composter, water purifier, and biocatalyst. Especially, the bio-oil product, composed of hundreds of oxygenated compounds, has many potential uses as alternative fuels, chemicals, heat, and power. Compared to commercial fossil fuels, bio-oils are usually much denser and viscous. Therefore, bio-oil upgrading to remove the defects is significantly important for commercial use.

Several types of reactors were used in the pyrolysis process; an auger type [45-48], a batch type [49-52], a fluidized bed type [38,53,54], and a microwave type reactor [55-58]. A fixed bed batch reactor was used to investigate the effects of independent variables of temperature, particle size, nitrogen flow rate, and steam velocity on the pyrolysis products. According to Pütün et al. [49], the maximum yield of bio-oil

(35.86%) was through steam pyrolysis. The conditions for maximum bio-oil yields were a temperature of 824 K, a particle size of 0.435<D<0.85 mm, and a nitrogen gas flow of 400 ml/min. Ingram et al. [48] determined that the bio-oil heating value from pine and oak wood from the auger reactor was at a range of 18 – 22 MJ/kg. The product mass yields of pine woodchips from the auger pyrolysis reactor were 57% liquid and 26% solid [45]. Sadaka et al. [46] used the auger reactor for gasification of agricultural residues. The effect of temperature was tested to produce gas to explore the possibility of finding a fuel source for an on-site facility. Fast pyrolysis in a fluidized bed reactor was used to process rice straw and rice husk at temperatures of 375 – 500ºC [54]. The highest mass yield of bio-oil from rice straw and rice husk was obtained at 500ºC while the highest char yield was achieved at 375ºC. The fluidized bed reactor was also used for gasification process to convert wastes of sorghum, cotton, gin trash, and dairy manure [38,53]. The microwave reactor was also used to pyrolyze rice straw at 237 – 423ºC [55]. Duman et al. [59] used cherry seed to compare slow and fast pyrolysis. The maximum bio-oil yield at 500ºC was found to be about 44 wt% for the fast process and about 15 wt% for the slow pyrolysis.

The torrefaction process can be defined as when the temperature range is 200 ºC to 320 ºC, which is sometimes referred to as mild-pyrolysis. The main product after the torrefaction process is solid products. Torrefaction is considered a pretreatment that helps to reduce the drawbacks of lignocellulosic biomass. Several improvements after the torrefaction treatment are an increased energy density and hydrophobic properties, which alleviate storage problems. Moreover, uniformed product quality and improved

grindability help reduce the cost of processing biomass feedstock for another combustion, pyrolysis, or the gasification process [41,42,60]. Through the torrefaction process, most of the hemicellulose, one of the main constituents of biomass, decomposes into light volatile products of water, acids, and lightweight chemicals [61].

The raw biomass feedstock loses 30-70% of its weight by maintaining energy over 60%, depending on the conditions of temperature, residence time, and moisture content [4,42,51]. This influences the augmentation of the heating value and energy density as the amount of atomic carbon increases with the decrease of atomic hydrogen and oxygen, which makes a fibrous biomass a suitable feedstock for a thermochemical energy generation such as pyrolysis, gasification and co-firing [42-44,62,63]. A previous study [43] verified that an increased mass and energy yield [64] of char from the pyrolysis of torrefied straws were obtained while the yield of volatiles decreased after pyrolysis of torrefied corn stalk and cotton stalk using a fixed bed reactor.

1.2.4. Bio-char product applications

The potential applications of char has been investigated and it can be used for combustible energy material, a soil amendment, and activated carbon. The value of activated carbon can vary based on how the carbon is used, such as for a metal catalyst support, a gas or liquid purification media, or an electrode material for energy storage. The following sub-sections of each application explain in detail with some previous studies.

Activation of carbons

Activated carbon is defined as a porous carbon with BET (Brunauer-Emmett-Teller) areas between 5 to over 3000 m^2/g [65]. The activated carbon properties of surface area, pore size, etc. is decided depending on the applications. The pore sizes of micropore (< 20 Å), mesopore (20 < width < 500 Å), and macropore (> 500 Å) are, in most cases, a standard property for determining the use of carbon. Two activation production methods, chemical and physical, have been introduced and used [66-68]. First, physical activation involves oxidizing agents of air, carbon dioxide, and/or water as steam. The pores on the targeted carbon are produced through endothermic and exothermic reactions producing CO and CO_2 gases. The second method is a chemical activation produced at a high temperature under inert gas with chemical etching agents. As higher porosity and controllable porous property can be achieved from the chemical method, it is mostly applied in the mass production of activated carbon.

The chemical activation method requires a carbonization or pyrolysis process to be impregnated with etching precursor agents. The activating chemical agent of $ZnCl_2$ (zinc chloride) and H_3PO_4 (phosphoric acid) was a preferred reagent before, and its uses have declined in Europe and North America [69]. Various activation process methods were reported from previous studies. Baseri el al. [70] prepared the activated carbon in nine different methods of direct pyrolysis, Na_2SO_4, H_3PO_4, $ZnCl_2$, KOH, HCl, H_2SO_4, dolomite ($CaMg(CO_3)_2$), and mixtures of H_2SO_4 and H_2O_2 using *Thevetia peruviana* for the purpose of removing dyes from waste water. The top four highest surface areas were obtained from H_3PO_4, $ZnCl_2$, KOH, and H_2SO_4, which have been used in many other

studies. Among other activating agents, KOH has been frequently used as it helps produce a defined micropore size distribution with a high surface area [66]. ACs, AX21 and Maxsorb are representative commercial KOH based activated carbons from fossil-based carbon. The KOH activation reaction mechanism was introduced from previous studies and found to be the most effective agent [66,71,72]. The main products during KOH activation below 700 ^{o}C were H_2, H_2O, CO, CO_2, K_2O (potassium oxide), and K_2CO_3 (potassium carbonate). With an activation temperature above 700 ^{o}C, another product of metallic K was formed as shown in Equation (1.8 – 1.12). Initially, the K_2O and K_2CO_3 at 400 ^{o}C and below 700 ^{o}C are formed through Equation (1.8 – 1.10) combining with two reactions, water-gas ($C + H_2O \rightarrow CO + H_2$) and water-gas shift ($CO + H_2O \rightarrow CO_2 + H_2$), that mainly produce CO, CO_2 and H_2 gas. After the complete consumption of KOH at 600 ^{o}C, the produced K_2O and K_2CO_3 above 700 ^{o}C are substantially reduced by C forming metallic K, K_2O and CO as indicated in Equation (1.11 – 1.12). Also, a significant Boudouard reaction ($CO_2 + C \rightarrow 2CO$) occurs at a higher temperature along with a water-gas shift reaction ($CO + H_2O \rightarrow CO_2 + H_2$) [62].

$2KOH \rightarrow K_2O + H_2O$	for dehydration	(1.8)
$CO_2 + K_2O \rightarrow K_2CO_3$	for potassium carbonate formation	(1.9)
$K_2CO_3 \rightarrow K_2O + CO_2$	for potassium oxide formation	(1.10)
$K_2CO_3 + 2C \rightarrow 2K$ (or K_2O) $+ 3CO$	for reduction by carbon	(1.11)
$K_2O + C \rightarrow 2K + CO$	for reduction by carbon	(1.12)

Activated carbon was produced for use in many applications such as chemical separation and purification, electrical power sources as battery and fuel, catalysts etc. [66]. A recent study of activated carbon production and its applications using rice wastes were reported. Adinaveen et al. [73] produced activated carbon using pyrolyzed rice straw with H_3PO_4 as an activating agent. A highest surface area of 376 m^2/g and a maximum capacitance of 112 F/g were obtained from activated carbon produced at 600 ^oC. Hwang et al. [74] constructed carbon fibers from rice straw and paper mulberry through a wet spinning and carbonization process for usage as hydrogen storage. The 8 M KOH solution treatment showed a 2,260 m^2/g surface area with 4.35wt% hydrogen uptakes. Teo et al. [75] utilized rice husk wastes to make KOH activated carbon for a supercapacitor electrode. The highest surface area produced at 850 ^oC showed 2695 m^2/g of surface area and 147 F/g of specific capacitance.

Pore analytical models and isotherm types

The most frequent analytical models for activated carbons are BET (Brunauer, Emmett, and Teller) and DFT (Density Functional Theory). BET, as an extended Langmuir theory, applies not only to a monolayer, but also to multilayers adsorption. As most activated carbons do not form a homogenized carbon structure, the BET model needs to be applied to measure a specific surface area of the multi-layers. On the other hand, DFT is a molecular-based statistical thermodynamic theory that can be used to analyze pore sizes down to micropore and mesopore ranges as the model is not affected by capillary condensation unlike a BJH (Barrett, Joyner and Halenda) method [65].

Capillary condensation happens when pore spaces are filled with a vapor which condenses into liquid form, when the vapor pressure, P_v, is lower than the saturation vapor pressure, P_{sat}. Then the condensed liquid forms a meniscus, which is mainly dependent on the surface tension and the shape of the pores. The Kelvin equation shows the relationship of the equilibrium vapor pressures and the saturation vapor pressure, P_v/P_{sat}. The different pressures are often used for measuring the sorption isotherms of porous materials. The higher the P_v/P_{sat}, the more vapor would condense in pores, whereas the lower P_v/P_{sat}, the more vapor would evaporate. The different pressures can be explained with adsorption/desorption isotherm graphs.

Depending on the shape of the isotherm graphs followed by the pressure differences, the graphs were classified into five Types I, II, III, IV, and V with four hysteresis loops of H1, H2, H3, and H4 according to an extended IUPAC classification [65] as shown in Figure 1.4. Type I isotherms show a steep relative pressures and reach a plateau, which indicates micropores. The difference between (a) and (b) is the size of micropores. A slower rate reaching to a plateau for Type I (b) indicates the presence of wider micropores. Type II isotherms normally indicate a non-porous or a macroporous adsorbent that allows an easier flow of pressures. However, Type II with hysteresis loop, H3, represents the presence of inter-particle capillary condensation, which would indicate micro/mesopores. Type III isotherms indicate a non-porous or macropore adsorbent as the knee of an isotherm curve is not present. Type IV isotherms that combine the shape of Type II isotherms normally indicate mesoporous adsorbents with a hysteresis loop associated with capillary condensation in mesopores. Type V is a

combination of Type III with hysteresis, and Type VI represents a layer-by-layer adsorption which can be mostly found from graphitized carbon.

The hysteresis loops produced from the capillary condensation in the pores are associated with the filling (the lower curve of adsorption) and emptying (the upper curve of desorption) of the pores. Hysteresis 1 (H1) loops correspond to a narrow distribution of uniform pores such as open-ended tubular pores, while H2 loops are obtained from complex and interconnected different sized pores. H3 loops indicate the aggregates of platy particles, and H4 loops are often found in activated carbons with slit-shaped micropores.

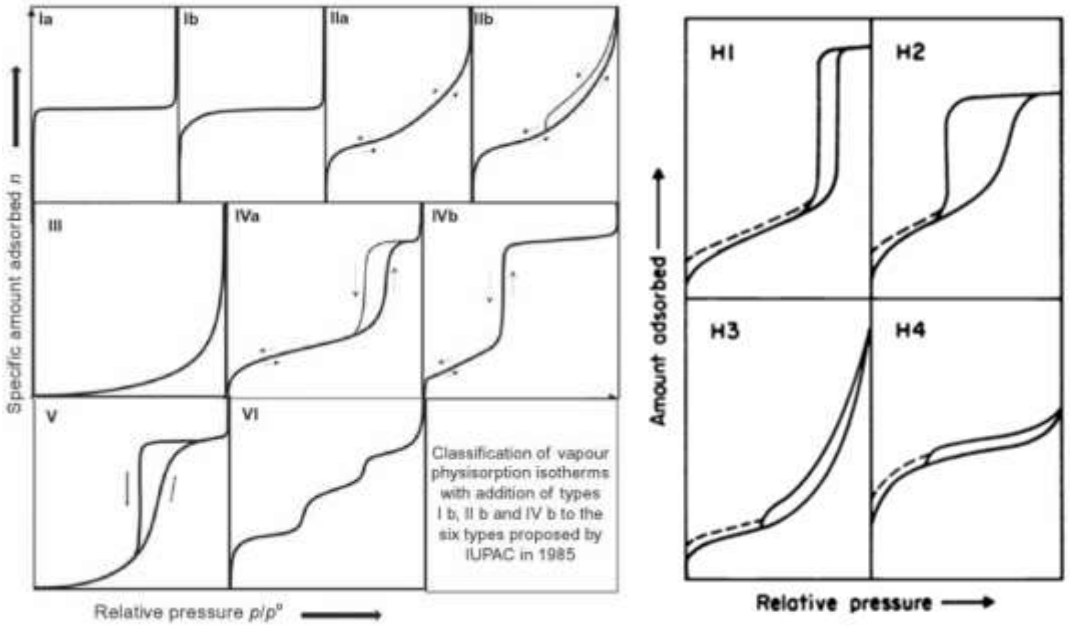

(a) (b)

Figure 1.4. The sorption isotherm (a) Types and (b) hysteresis loops introduced from IUPAC [65].

Adsorption of pollutants

The activated carbon adsorbent has been approved for and widely used for removing color, odor, and other pollutants mixed with water and air. Contaminants for the removal studies included SO_2, NO_x, H_2S, VOCs, dyes, phenols, heavy metals, pesticides, and medicines [76]. Representative parameters used for a contaminant adsorption study includes the pH of the solution, contact time, initial contaminant concentration, adsorbent dose, and process temperature. The pH of an aqueous solution normally varies in the increase or decrease in the negative charge on the adsorbent surface, which deals with the electrostatic force between the adsorbent and adsorbate ion. The lower the pH (acidized), the higher the protonation tendency of the adsorbent. The determination of the optimum contact time needs to be considered at each parameter for economic evaluation. The increase in the adsorbent dose would definitely increase the rate of removal, but a further increase would not show any significant removal. The higher the process temperature, the higher a removal rate would normally be obtained due to a faster diffusion and a broader surface area caused by oxidation [77].

Luna et al. [78] conducted the removal of Eriochrome Black T dye using RHAC (rice straw activated carbon) to find the optimum conditions based on initial concentration, adsorbent dose, and pH. Also, a kinetic data of its performance was understood. The highest removal of 95.9% was made at a 95 ppm concentration, an adsorbent of 2 g, and a pH of 2. All kinetic models of pseudo-first order, pseudo-second order, and intraparticle diffusion model were well fit to the experiment work with a good fit correlation coefficient of over $R^2 = 0.98$. Mashayekh and Moussavi [79] used

pomegranate wood activated carbon to remove acetaminophen pollution from water. They applied different conditions of pH, time, initial solution concentration, adsorbent concentration, and temperature. The significant removal was made under the conditions of a pH of 2 – 8, a short contact time of less than 5 min, and a low concentration of adsorbent achieving a maximum 233 mg/g adsorption capacity. The adsorption was found to follow the pseudo-second order kinetic model and fit in the Langmuir isotherm. Similar to this work, activated carbon from animal hair and cattail fiber was applied to remove acetaminophen contaminant by Liu et al. [80]. The removal of an ibuprofen contaminant was also studied using activated carbon from cork waste done by Mestre et al. [81].

Electrode material application for a supercapacitor

The electrochemical capacitors can be grouped into two types of electrical double layer capacitors (EDLC) and supercapacitors (SC) based on the types of energy deal with. The EDLC is based on a pure electrostatic attraction, while the SC is an accordance with both the electrostatic attraction and pseudocapacitance reactions (faradaic and redox reactions). Thus, the supercapacitors can reach a higher energy (the capacity to do work) density by maintaining the high power (how fast the energy is delivered) density as much as conventional capacitors, which energy and power density of supercapacitors locates in between those of capacitors and batteries.

Two methods among a number ways of testing the performance of a supercapacitor are introduced: cyclic voltammetry (CV) method and galvanostatic

method. CV tests are conducted by applying a range of voltages at a constant sweep rate (V/s) for simultaneous response of current. The results provides a charge and response performance of supercapacitor in accordance to a varying voltage. The specific capacitance can be calculated using an Equation (1.13). The CV graph normally presents a relationship of capacitance (F/g) and voltage (V). A higher sweep rates is associated with a higher power levels for charging and discharging the materials. The evaluation of constant-current charging performance can be made with the second method of galvanostatic method. A typical constant current charge and discharge shows a linear curves, while the pseudocapacitance results a non-linear curves.

$$C_{sp} = 2 \times I/m \times (dV/dt) \quad (1.13)$$

where, I = current

m = the mass of electromaterial on a working electrode

dV/dt = a constant sweep rate

The shape of the ideal voltammogram is rectangular if the capacitance behavior is only from an ideal EDLC. In contrast, the materials with a pseudocapacitance property affect on the irregular rectangles due to the reversible redox peaks as indicated in Figure 1.5 (a). As Figure 1.5 (b) shows, the square box of EDLC mainly affected by an electrostatic attraction portion remain unchanged under different voltage application in contrast to the pseducapaciance regime that varies [82,83].

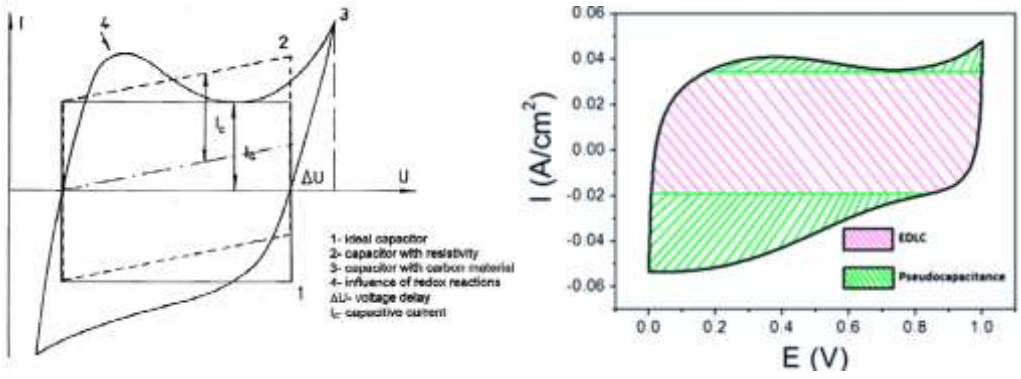

(a) (b)

Figure 1.5. Cyclic voltammetry graph of (a) typical charge and discharge characteristics imported from Frackowiak and Béguin [82] and (b) the CV curve divisions of EDLC and pseudocapacitance [83].

Various natural biomass-based materials were used for electrochemical material studies after activation of carbons. Some include wood sawdust [84], wheat straw [85], cow dung [86], and waste paper [87]. Wei et al. [84] activated wood sawdust for an electrochemical material and reported the highest specific capacitance as 236 F/g at a sweep rate of 1 mV/s. [85]. Bhattacharjya and Yu [86] converted a biological waste cow dung into activated carbon with KOH for electrochemical application. The best performance of specific capacitance using non-aqueous electrolyte was obtained as 124 F/g at 0.1 A/g. Besides the discussed the studies, the common specific capacitance of activated carbon is known about 70 -120 F/g in organic electrolytes [84].

1.2.5. Hydrotreatment

The pyrolytic bio-oil was identified as a source for a potential fuel substitute or additive. Bio-oil products from pyrolysis are normally difficult to use as they are

composed of numerous chemical compounds of various functional groups and a wide range of molecular weights, which sometimes causes unwanted bio-oil characteristics. Thus bio-oil needs further processing to be able to be used commercially and meet ASTM standards including physical, chemical, and catalytical upgrading can be viable as reviewed in the literature [88-90]. Pyrolysis bio-oil has several properties that can be upgraded including high oxygen and solid content, high viscosity, and instability. Current bio-oil upgrading studies are mostly based on catalytic hydrotreatment to reduce the oxygen content. In the process, the bio-oil reacts with hydrogen in a condition of high temperature and pressure. A two-step method is usually proposed: 1) deoxygenation with a lower amount of hydrogen gas to stabilize the pyrolysis oil and 2) a high temperature hydrotreatment with a catalyst for complete deoxygenation [91]. The oil upgrading process can be simplified as in the following Equation (1.14) [92]:

$$C_6H_8O_4\,(\text{bio-oil}) + 6H_2 \rightarrow 6CH_2\,(\text{hydrocarbon}) + 4H_2O \qquad (1.14)$$

The other way of physical upgrading is distillation. Vacuum distillations are mainly used for heat sensitive chemical compounds which can be degraded or transformed by high temperature exposure. Jewel and Capareda [93] performed a fractional distillation at atmospheric and low vacuum pressure (50 kPa) using corn stover pyrolytic crude oil. Still, the high oxygen content and total acid number of distillates requires further catalytic upgrading.

The catalytic upgrading of bio-oil can be achieved mainly by reducing the oxygen content through hydrotreating and breaking carbon-carbon bonds through hydrocracking in the presence of a catalyst, hydrogen, high temperature, and high pressure. The deoxygenation happens by converting oxygen into carbon dioxide and water. Moreover, other significant reactions of decarbonylation, decarboxylation, hydrogenation, depolymerization and carbon formation also occur during the upgrading as well as an important reaction of hydrodeoxygenation as indicated in Figure 1.6.

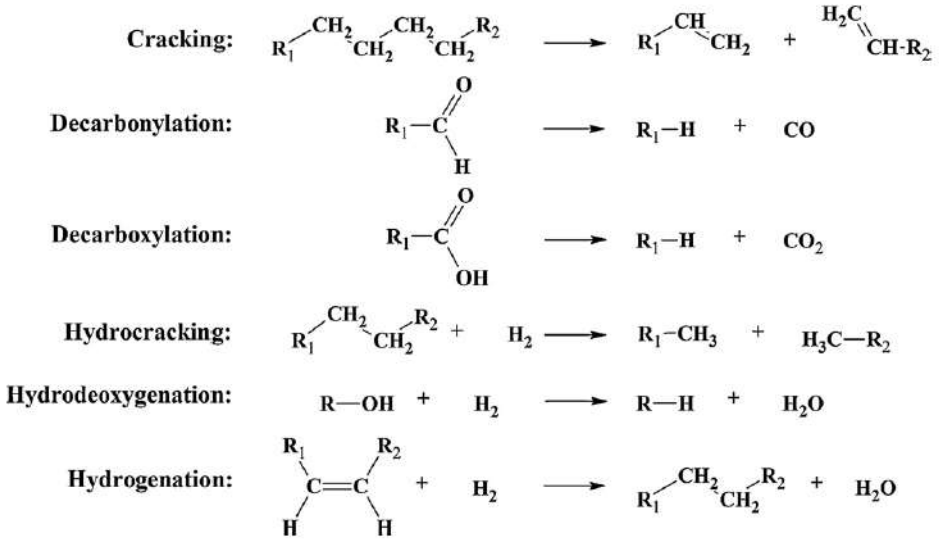

Figure 1.6. Representative chemical reactions during bio-oil upgrading [94,95].

Noble metal catalysts such as palladium (Pd) and ruthenium (Ru) were used in bio-oil hydrotreatment to understand the effectiveness of bio-oil upgrading [96,97]. Catalysts for conventional petroleum such as sulfide cobalt-molybdenum- (CoMo) and nickel-molybdenum- (NiMo) have the disadvantage of potential deactivation if sulfur is

rare in the fuel like bio-oil [98]. Wildschut et al. [99] concluded that the Pd/C catalyst was the better choice when considering both low oxygen content and a high yield compared to Pt/C which resulted in a relatively high oxygen content with the best yield. An aquatic biomass duckweed bio-char was used as a catalyst [100]. The CO_2 treated bio-char helped reform biogas as an initial catalytic activity. Char supported metal catalysts of Ni/char and Ca/char were also reported [101]. The use of catalysts improved H_2 production in brown coal steam gasification. During hydrotreatment, high pressure was considered an important variable as it not only helps a better reaction of hydrogen with bio-oil that increases the reaction rate, but also decreases the amount of coke [95]. Even though many studies found that a noble metal on carbon catalysts improved the fuel quality, the unit price of palladium (Pd), for example, was found to be $589/oz. ($9,424/lb) compared to the unit price of nickel at $3.9/lb reported by www.kitco.com on March 18, 2016.

The Handbook of petroleum product analysis [102] by Speight introduced the general summary of carbon ranges and distillation temperature of each petro based products as indicated in Table 1.2. The lower carbon ranges from C_1 to C_4 indicated a hydrocarbon gas, while the ranges of carbon from C_4 to C_{12} or C_{16} represented naphtha, gasoline and kerosene fuel. A higher carbon range from C_{12} to C_{20} above indicated fuel oil, lubricating oil, wax, asphalt, and coke. The boiling point and carbon ranges of each petro fuel was used for discussions on the bio-oil distillation and bio-oil upgrading studies.

Table 1.2. General properties of petro fuels [102].

Product	Lower carbon limit	Upper carbon limit	Lower boiling point (°C)	Upper boiling point (°C)	Lower boiling point (°F)	Upper boiling point (°F)
Refinery gas	C_1	C_4	−161	−1	−259	31
Liquefied petroleum gas	C_3	C_4	−42	−1	−44	31
Naphtha	C_5	C_{17}	36	302	97	575
Gasoline	C_4	C_{12}	−1	216	31	421
Kerosene/diesel fuel	C_6	C_{18}	126	258	302	575
Aviation turbine fuel	C_8	C_{16}	126	287	302	548
Fuel oil	C_{12}	$>C_{20}$	216	421	>343	>649
Lubricating oil	$>C_{20}$		>343		>649	
Wax	C_{17}	$>C_{20}$	302	>343	575	>649
Asphalt	$>C_{20}$		>343		>649	
Coke	$>C_{30}$ [a]		>1000[a]		>1832[a]	

[a] Carbon number and boiling point difficult to assess; inserted for illustrative purposes only.

1.2.6. Related publications

The published manuscripts were reprinted in the dissertation with permission from *Elsevier* and *ASABE*. The last two studies are actively being reviewed by the journal reviewers.

- **H. Nam**, A.L. Maglinao, S.C. Capareda and D.A. Rodriguez-Alejandro, Enriched-air fluidized bed gasification using bench and pilot scale reactors of dairy manure with sand bedding based on response surface methods, *Energy*, 95 (2016), 187-199 [I.F. 4.844].
- **H. Nam**, A.L. Maglinao and S.C. Capareda, Oxygen gasification of processed dairy manure and its syngas upgrading in a bench-scale fluidized-bed reactor, Proceedings of ASABE 2015 International Meeting, New Orleans, LA, July 26-29, 2015.

- **H. Nam** and S.C. Capareda, Experimental investigation of torrefaction of two agricultural wastes of different composition using RSM (Response Surface Methodology), *Energy* 91 (2015), 507-516 [I.F. 4.844].
- **H. Nam**, S.C. Capareda, N. Ashwath and J. Kongkasawan, Experimental investigation of pyrolysis of rice straw using bench-scale auger, batch and fluidized bed type reactors, *Energy*, 93 (2015), 2384-2394 [I.F. 4.844].
- **H. Nam**, J. Choi and S.C. Capareda, Comparative study of vacuum and fractional distillation using pyrolytic microalgae (*Nannochloropsis oculata*) bio-oil, *Algal Research*, accepted on April 2016 [I.F. 5.014].
- **H. Nam**, A.L. Maglinao and S.C. Capareda, Studies to effectively utilize dairy manure mixed with sand bedding for thermal conversion processes, in review.

2. PROCESS EVALUATION OF SAND BEDDING MIXED DAIRY MANURE FOR THERMAL CONVERSION FUEL SOURCE AND ITS CHARACTERISITICS

2.1. Introduction

A USDA report [103] determined the types of bedding materials used in dairies in the U.S. to be sand, straw or hay, sawdust/wood products, compost manure, rubber mats and tires, corn cobs and stalks, waterbeds, and mattresses. The most frequent material for bedding was reported to be sand (25.8%) because it is regarded as an ideal choice for a dry and clean environment by preventing bacterial growth. Also, the sand bed material offers a comfortable and uniform bed for cows to lie on. A study [104] determined that 92% of dairy cows that bedded on sand showed no lesions, while 84% of the cows lying on waterbeds had lesions. Also, at dairies with sand bedding, 24% more cows were active after leaving the milking parlor. For these reasons, sand materials for bedding have been used in many dairy cow facilities, which causes a negative effect on the desirable feedstock for thermal conversion processes such as combustion and gasification.

The separation of manure and sand after liquid has to be done for many applications. Various technologies or processes have been reported and developed. Wedel et al. [105] developed a sand-manure separation for anaerobic digestion pretreatment using a main SMS (sand-manure separation) system and a hydrocyclone which each recovered 87% and 8% of the sand for reuse. Also, a wide range of manure and liquid separators were introduced such as a rotating screen, brush-roller, vibrating

screen, screw press, belt press, and run-down screen [106]. The suggested screen size for the screw press was 1 – 5 mm depending on the amount or type of fiber mixed with the manure. A sedimentation principle was also suggested for the finer particles of less than 1 mm, which may not be applied to animal slurries due to the small density difference. Thus, the two step separations of screening fiber and settling manure were recommended to deal with a manure slurry. Other apparatuses for separation of sand and manure were reported. The wet sand mixed manure was dumped into a chamber. The water first drained, sand was settled on the floor, and the remaining manure was suspended in the suspension [107]. A screw auger based separator was designed for extracting sand from raw slurry [108]. A drying study with swine manure was discussed and it was determined that the air drying time of manure depended on the amount of manure [109]. Even though organic wastes can be optimal candidates for a thermal conversion process of combustion or gasification, some difficulties include slagging, fouling, bed agglomeration, and corrosion [110]. Especially, the major inorganic material of high ash content in dairy manure could easily result in these problems. Slagging includes stickiness, ash melting, and sintering in a main boiler, while fouling happens because of condensation of vaporized inorganics on flow pipes. A prediction of the troublesome inorganic formation in a high temperature reactor can be conducted based on the inorganic chemical compounds of base and acid [111-113]. Those several indices used in previous studies were an alkali index, a base-to-acid ratio, a fouling and slagging factor, and a bed agglomeration index.

In this study,

1) The collected sand mixed dairy manure is analyzed to determine the optimum conditions for developing a pilot scale handling system.
2) The performance of a developed pilot scale manure handling systems is evaluated for continuous dairy manure processing to predict the process rate and the quality of the processed dairy manure.
3) The ash analysis for the bed agglomeration and slagging prediction is investigated to prevent any ash fusion in a high temperature reactor.
4) Finally, the evaluation of the processed dairy manure is conducted through a fluidized bed gasification.

2.2. Materials and Methods

2.2.1. Understanding sand mixed dairy manure

A sample of sand mixed dairy manure, obtained directly from an open field pit at the Sierra Dairy Center in Dublin, Texas, where sand material is used for the main bedding, was first investigated for designing equipment for a pilot scale process. Particle distribution through different sieves (USA Standard Sieves) was used to separate the samples into different sizes of sand and manure particles in regard to moisture content, heating value, and elemental data. The ground (Gr) and non-ground (NGr) acronyms indicate milled and unprocessed samples, respectively, while 10% and 20% indicate the percent moisture content of the dairy samples. The sieve size for milling was 2 mm equivalent to 10 mesh. The dairy manure treated conditions for the sieving tests were expressed in this study as Dry_Gr (manure fully dried after being ground), Dry_NGr (as-

received manure fully dried), 10%_Gr (10% moisturized dairy manure after being ground) and 22%_NGr (as-received 22% moisturized dairy manure).

2.2.2. Pilot scale dairy manure process

A sand dairy manure process for a thermal conversion fuel was developed as shown in Figure 2.1. Each piece of equipment was designed and fabricated based on preliminary experiments. The dairy manure from the Southwest Regional Dairy Center in Stephenville, Texas, was air dried and an additional drying was done both with and without a heater until it dried to less than 5% moisture content. The box-type manure dryer (90 × 90× 180 cm) was equipped with a blower and heater. Air was forced through a perforated flat bed to dry the wet samples. Then the dried manure samples were ground using 5 HP hammer mill with a 4.76 mm sieve (mesh-4). The dried ground manure samples were transferred to a drum sand separator designed and fabricated at TAMU (Texas A&M University) in College Station to separate the sand. Two different sized sieves of mesh-16 and 40 were installed inside the sand separator. The size of the sieves was determined from the preliminary studies described in section 2.3.1.

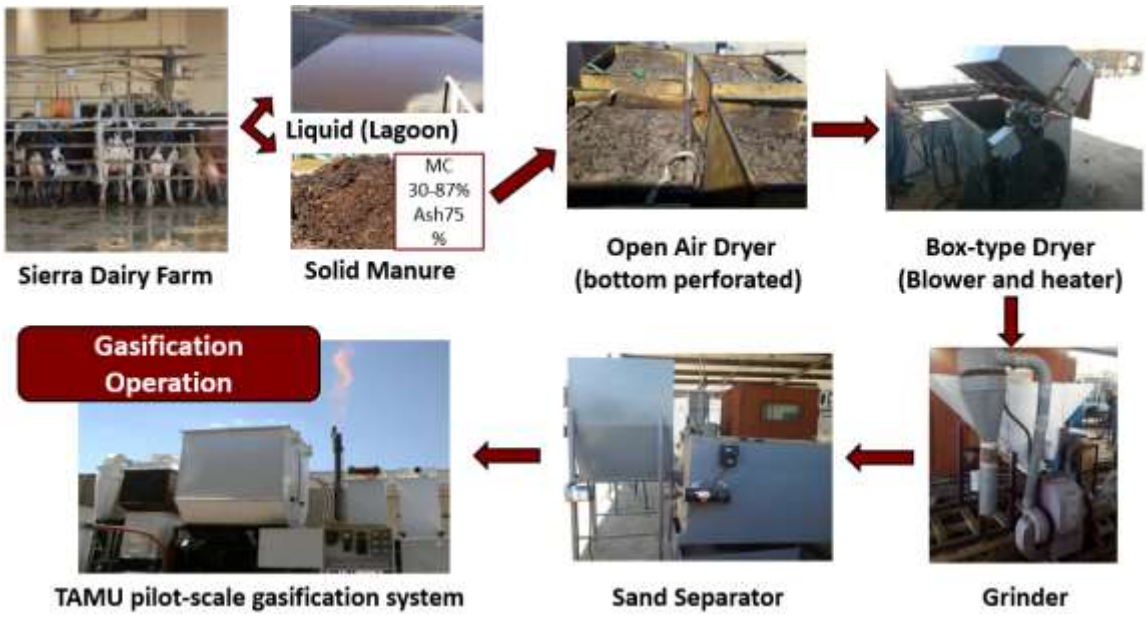

Figure 2.1. Pilot scale sand mixed dairy manure process for a gasification process.

2.2.3. Slagging and fouling prediction of dairy manure

The compressive strength measurements of an ash pellet was used as a method for finding the melting temperature that incurs the slagging and fouling of diary manure. The as-received dairy manure was first converted into ash, and 10 g of ash was pelletized in a uniformed cylindrical shape of 2.54 cm in diameter and 1 cm in height using an MTS model 810, Gray Machinery Co., Prospect Heights. Then, the ash pellets were baked in temperatures of 550, 600, 650, 700 and 750 ^{o}C for 1 and 3 hours. Each conditioned pellet was prepared three times for replication. The prepared pellets were compressed with the same load, and the peak compressive strengths after pellet breakage were recorded for slagging and fouling analysis.

2.2.4. Pilot scale gasification system

A pilot-scale fluidized bed gasification (FBG) system at TAMU has a reactor of 30 cm in diameter, which was used in a previous gasification study [38,114]. The gasifier is protected under intellectual property registration TAMUS 2814 serial No. 61/302,001. The fluidized bed gasifier was equipped with control systems for the air flow and biomass feed, and monitoring systems for pressures, temperatures, and syngas compositions coded by Labview. A 10.2 cm diameter screw conveyor was used for the biomass feeding system. A propane burner initially heated the reactor and two-stage 1D-2D and 1D-3D TAMU designed cyclones were attached to capture the solid chars from the syngas. First, as-received dried manure was gasified to test if the unprocessed material could increase the temperature of the main reactor. Then, the processed manure was used to run the pilot scale gasification system.

2.2.5. Analytical methods for the materials

The proximate data and moisture content of the dairy manure were secured based on the methods of ASTM E1755 and D3172. The heating value (HHV) and elemental data were obtained using a Parr bomb calorimeter and a Vario MICRO Elemental analyzer. The particle size diameter of the manure and sand were determined using USA Standard Sieve Nos. 12, 16, 20, 30, 40, 45, 50, 60, 70, 80, and 100 (ASTM E-1 specification, Fisher Scientific Company, USA). The volumetric gas composition was determined using a gas chromatograph (TCD-GC), which can detect gas mixtures of H_2, N_2, O_2, CO, CH_4, CO_2, C_2H_4, C_2H_6, C_3H_6, and C_3H_8.

For the evaluation of slagging and fouling, various indices of $R_{b/a}$, R_s, R_f, and BAI (bed agglomeration index) were used after an ICP analysis of the processed dairy manure as follows. The $R_{b/a}$ used by Vamvuka and Zografos [111] indicated the ratio of base over acid. A higher ratio represented a larger possibility of fouling. The two indices of R_s and R_f represented the possible tendency of slagging and fouling, which used for the potential ash fusion in coal combustion systems [115], while BAI (bed agglomeration index) by Bapat et al. [116] was used to predict the agglomeration in fluidized bed reactors. Moreover, an alkali-induced slagging criteria was established by Niu et al. [117] of Cl and S ratios as indicated in Equation (2.5 – 2.6).

$$R_{b/a} = \text{Base} / \text{Acid} \quad (2.1)$$

$$R_s = R_{b/a} \times \%\text{Sulfur} \quad (2.2)$$

$$R_f = R_{b/a} \times Na_2O \quad (2.3)$$

$$\text{BAI} = \%(Fe_2O_3) / \%(K_2O + Na_2O) \quad (2.4)$$

where Base = $\%(Fe_2O_3 + CaO + MgO + K_2O + Na_2O)$,

Acid = $\%(SiO_2 + TiO_2 + Al_2O_3)$

$$\text{Cl ratio} = (Cl + K_2O + Na_2O) / (SiO_2 + Al_2O_3) \quad (2.5)$$

$$\text{S ratio} = (S_{volatile} + K_2O + Na_2O) / (SiO_2 + Al_2O_3) \quad (2.6)$$

2.3. Results and Discussion

2.3.1. Basic understanding of sand mixed dairy manure

Table 2.1 shows the properties of sand-mixed dairy manure compared to fresh manure obtained directly from the dairy cattle. The as-received sand-mixed manure contained almost 71% (dry basis) ash resulting in a very low heating value of 5.5 MJ/kg, while the fresh manure showed 18 MJ/kg with a 16% ash content (dry basis). The standard deviation of HHV was high as the homogenous sampling was difficult to heat due to sand particles. The HHV of as-received manure from an ash based, and an ash and VCM based empirical equations (Jenkins, 1989), showed 3.5 MJ/kg and 3.2 MJ/kg, which is an even smaller value than the actual HHV. The relative amount of VCM (volatile combustible matter) and FC (fixed carbon) contents showed a lower value for each sample. The high ash content can not only interrupt the burning of organic matter, but also cause fouling and slagging problems in a high temperature oxygen present reactor [113]. Thus, the sand (or ash content) should be removed for the material to be used as a thermochemical conversion fuel source.

Table 2.1. Characteristics of dairy manure directly from a lagoon, and fresh manure (db: dry basis, wb: wet basis).

	HHV, db (MJ/kg)	VCM, db (%)	Ash, db (%)	FC, db (%)	MC, wb (%)
As received	5.5±1.5	25.5 ±0.7	70.6±0.6	3.9±0.3	32.1±0.3
Fresh manure	17.3+0.9	71.2+1.4	13.6+0.8	15.2+0.8	-

Eleven USA Standard mesh sieves were used to separate the previously conditioned dairy manure (dried ground, dried non-ground, 10% MC ground, and 22% non-ground manure samples). Figure 2.2 shows a partial weight fraction of differently processed dairy manure before sieving. The group of NGr (non-ground) samples shows a large amount of big particles (above mesh-12) regardless of the wetness of the samples as the manure was clumped together. On the other hand, Gr (ground) samples showed an ease of sieving by shaking the sieving pans, which led to larger weight fractions in higher meshes. From all the processing conditions, large weight fractions were found in the higher mesh sieves from 70 to 100, which was caused mainly by the large amount of sand.

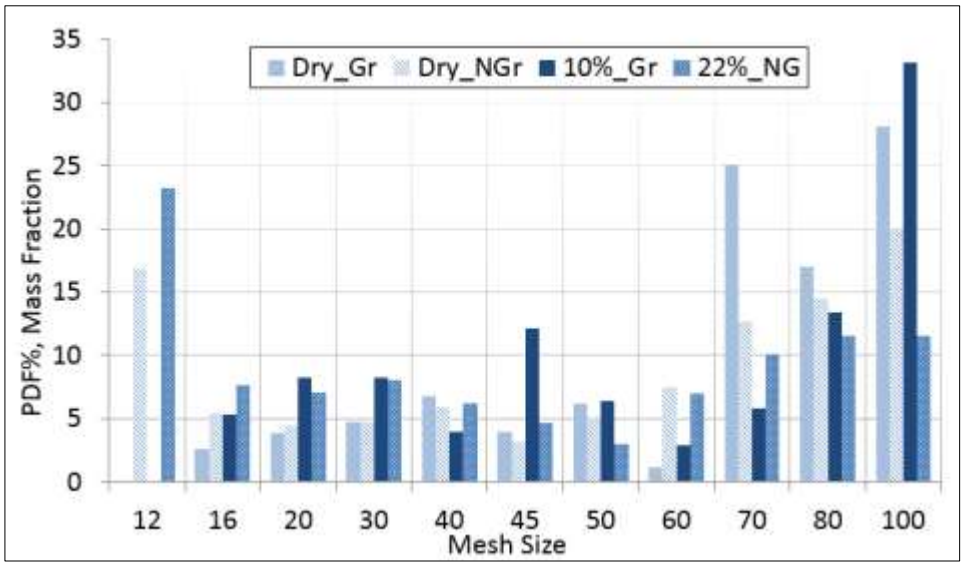

Figure 2.2. Partial weight fractions of treated dairy manure in each sieve.

The ash content of the as-received sample was found to be from 70 to 80%. Figure 2.3 shows the ash contents found in the sieved dairy manures. In all conditions, the separated manure between mesh-16 and mesh-30 showed an ash content less than 40 - 50%. A relatively high ash content, about 50 – 60%, was found in non-ground samples from mesh-12 to mesh-40 due to manure lumps containing a large amount of sand, while the ground samples showed about 40% ash content in mesh-16, mesh-20, and mesh-30. The lowest ash content in the processed manure was obtained as 39% from Dry_Gr (the fully dried ground dairy manure sample) in mesh-20 and mesh-30. Above mesh-45 or mesh-50, the separated samples showed an abrupt increase in ash content, which can be expected from the sand. From the ash contents at different sieves, the sieve sizes between mesh-16 and mesh-40 were recommended to reduce the ash content of the manure.

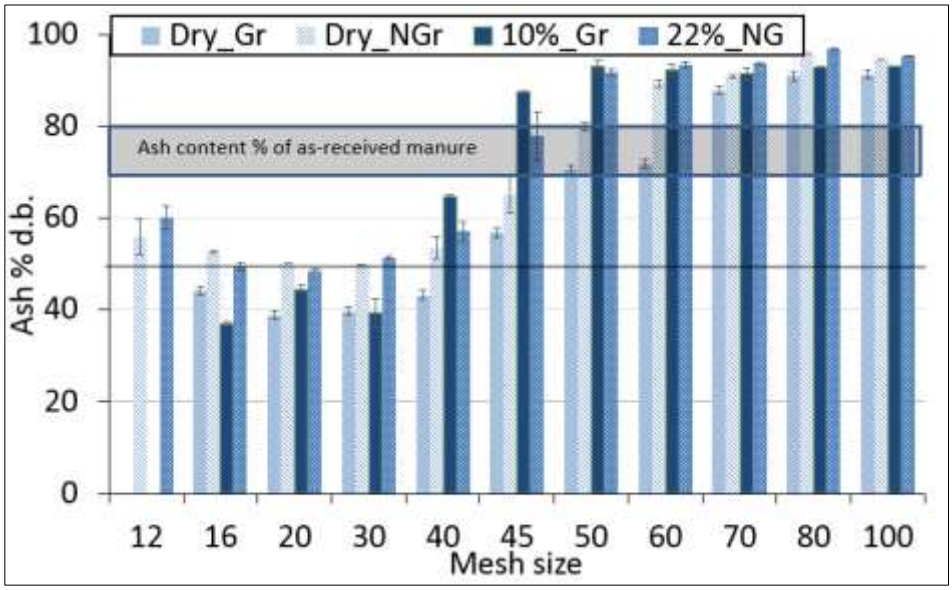

Figure 2.3. Ash contents in each separated sand mixed dairy manure at different sieves.

Figure 2.4 shows the cumulative mass distribution of the sieved dairy manure based on ash content at an incremental mesh size. The cumulative recovery of manure was another important factor for the fuel recovery after sand separation. First, the effect of Gr/NGr (ground/non-ground) conditions on the cumulative mass recoveries varied much. As the manure was ground, a large portion of sand from the manure lumps was separated, and lower ash in ground manure was sieved compared to unground samples. On the other hand, the unground manure showed a high ash content of around 50% with a higher cumulative mass fraction than the ground manure samples. The second variation of condition was moisture. The effect of moisture on separation was not significant on the ground samples, but was on the unground samples. The higher moisture contents were included in manure samples before separation, the larger cumulative fraction was obtained at the lower sieves. This is because the moisture helped form lumps containing a large amount of sand. As suggested in a previous discussion, if the processing sieve is set below mesh-40 by targeting to have less than 50% ash, the mass recovery of the ground samples is around 20 – 27 wt.% with about 40% ash content, while the non-ground manure can be recovered up to 50 wt.% with about 50% ash content. Considering a much higher density of sand than pure manure, the manure recovery of 50% from the non-ground to 20 – 27% from the ground would be less than twice the difference from a carbon or HHV point of view.

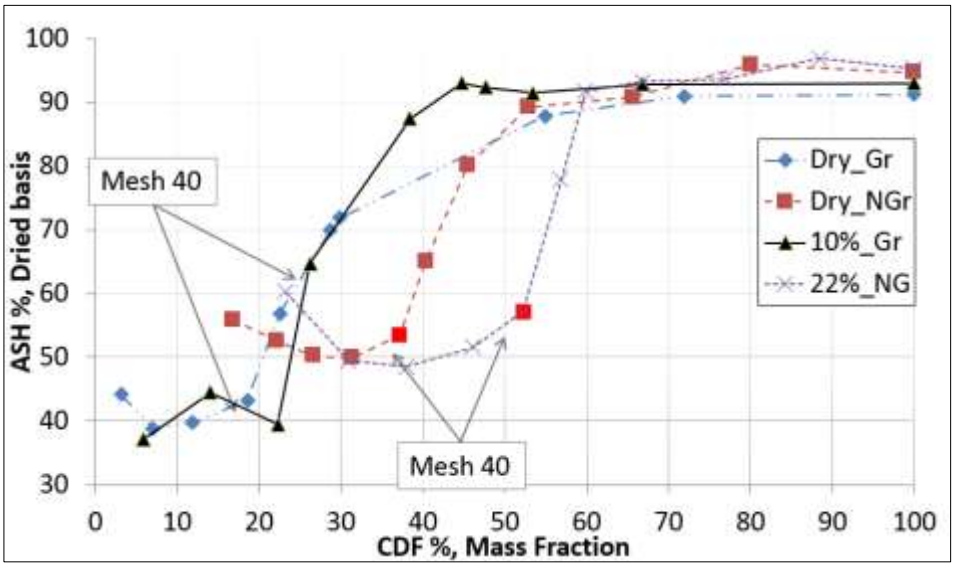

Figure 2.4. Cumulative distribution of mass fractions vs. ash content.

The moisture content of each sieved sample was investigated as shown in Figure 2.5. The moisture contents with Dry_Gr and Dry_NGr samples were less than 2% through all the different sized sieves as they were fully oven dried. On the other hand, the moist samples showed a large variation of moisture contents at different particle sizes. Due to the nature of the hydrophobicity of sand and the hydrophilicity of organic manure samples, high moisture contents remained in the smaller meshes that contained less ash content as described earlier. The moisture content was abruptly decreased after mesh-40 or mesh-45, which can be another indication of percent ash or sand in the sieved samples. If the sand mixed manure is sieved at mesh-40, the average moisture contents would be 1 – 2% for the fully dried case (Dry_Gr and Dry_NGr), about 8% for the 10% Gr sample, and around 35% for the 20% NGr case.

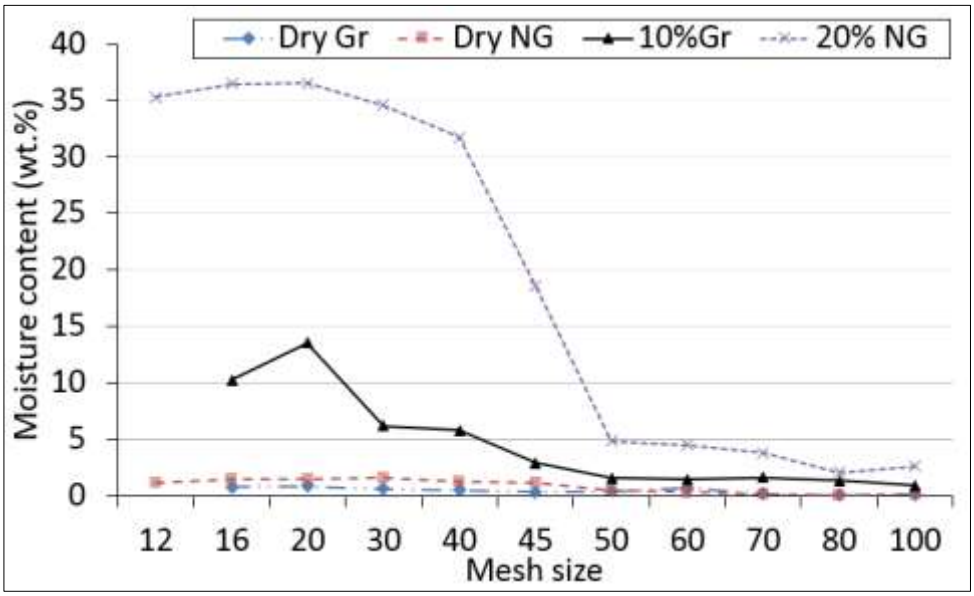

Figure 2.5. Moisture content of dairy manure at different sieves.

The different ash content from the different sieving conditions between mesh-12 and mesh-40 resulted in different heating values and elemental data as shown in Figure 2.6. The highest HHV after conditioned sieving was obtained as 11.4 MJ/kg at the Dry_Gr condition, while the HHV of the Dry_NGr sample showed 9.3 MJ/kg, which is almost twice an improvement in HHV of the as-received manure. However, the improved HHVs and reduced ash contents were still not close to the pure dairy manure of 17.8 MJ/kg and 17% ash content. The compositions of carbon (32 to 19%), hydrogen (3.7 to 2.4%), and nitrogen (2.7 to 2.0%) contents were inversely linear to the amount of ash contents (42 to 55%). The lower ash content induced the higher carbon contents.

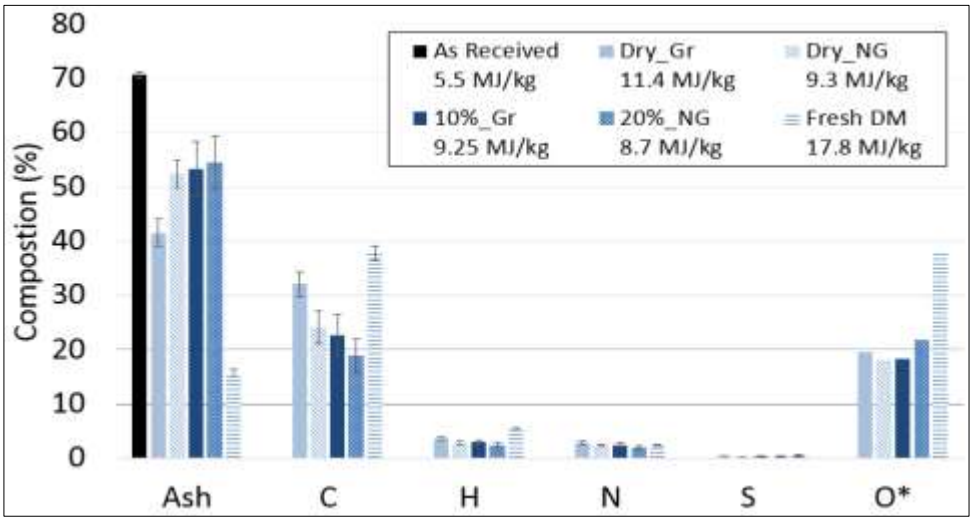

Figure 2.6. Elemental data and heating value of dried ground/non-ground conditions.

2.3.2. Evaluation of the pilot scale dairy manure handling system

A pilot scale dairy manure handling system was developed based on the results obtained in the previous sections. Figure 2.7 shows the physical appearance of dairy manure at each stage of air dried, burner dried, after ground, and after sand separation. The moisture contents of manure air dried for two weeks was still high as much as almost 40%. The moisture content of the swine manure after air drying was also obtained as 40 – 50% [109]. Big lumps of manure after burner drying can easily form as the moisture evaporates in a static bed during the drying process. After the milling, many sand particles mixed with manure were easily recognized, and these included 76% ash content. The final manure samples after the sand separation stage looked as if they were a mixture of dried manure and grass as shown in Figure 2.7 (d). The moisture content of the dried sand mixed manure was increased from 2% to around 10% as the hydrophobic sand particles were removed from 76 to 46% ash, which added a larger sample weight.

(a) Air dried (MC40%) (b) Burner dried (MC2%) (c) Ground (Ash76%, MC2%) (d) Sand separated (Ash46%, MC10%)

Figure 2.7. Physical appearance of samples at each stage.

Table 2.2. Characteristics of processed dairy manure through a pilot scale process.

Characteristics	Processed T. DM with pilot process	As-received T. DM from dairy	Fresh dairy manure
Higher heating value, MJ/kg db	11.0	3.3	17.3
Proximate analysis (wt%), db			
Volatile combustible matter	46.2	26.9	71.2
Fixed carbon	4.9	0.8	15.2
Ash	48.8	72.3	13.6
Ultimate analysis (wt%), db			
C	23.9	-	32.8
H	3.0	-	2.5
N	2.1	-	4.2
S	0.21	-	0.21
O*	22.1	-	24.5
H/C	1.48	-	0.91
O/C	0.69	-	0.56
Physical properties, db			
Angle of repose, degree	34.5	-	-
Angle of friction, degree	42.5	-	-
Bulk density, kg/m3	267.5	-	-
Particle density, g/cm3	0.926	-	-
pH	7.6	-	-
Conductivity (Umhos/cm)	1670	-	-

*T. DM: Dairy manure from Tarleton State University (Southwest Regional Dairy Center)

The final processed dairy manure product were completely analyzed and compared with as-received dairy manure and fresh dairy manure as shown in Table 2.2. The fresh dairy manure was collected in a clean holding pan by capturing wastes directly from cows.

The HHVs of the samples were proportionally changed based on the amount of sand in the manure samples. The HHV of fresh dairy manure is 17.3 MJ/kg, which is as high as general lignocellulosic biomass such as cotton stalk at 17.0 MJ/kg [118] and corn stover at 18.3 MJ/kg [119]. The more sand in the manure decreased the HHV of as-received manure of 3 MJ/kg to the processed manure of 11 MJ/kg. Again, a higher carbon content was found in fresh dairy manure than processed manure from the ultimate analysis. A higher nitrogen content in freshly obtained manure compared to processed manure also indicated that more protein was included in the fresh sample. Thus, the amount of sand in the sample reduced all the properties needed for the thermochemical conversion process. Further the physical properties of the processed dairy sample was investigated. The angle of repose and friction are important properties when a feedstock hopper needs to be fabricated. A sliding angle from 40 to 45 degrees for the processed dairy manure is suggested. The bulk and particle density of the final manure product was obtained as 267 kg/m^3 and 0.926 g/cm^3, which will be considered for storage design and transporting the feedstock. Also, a large amount of manure weight can be easily estimated with the known density. Electrical conductivity and pH value of manure is useful when the sample is used as a fertilizer. The presence of salt in the sample is related to the level of electrical conductivity. Landis et al. [120] reported that

the electrical conductivity of fertilizer up to 4000 Umhos/m, which is a minimum conductivity value for soils, didn't affect most agricultural plants, but woody plants are sensitive and were affected. The conductivity of 1670 Umhos/m of processed dairy manure can be considered as safe for fertilizer applications [121].

Table 2.3 (a) shows the inorganic minerals of processed dairy manure. The total P of 0.26% and K of 0.33% were found to be similar to the reported manure amendments in forms of liquid manure (0.17% P and 0.18% K), solid manure (0.38% P and 0.78% K) and composted manure (0.29% P and 0.42% K) [122]. Also, the oxidation on a stainless iron reactor with the corrosive materials of potassium and sodium can be expected or prevented by knowing the mineral contents beforehand. Moreover the inorganic contents shown in Table 2.3 (b) were used for the investigation of slagging and fouling prediction. Some water soluble mineral compounds of CaO (27%), MgO (11%), Na_2O (2%), and K_2O (5%) showed much less quantity compared to that reported in another study [113] as the dairy manure sample in this study was collected in a dairy pit after it was washed with water. A detailed discussion of the ash fusion in a high temperature reactor will be presented in a following.

Table 2.3. Mineral information of dairy manure in the pilot scale process (dry basis).

(a)	Ca	Fe	Mg	Na	K	Si	Al	Ti	P	Cu	Mn	Zn
Manure (%)	1.61	0.23	0.30	0.14	0.33	19.8	0.57	0.05	0.26	0.025	0.013	0.017

(b)	CaO	Fe_2O_3	MgO	Na_2O	K_2O	SiO_2	Al_2O_3	TiO_2	S	Cl
Ash (%)	4.85	0.82	0.03	1.64	0.52	86.7	2.21	0.17	0.374	0.763

The recycling of sand bedding for dairies is an important issue as it increases the dairies' profit. Figure 2.8 shows the ash content, which is the direct indication of sand purity, and fractional weight at each sieve. For a good comparison to the filtered sand from the TAMU sand separator, new and reused sands were collected from the Southwest Regional Dairy Center at Tarleton State University. As suggested in the previous section, a sieve above mesh-40 obtained the most weight fraction of sand from all new, TAMU, and Tarleton samples along with over 90% ash content. Especially, the fractional weights and ash contents between the samples from TAMU and Tarleton was very close to each other, indicating that they were the same characterized sand. The TAMU sand separation system can help recover the sand from collected manure which can then be used for bedding. If a mesh-40 as a separation sieve is used for sand separation, the maximum sand recovery using the sand separator designed here is above 99%.

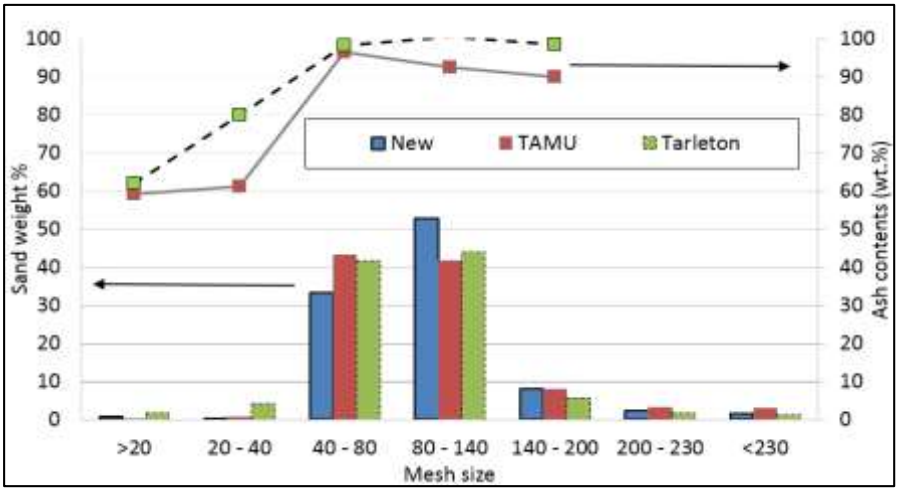

Figure 2.8. Characteristics of filtered sand beds (mass distribution and ash content at different sieves).

The process rate of the pilot scale sand bedding DM handling system developed at TAMU was evaluated as shown in Figure 2.9. The box type manure dryer handled the manure at a rate of 0.068 kg/min with only a blower and 0.425 kg/min with both a blower and heater when the initial moisture content was approximately 35 – 50%. After the samples dried, the bulk density of 951 kg/m^3 was reduced by almost half because of moisture evaporation. The process speed of the grinder and sand separator was rated as 3.44 kg/min and 1.49 kg/min, respectively. The moisture content in the manure increased after filtration as only the organic manure which contained most of the moisture was left. The bulk density reduced by half from a fully dried sample to a final manure sample, when the total weight was recovered by 25%, which was expected as discussed in, Figure 2.4 with 10%_Gr condition.

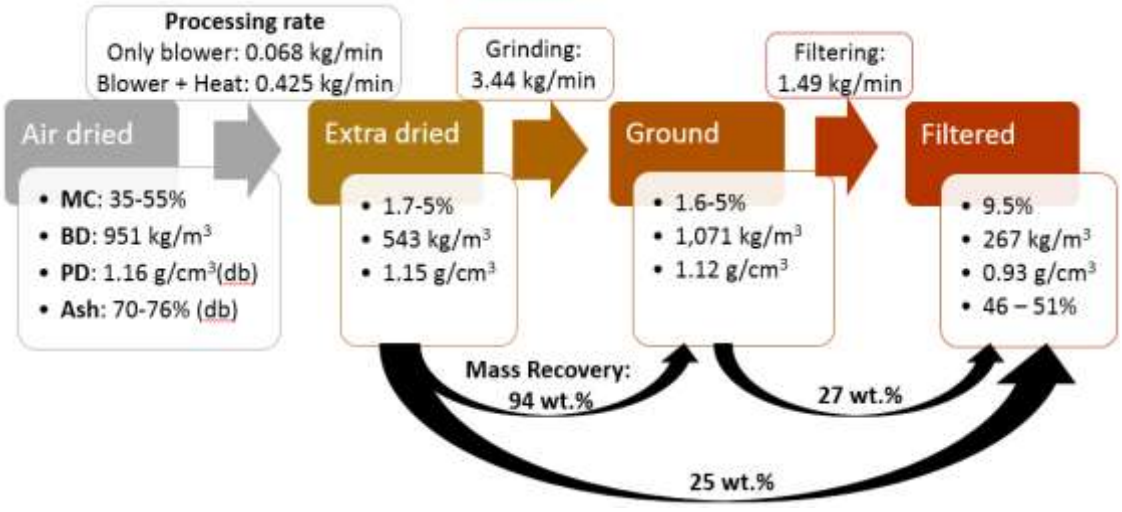

Figure 2.9. Process diagram for the processing rate and mass recovery at each step (MC: moisture content, BD: bulk density, and PD: particle density).

2.3.3. Prediction of agglomeration, fouling and slagging behavior of dairy manure

The prediction of ash agglomeration, fouling, and slagging behavior was investigated based on the inorganic elements in the processed dairy manure ash. Table 2.4 shows the summary of slagging and fouling indices with the inorganic compounds found in the processed dairy manure ash in Table 2.3. All the indices showed low potentials on slagging, fouling, and agglomeration due to washed alkali minerals and a relatively increased Si percent. The increased Si to over 80% would prevent the formation of ash fusion as the melting temperature of silicate is normally higher than the gasification temperature.

Table 2.4. Slagging and fouling analysis based on the various prediction indices.

Index		Ash	Slagging, fouling and agglomeration potential
$R_{b/a}$	Base-to-acid ratio	0.09	> 1, slagging and fouling tendency increases
R_s	Slagging factor	0.04	< 0.6, low slagging potential
R_f	Fouling factor	0.15	< 0.2, low fouling potential
BAI	Bed agglomeration index	0.38	< 0.15, bed agglomeration occurs
Cl ratio	Alkali-induced slagging	0.03	> 2.4, serious slagging
S ratio		0.03	> 1.9, serious slagging

Many proposed indices to predict the ash related issues of alkali induced slagging, silicate induced slagging, and agglomeration in a high temperature furnace [123]. The alkali induced slagging formation would be initiated with fine particles of K, Na, Cl, and S by forming KCl and $K_3Na(SO_4)_2$, which capture coarse ashes with high Si or Al. Then the fused ash deposits on the reactor surface promotes the layer-by-layer

slagging growth unless the initial layer is destroyed. Several studies [113,124] reported that the based-to-acid ratio and slagging (and fouling) factor, originally developed for coal combustions, were not reliable for biomass combustion. Rather, Niu et al. [117] proposed an alkali-induced slagging by including Cl and S contents, which roles as a carrier in reactions that helps the transfer of alkali minerals. Due to a high SiO_2 content, both the Cl and S ratio showed as low as 0.03, which corresponded to slight slagging. The next proposed reason for slagging was from silicate melt. However, as the silicates melt at much higher temperatures than the gasification operating condition, the discussion would be out of the scope of this study. At last, the bed agglomeration in a fluidized bed combustion boiler has been a major problem, which may result in defluidization and an unscheduled shutdown [125]. Visser [126] grouped two different routes of bed agglomeration as melt-induced and coating-induced agglomeration. The melt-induced agglomeration occurs between two or more bed materials with a molten phase as a binder at a spot where a high peak temperature reserves. On the other hand, the coating-induced agglomeration is observed as a coating on the surface of the bed materials. Then a neck between the coated bed particles forms, which leads to agglomeration. A localized high temperature zone promotes both the cases. A BAI (bed agglomeration index) of the dairy manure ash in Table 2.4 was 0.38 larger than 0.15, which suggests no bed agglomeration occurrence. Moreover, three agglomeration indicators of $I1$, $I2$, and $I3$, proposed by Visser [126] represented the formation of fused alkali and silicates on the bed particles, the probability of the coating formation on the reactor, and the probability of melt-induced agglomeration in a quartz bed. All three

indicators also showed values less than the agglomeration standard number, which mainly resulted from a high percent of silicate.

Figure 2.10 shows the compressive strength of dairy manure ash pellets, which can be used for an agglomeration prediction. According to Rajvanshi's study result [30] that a severe slagging is expected with a fuel containing an ash content of 12% or more, the sand mixed dairy manure after processing should avoid slagging and fouling problems. However, recent studies found that the different inorganic element compositions lead to different results as discussed earlier. The highest compressive strength from a three hour baked ash pellet was determined at around 600 ^{o}C. A similar result was also obtained by Amado et al. [113] that the highest compressive strength of a manure pellet was obtained at 600 ^{o}C, which was comparable to the strength of a cotton ash pellet showing the strongest strength at around 800 ^{o}C. The absolute strength magnitude of cotton ash was almost three time stronger than manure, which agreed with the reported bed agglomeration index results of cotton (0.04) and manure ashes (0.26).

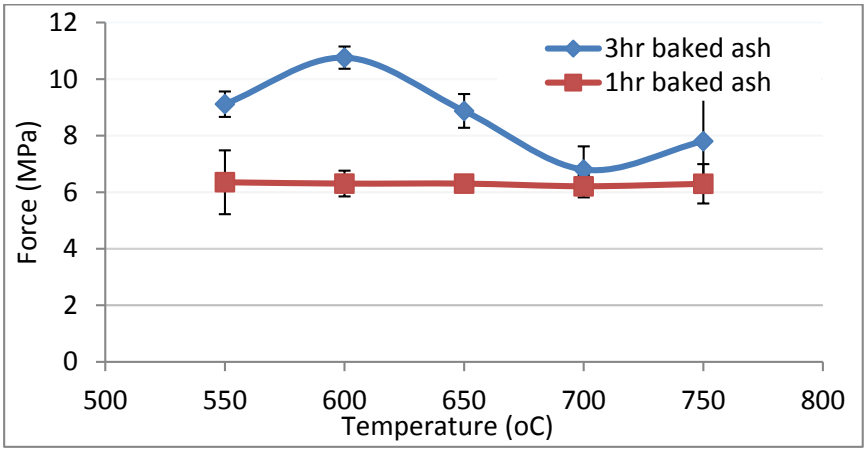

Figure 2.10. Compressive strength of baked ash pellet breakage at different conditions.

In this study, the BAI was obtained as 0.38 showing a low potential for bed agglomeration. In contrast, the processed manure ash pellet, after 1 hour baking at different temperatures, didn't show a significant strength as indicated in Figure 2.10. The result suggests a conclusion that dairy manure ash exposure to longer than 3 hour residence time at a high temperature would cause weaker bed agglomeration compared to that with lignocellulosic biomass waste like cotton gin trash. The high amount of silicate due to the water washed diary manure in an actual manure processing helps prevent bed agglomeration. Also, a keep-moving bed materials for the fluidization would break the weak agglomerated bed particles.

The 30 cm square fluidized bed reactor after a one day gasification operation with the unprocessed dairy manure was investigated. When the reactor main door was opened after 4 days of slow cooling, substantial melt-induced and coating-induced bed agglomeration formations were recognized as ash as illustrated in Figure 2.11. The case was different from the bed particle condition with the process dairy manure where there was no significant bed agglomeration. The strongest lump of bed materials was found in a location where the fuels were added. This happened for expected reasons of (a) high sand (ash) content in the feedstock, (b) the reactor after gasification wasn't fluidized enough to remove initial stage of ash agglomeration, and (c) the reactor temperature between 550 and 600 ^{o}C was maintained for a longer time. Taking these reasons into consideration, the pilot fluidized bed gasifier was operated again and again with the processed dairy manure. There was no significant agglomeration detected when the main reactor was opened. This supports the hypothesis that bed agglomeration would occur

even with a high silicate containing ash if the temperature and the exposure time are high and long enough in a stationary reactor.

(a) bed agglomeration in the reactor (b) lumps of bed materials

Figure 2.11. Agglomerated bedding materials from TAMU fluidization reactor

2.3.4. Gasification tests with processed dairy manure

The as-received manure was used for heating the pilot scale TAMU gasifier as shown in Figure 2.12 (a). However, the temperature with the unprocessed dairy manure cannot increase the bed temperature above 600 ^{o}C, and it rather decreases the temperature of the reactor. The large amount of ash (sand) in the as-received manure cooled the reactor temperature. Another problem was the fuel feeding system because of the high bulk density of the as-received manure. On the other hand, when the processed manure was used, the temperature was easily controllable and could be increased to a desirable temperature as shown in Figure 2.12 (b). Also, the feeding flow was significantly improved with the almost four times lighter bulk density of the processed manure as reported in Figure 2.9.

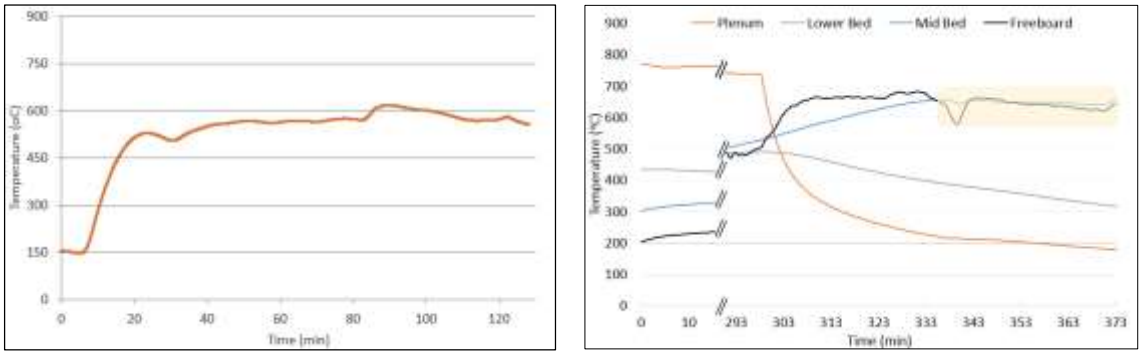

(a) (b)

Figure 2.12. Temperature profiles of a pilot-scale gasification using (a) as-received dairy manure and (b) processed dairy manure.

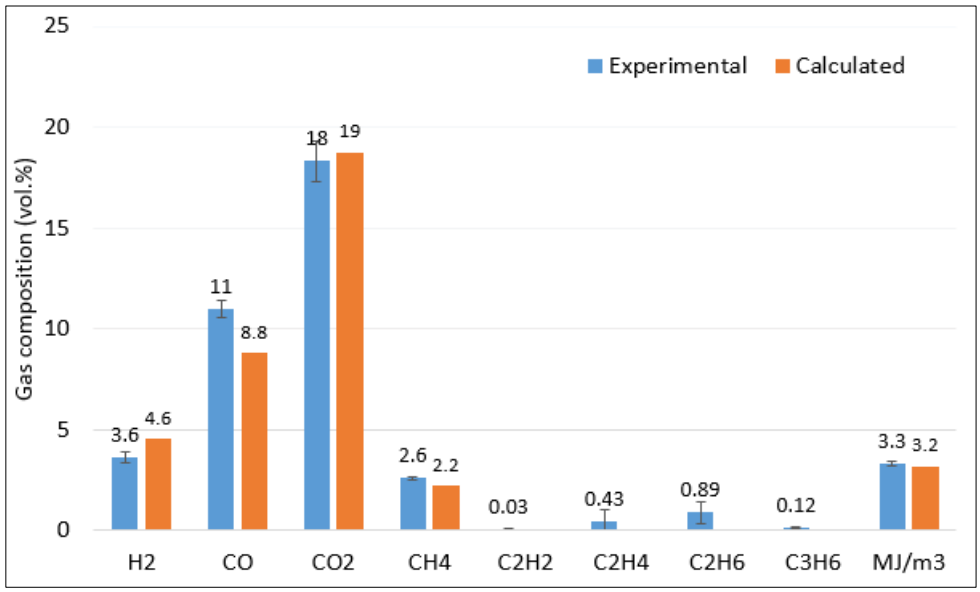

Figure 2.13. Gas compositions from a pilot-scale fluidized bed gasifier compared to the calculated gas composition developed with the bench-scale gasifier [62].

The gas compositions from the processed dairy manure at temperature ranges from 650 – 680 ºC for over 30 minutes were collected and averaged as shown in Figure 2.13. The gas produced from the pilot gasifier was successfully flared with a LHV of 3.3

MJ/Nm^3. For a further comparison, the experimentally developed model [62] of each gas composition was applied to the syngas composition from the pilot gasifier, and showed similar gas compositions. A higher CO (11%) and CH_4 (2.6%) gas composition than the calculated values the experimental data resulted in a higher gas LHV (3.3 MJ/Nm^3). A trace of hydrocarbons (1.5%) were also reported.

2.4. Conclusions

Dairy manure mixed with sand to be used as a thermal conversion fuel source was fully analyzed for a pilot scale manure handling system development and the gasification operation. An initial moisture content of less than 10% with the ground condition was the most reliable for the sand separation process by maximizing the yield and minimizing the ash content when filtered with a sieve mesh-40, which was used for the development of pilot scale sand separator. The developed pilot scale drying and sand separation systems successfully processed the as-received dairy manure as designed by recovering a 25 wt% of initial dried manure with 40 to 50% ash content. The processing rate of the developed manure handling system was evaluated, and the characterization of manure at each stage was analyzed, which would help on designing a complete waste thermochemical process. From the compressive strength examination for the bed agglomeration prediction, the temperature at 600 ^oC was shown to be the highest. However, a large amount of silicate in the ash reduced the probability of slagging and agglomeration. Finally, the sand mixed manure was successfully used for running a pilot gasifier, and the produced syngas was flared with an LHV of 3.3 MJ/Nm^3.

3. ENRICHED AIR AND STEAM FLUIDIZED BED GASIFICATION WITH SAND BEDDING DAIRY MANURE AND SYNGAS CLEAN-UP*

3.1. Introduction

Every day a dairy cow produces on the average about 8.2 kg of dry manure [127]. This gives a rough idea of the total production of dairy manure per year at about 28 million dry metric tons in the U.S. and 1.4 million dry metric tons in Texas. With the heating value of dairy manure at 15.8 MJ/kg (dry basis) [128], the total potential energy value of dairy manure is about 4.42 $x10^{11}$ MJ/year (14,000 MW) from the U.S.
Many large stall cow feedlots and dairies are using different types of bedding materials for dairy cows. If dairy manure is used for fermentation, the process usually takes at least a week to a month to obtain maximum energy yield. Even after all the reactions have been made, the amount of the waste can only be reduced by a maximum of 58% after 20 days. Still, almost 40% of the solid manure is left behind as waste or used in other ways [129].

Dairy manure gasification was recently used in a fixed bed gasifier. Gordillo and Annamalai [130] utilized dairy manure for air and steam gasification. The results showed that as more fuel was added to the reactor, it resulted in a decrease in the highest reactor temperature, energy efficiency, and CO gas production. On the other hand, the

* Reprinted with permission from "Enriched-air fluidized bed gasification using bench and pilot scale reactors of dairy manure with sand bedding based on response surface methods" by H. Nam, A.L. Maglinao, S.C. Capareda and D.A. Rodriguez-Alejandro, 2016. *Energy*, 95, 187-199 Copyright [2016] by Elsevier.

H_2, CO, and CH_4 gases were increased by adding more steam in the reactor, which also enhanced the energy efficiency and the syngas heating value. Thanapal et al. [131] also used the same reactor for dairy manure gasification with enriched air. From the air gasification, the ranges of resulting products were 2.7 – 4% for H_2, 7 – 23% for CO, and 2.2 – 4.2 MJ/Nm^3, while the ranges from the oxygen gasification were 3.5 – 6.6% for H_2, 11 – 20% for CO, 2.9 – 4.7 MJ/Nm^3. A dairy manure fluidized bed gasification was also done based on a Box-Behnken design (BBD) [132]. The LHV of syngas was obtained from 2.0 to 4.7 MJ/Nm^3 with the operating conditions of temperature (650 – 850 ^oC), ER (0.08-0.2), and steam-to-biomass ratio (0-1.76).

In this study,

1) The effects of operating conditions on the syngas quality are presented based on the response surface methodology (RSM) in order to construct the empirical equations for syngas prediction.
2) Optimal conditions are investigated for the highest heating value and energy efficiency.
3) The effect of steam on syngas compositions is evaluated to increase H_2 concentration.
4) The volumetric LHV of syngas is upgraded using an alkali solution to obtain the improved syngas quality.

3.2. Materials and Methods

3.2.1. Sample preparation an characterization

The dairy manure feedstock was obtained directly from an open field pit at the Southwest Regional Dairy Center in Stephenville, Texas. A drying of air dried dairy manure was done at 85 ^{o}C with a box type dryer (90 × 90× 180 cm) covered with a 1.3 cm thick insulation board (R-value = 3.2) until it dried to less than 1% moisture content. Then, the sand was separated from the dried dairy manure using a drum sand separator with 16 and 40 mesh sieves. The manure for the bench-scale gasification was further milled through a 2 mm sieve using a Wilely Laboratory Mill model #4.

3.2.2. Experimental setups

The enriched-air gasification experiments using processed dairy manure were done using a bench-scale gasifier and a pilot-scale fluidized bed gasifier as shown in Figure 3.1. A bench-scale fluidized bed reactor with an electric tube furnace contained the main tube reactor measuring 5 cm in diameter and 84 cm in length made of AISI 316 S.S. A feedstock hopper was connected to the lower part of the main tube reactor. A DC auger controller was used to control the speed of the dairy manure feed rate. A K-type thermocouple was installed to measure the temperature of the lower bed where the samples were added from the hopper. Two pressure tubes were placed to measure the pressures of the lower and upper beds to monitor fluidization in the reactor. The bed material used was Mulgrain 47-10 x18 (CE Minerals, Andersonville, GA) consisting of SiO_2 (50%) and Al_2O_3 (46.8%) [133], and it was sieved with -20 and +40 meshes. The

mean diameter was determined to be about 0.63 mm using USA Standard Sieves, and the particle density was 1.44 g/mL using an Accupyc 1330 pycnometer (Micrometritics). Air from a compressor and oxygen from a gas cylinder (Airgas Distribution) with corresponding flow controllers were used for these gasification experiments. A cyclone was used to separate the solid particles from the syngas. A wet scrubber was utilized to further remove finer particle matter and reduce the gas temperature. An orifice meter was placed after the scrubber to monitor the syngas flow rate. This pilot scale gasification system was described in a previous section 2.2.4.

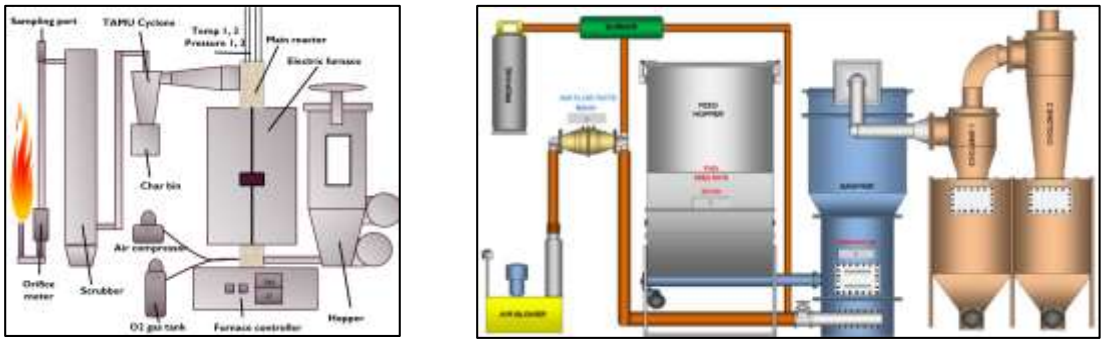

(a) Bench scale gasification system (b) TAMU pilot scale gasification system [24]

Figure 3.1. Bench scale and pilot scale gasifiers at Texas A&M University.

3.2.3. Experimental procedure and data analysis

The main reactor of the bench-scale gasifier was first heated using an electric furnace. The electric furnace, set at 500 ^{o}C, was turned on. When the main reactor reached 400 ^{o}C, air at a minimum fluidization velocity was introduced into the reactor. Then, the processed dairy manure was inserted into the main reactor to increase the temperature. Some of the experimental conditions required the electric furnace to be in

operation to compensate for the reactor heat loss. Otherwise, the bed temperature would decrease whenever the ER conditions were reached. Once the operating conditions of temperature, equivalence ratio, and oxygen percentage were met within a range of ±5% error, the produced syngas was kept flowing for about 3 min. Then, three syngas samples were collected, and the final gas product flows were recorded after the gas clean-up and cooling. In a similar manner, the reactor of the pilot-scale TAMU gasifier was heated using a propane burner until it reached 400 ^{o}C. Then, the burner was turned off and the temperature was maintained only by biomass fuel. The maximum feeding rate for the dairy manure was 8 kg/min. Due to the low heating value of dairy manure, an increase in the operating temperature was restricted due to the limited amount of dairy manure. The sampled syngas was analyzed using an SRI gas chromatograph (GC) with a thermal conductivity detector (TCD). The carrier gas was argon, and it detects the gas mixture of H_2, N_2, O_2, CO, CH_4, CO_2, C_2H_2, C_2H_4, and C_2H_6. The GC calibration was made using two different standard gases offered from Airgas Distribution at ±2%. The dairy manure feedstock was analyzed for high heating value (HHV) using a Parr bomb calorimeter, a proximate analysis following ASTM E1755 and D3172, and an ultimate analysis using a Vario MICRO elemental analyzer.

With the elemental composition from the ultimate analysis, the stoichiometric chemical reaction can be expressed in Equation (3.1). Based on the equivalence ratio (ER) of $(air/fuel)_{actual}/(air/fuel)_{stoich}$, one kg of dairy manure requires 5.54 kg of air for the stoichiometric combustion reaction. However, as enriched air was used in this study, the stoichiometric amount of air was obtained from the modified ER which replaced the

weight of air with oxygen as shown in Equation (3.2). The lower heating value of syngas, cold gas efficiency, and carbon conversion efficiency was calculated by using Equations (3.3 – 3.5).

$$C_{2.7}H_{2.5}N_{0.3}O_{1.53}S_{0.006} + 2.59(O_2 + 3.76N_2) \rightarrow 2.7CO_2 + 1.24H_2O + 9.74N_2 \quad (3.1)$$

Modified ER_m,

$$ER_m = \frac{Oxygen{:}Fuel_{actual}}{Oxygen{:}Fuel_{stoic}} \quad (3.2)$$

Lower Heating Value (LHV) of syngas,

$$LHV\left(\frac{MJ}{Nm^3}\right) = \frac{1}{100}\begin{pmatrix} 10.2 \cdot Y_{H2} + 12.0 \cdot Y_{CO} + 33.9 \cdot Y_{CH4} \\ +53.9 \cdot Y_{C2H2} + 57.0 \cdot Y_{C2H4} + 60.7 \cdot Y_{C2H6} \end{pmatrix} \quad (3.3)$$

Y_i = %mole (v/v) of syngas of each gas component

Cold gas efficiency, η_{cold} (%),

$$\eta_{cold} = \frac{M_{syngas} \times LHV_{syngas}}{M_{biomass} \times LHV_{biomass}} \quad (3.4)$$

M_j = mass flow rate (kg/min)

Carbon conversion efficiency, η_{carbon} (%) [134]

$$\eta_{carbon} = \frac{12}{22.4} \times f_{syngas} \times \frac{Y_{CO}+Y_{CO2}+Y_{CH4}+2\times(Y_{C2H2}+Y_{2CH4}+Y_{CH6})}{C\% \times M_{biomass}} \quad (3.5)$$

Y_i = %mole (v/v) of syngas of each gas component

C% = the mass percentage of carbon in the ultimate analysis of biomass fuel in dry basis

M_j = mass flow rate (kg/min)

f_{syngas} = syngas volumetric flow rate (Nm^3/min)

3.2.4. Experimental design

A response surface methodology (RSM) was used to design the experimental operating conditions of the enriched-air gasification process using Design-Expert (DX9) version 9.0.2 software (Stat-Ease Inc., USA) as shown in Figure 3.2. A Box-Behnken design (BBD) was first considered for the design of the experiments using the three operating conditions of temperature, modified equivalence ratio (ER_m), and oxygen concentrations of gasifying agents in the current study. Then, a central composite design (CCD) was added for a better understanding of the air gasification. A total of 24 runs were designed and made as there were 4 replicate points at the center of each design, 12 points at the edges of the BBD, 8 points at the edges of the CCD, and the 4 overlapping points. The lower operating conditions of temperature, ER_m, and oxygen concentration were 600 ^oC, 0.1, and 21%, while the higher operating conditions were 800 ^oC, 0.4, and 40%. However, some temperature conditions were difficult to keep exactly as it was designed due to the many other conditions that affected the changes of temperature. An analysis of variance (ANOVA) was used to evaluate the goodness of fit, which showed the proposed models were statistically significant.

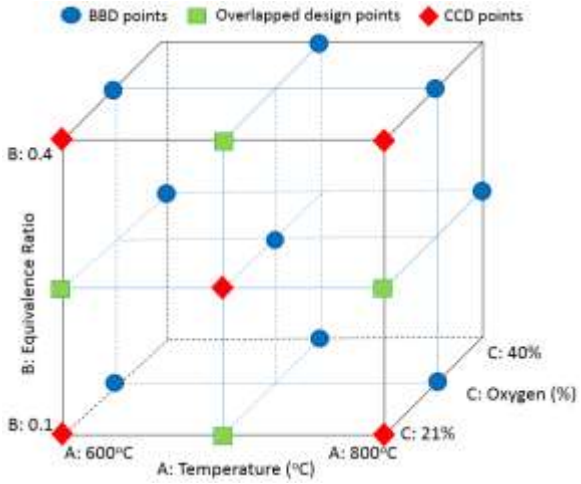

Figure 3.2. Schematic diagram of the combined statistical models of BBD and CCD points.

3.3. Results and Discussion

3.3.1. Dairy manure feedstock characteristics

The results are shown in Table 3.1. The HHV of as-received dairy manure was 8.7 MJ/kg, which is low in comparison with fresh dairy manure at 17 MJ/kg and woodchip at 19 MJ/kg. High ash content (49%) due to presence of sand is one reason for the low HHV of the as-received dairy manure. After the sand separation, the processed manure had a higher HHV of 12 MJ/kg with a 36% ash content. Still, a large variation in the standard deviation was obtained from both as-received and processed dairy manure due to the mixture of sand bedding material in the sample. The carbon contents were determined to be 17% for the as-received manure, 33% for the processed manure, and 38% for fresh manure. The chemical composition of the processed dairy manure can be expressed as $C_{2.7}H_{2.5}N_{0.3}O_{1.53}S_{0.006}$, which is needed for ER conditions.

Table 3.1. Dairy manure characteristics (db: dry basis; *:by difference).

Biomass characteristics	As-received dairy manure	Processed dairy manure	Fresh manure
High Heating Value (MJ/kg), db	8.7±1.6	12.3±1.4	17.3±0.9
Proximate analysis (wt%), db			
VCM	49.1±2.9	60.5±2.8	71.2±1.4
FC	2.2±0.8	3.6±2.7	15.2±0.8
Ash	48.8±3.1	35.9±1.7	13.6±0.8
Ultimate analysis (wt%), db			
C	16.6	32.8	37.81
H	2.27	2.48	5.37
N	1.1	4.16	2.43
S	0.23	0.21	0.58
O*	31.0	24.46	47.36
H/C	1.64	0.91	1.70
O/C	1.40	0.56	0.94

3.3.2. Effects of operating conditions on the syngas products

The enriched-air gasification was carried out and investigated under the operating conditions of temperature, ER_m, and oxygen content. Table 3.2 shows the syngas product composition of H_2, CO, CH_4, and CO_2 as well as their lower heating value (LHV). The experimental runs from 1 to 16 belonged to the BBD points for the oxygen gasification, while the runs from 13 to 24 were designed using the CCD for air gasification including temperature and ER_m operating conditions. The ranges of the volumetric syngas composition from the BBD (oxygen gasification) were 2.3 – 11.5% for H_2, 6.2 – 20.3% for CO, 1.3 – 6.1% for CH_4, and 16.8 – 31.8% for CO_2, while the ranges for the CCD (air gasification) were 2.3 – 9.1% for H_2, 6.2 – 12.8% for CO, 1.3 – 4.1% for CH_4, and 16.8 – 20.1% for CO_2. The ranges of syngas LHV from each design were 1.78 – 8.00 MJ/Nm^3 for the BBD and 1.78 – 5.74 MJ/Nm^3 for the CCD. Ranges of

syngas composition and LHV obtained from other gasification systems using dairy manure were similar or slightly smaller, from 2 to 4.6 MJ/Nm^3 [131,132,135].

Table 3.2. Syngas composition for the combination of BBD (Box-Behnken design) and CCD (central composite design) in volume percentages.

		Operating conditions				Syngas products (vol%)				
Design	runs	Temp (^{o}C)	ER_m	ER	O_2 (vol%)	H_2	CO	CH_4	CO_2	LHV (MJ/m^3)
BBD points	1	630	0.25	-	40	4.1	14.1	2.3	31.6	3.51
	2	617	0.1	-	30	3.3	10.0	1.8	26.0	2.74
	3	625	0.4	-	30	3.5	10.7	1.9	25.8	2.87
	4	708	0.25	-	30	7.1	14.5	3.3	23.8	4.85
	5	730	0.4	-	40	6.6	16.6	3.4	31.8	5.54
	6	709	0.25	-	30	7.6	15.4	2.8	25.7	4.90
	7	702	0.1	-	40	8.5	19.0	4.4	27.1	6.25
	8	790	0.4	-	30	8.2	13.7	3.5	23.5	5.02
	9	790	0.1	-	30	11.5	18.9	5.3	22.1	7.33
	10	800	0.25	-	40	11.0	20.3	6.1	26.4	8.00
	11	690	0.25	-	30	4.8	10.4	2.4	24.0	3.61
	12	700	0.25	-	30	6.5	13.0	2.6	24.5	4.34
Overlapping design points	13	620	0.25	0.3	21	2.3	7.7	1.5	19.8	2.03
	14	700	0.4	0.48	21	2.9	6.2	1.3	18.2	1.78
	15	705	0.1	0.12	21	8.4	15.3	4.1	20.1	5.67
	16	785	0.25	0.3	21	8.6	8.6	1.9	16.8	3.07
CCD points	17	600	0.4	0.48	21	2.1	5.9	1.1	20.0	1.59
	18	699	0.25	0.3	21	6.4	11.5	2.8	18.8	4.35
	19	710	0.25	0.3	21	6.0	9.4	2.3	18.2	3.47
	20	610	0.1	0.12	21	2.9	7.2	1.4	19.6	2.04
	21	683	0.25	0.30	21	4.6	9.4	2.2	19.7	3.11
	22	800	0.4	0.48	21	6.2	7.1	1.7	18.0	2.65
	23	721	0.25	0.30	21	5.5	12.8	3.3	18.8	4.54
	24	800	0.1	0.12	21	9.1	12.1	3.2	18.7	5.74

The produced syngas based on the BBD and the CCD were statistically analyzed to construct empirical prediction models using an analysis of variance (ANOVA) as shown in Table 3.3. Each model was selected with the highest order polynomial for

maximizing the adjusted R^2 where the terms were significant and the model was not aliased. Thus, the quadratic model was chosen for H_2 when a 2-factor interaction model was applied to CH_4, CO_2 and LHV. A linear model was used for the CO gas. Normally, a regression model with a p-value less than 0.05 is regarded as significant, which indicates a 95% confidence level. All the models for each variable were significant as the p-value showed less than 0.0001. Also, the effect of each term on the responses were evaluated with p-values < 0.05. Except for the LHV value, the temperature and ER_m terms of the models were highly correlated with the production of H_2, CO, CH_4, and CO_2 (p-value < 0.01), while the oxygen concentration of the gasifying agent was significantly correlated with all the dependent variables (p-value < 0.01). The oxygen content was especially significant to the production of CO, CO_2, and LHV (p-value < 0.0001). The R^2 and adjusted R^2 were used to evaluate the model. It is known that the R^2 values increase with more independent variables, while the adjusted R^2 values increase with the elimination of the insignificant variables. It is also known that the predicted R^2 indicates whether the models are overfitting a model by having too many predictors that cause random noises. The adjusted R^2 is preferred to understand the regression model [35] as the variables in some models were reduced in this study. The adjusted R^2 of the regression models were shown in excess of or close to 80%, which can be regarded as satisfactory considering the complicated chemical reactions in a bench-scale fluidized bed reactor for the enriched-air gasification process. As the model will be used for product predictions, the predicted R^2 was also used to evaluate the regression models. Since the difference between the adjusted R^2 and the predicted R^2 are less than 10%

from all models except the H_2 model, these models can be used to navigate the design space. However, even the H_2 regression model is in reasonable agreement and can be used for prediction as the difference is less than 20% [136].

The actual and coded regression coefficients for H_2, CO, CH_4, CO_2, and LHV are listed in Table 3.4. The coded coefficients are useful for comparing the relative impact of the each variable term on the responses, while the actual coefficients help to predict the actual responses with the original units. The major influencing conditions on each dependent variable were determined as temperature for H_2, CH_4 and LHV, and oxygen concentration for CO and CO_2. A further discussion on the regression coefficients will be discussed in following sections.

Table 3.3. Model validation for the response surface models using ANOVA.

Terms	H_2		CO		CH_4		CO_2		LHV	
Source	Sum of Sqr	P value	Sum of Sqr	P value	Sum of Sqr	P value	Sum of Sqr	P value	Sum of Sqr	P value
Model	143.5	0.000	310.8	0.000	31.18	0.000	403.4	0.000	54.97	0.000
A-Temp	93.93	0.000	56.51	0.001	15.37	0.000	28.43	0.000	27.89	0.058
B-ER	14.41	0.001	42.41	0.004	3.93	0.002	6.54	0.004	4.64	0.006
C-O_2	10.42	0.004	199.3	0.000	7.01	0.000	375.9	0.000	12.57	0.000
AB	4.30	0.041			1.11	0.069	0.013	0.884	3.22	0.019
AC	3.98	0.049			3.72	0.002	4.53	0.013	3.25	0.019
BC	0.064	0.788			0.014	0.832	13.45	0.000	0.17	0.557
A^2	1.42	0.218								
B^2	0.33	0.542								
C^2	0.92	0.316								
Resi.	11.92		81.26		4.99		10.01		8.17	
Cor Total	155.4		392.1		36.17		413.4		63.14	
R^2	92%		79%		86%		98%		87%	
Adj R^2	87%		76%		81%		96%		82%	
Pre R^2	74%		70%		71%		95%		76%	

Table 3.4. Actual and coded operating coefficients for the proposed response models.

	Inter	A: T	B: ER	C: O_2	AB	AC	BC	A^2	B^2	C^2
H_2 Act.	-44.8	0.11	21.71	-0.28	-0.054	9.4e-4	0.07	-6.7e-5	11.43	-4.8e-3
H_2 Cod.	6.55	3.58	-1.19	0.97	-0.80	0.94	0.11	-0.67	0.26	-0.48
CO Act.	-13.0	0.02	-12.54	0.41						
CO Cod.	13.12	2.42	-1.88	4.12						
CO_2 Act.	6.36	9.8e-3	-27.13	1.01	-2.9e-3	-9.9e-4	1.01			
CO_2 Cod.	24.1	-1.92	0.80	5.74	0.04	-0.99	1.52			
CH_4 Act.	6.08	-6.0e-3	13.86	-0.55	-0.027	9.0e-4	0.03			
CH_4 Cod.	2.91	1.41	-0.62	0.78	-0.41	0.90	0.05			
LHV Act.	-0.53	5.4e-3	24.43	-0.51	-0.046	8.4e-4	0.11			
LHV Cod.	4.40	1.90	-0.68	1.04	-0.69	0.84	0.17			

3.3.3. The effect of operating conditions on H_2 production

The response surface plots of H_2 production with independent variables of temperature and ER_m are presented with different oxygen concentrations for the gasifying agent in Figures 3.3 (a) to (c). As seen from the H_2 quadratic regression model in Table 3.4, the major influential coded coefficients contributing to an increasing H_2 production were the linear terms of temperature (A=3.6) and oxygen (C=0.97), while for a decreasing H_2 was the linear term of ER_m (B=-1.2). Thus, the highest H_2 production of 11.5% was obtained at a condition of 790 ^oC-0.1-30% (temp-ER_m-oxygen), and the lowest production of 2.1% was obtained at the operating conditions of 600 ^oC-0.4-21% from the actual data as shown in Table 3.3. From the empirical regression model, the highest H_2 production was calculated as 13.0% at conditions of 790 ^oC-0.1-40%. The effect of the increasing temperature on the increasing H_2 composition could be explained mainly by the endothermic reactions of the water-gas reaction ($C + H_2O \leftrightarrow CO + H_2$) in a higher temperature [137] as well as the exothermic reactions of the water-gas shift (CO

+ $H_2O \leftrightarrow CO_2 + H_2$) and dry reforming ($CH_4 + CO_2 \leftrightarrow 2CO + 2H_2$) [32]. Even though Han et al. [138] reported that the effect of exothermic reactions at a higher temperature are minimal on the water-gas shift reaction, the reaction takes place and increases the ratio of H_2 to CO at up to 800 ^oC. Heavy hydrocarbons in a high temperature favor H_2 production through the carbonization reaction ($C_nH_m \rightarrow {}_nC + m/2H_2$), which lowers the tar concentration as the temperature increases [135]. The high H_2 concentration was obtained at a higher temperature and a lower ER_m condition, which showed the significance of the interaction of temperature and ER_m (p-value = 0.04). The high oxygen concentration also resulted in a high H_2 gas production at a lower ER_m. This is because the increased oxidation reaction ($C + O_2 \rightarrow CO_2$, $C + 1/2O_2 \rightarrow CO$) favors hydrogen production through the water-gas shift reaction [137]. The water in tar production also helps the H_2 production reactions as it was reported that a large production of tar could be produced at a low ER_m condition. Figure 3.3 (d) shows the actual and predicted response values of the quadratic regression model. The values were placed near the linear straight line, which indicated a satisfactory regression model. Overall, a higher temperature, oxygen concentration, and a lower ER_m resulted in a high concentration of H_2 in the syngas from dairy manure gasification.

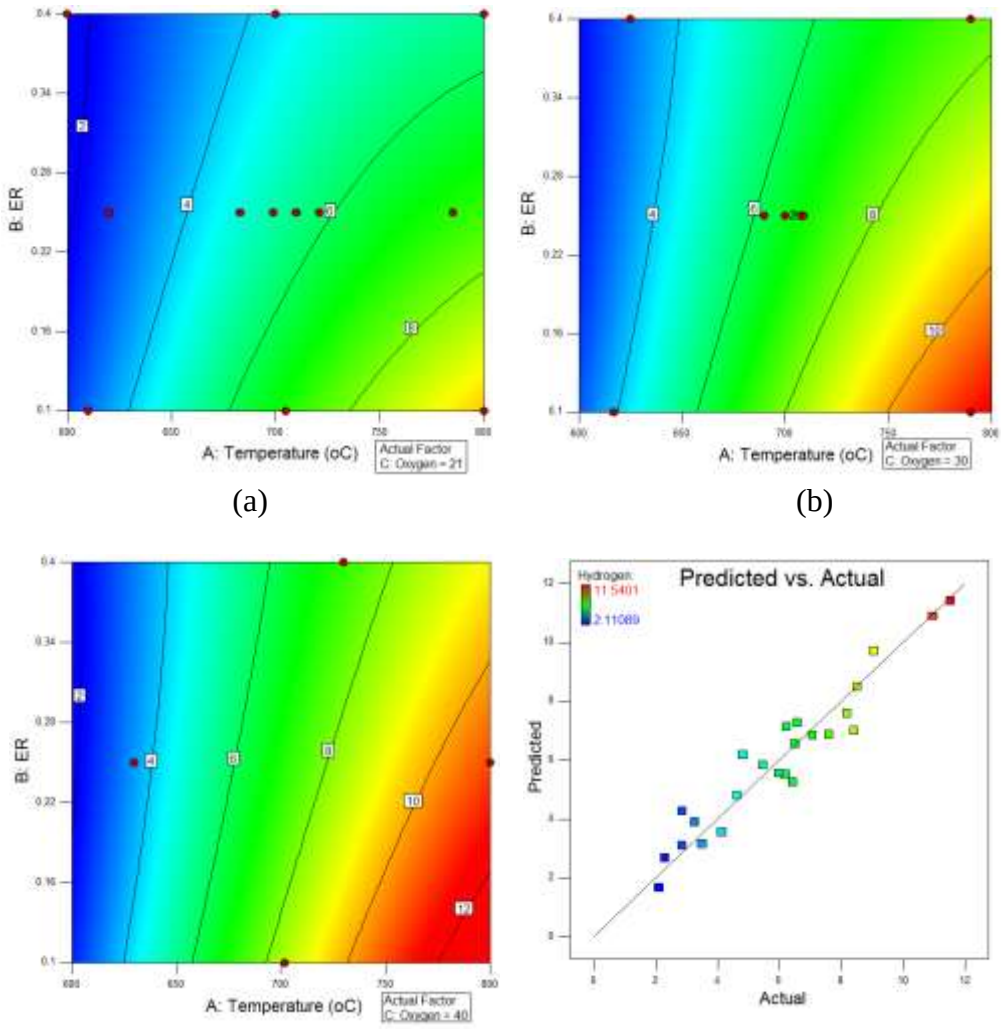

Figure 3.3.The response surface and the effect of operating conditions on H_2 production: (a) 21% oxygen (b) 30% oxygen, (c) 40% oxygen, and (d) actual vs. predicted plot.

3.3.4. The effects of operating conditions on CO and CO_2 production

The production of both CO and CO_2 were affected the most from the condition of the oxygen concentration of the gasifying agent (C = 4.12 for CO, and C = 5.74 for CO_2), followed by the condition of temperature. The effect of the rising temperature increases the composition of CO (A = 2.42) and reduces the composition of CO_2 (A = -

1.92). As the oxygen concentration was increased, the exothermic carbon oxidation reactions ($C + O_2 \rightarrow CO_2$; $C + 1/2O_2 \rightarrow CO$) were significant, which led to an increase in CO and CO_2 as shown in Figures 3.4 and 3.5. The CO gas composition variation ranged from 5.9 to 15.3% in the air gasification (21% oxygen), from 10.4 to 18.9% in the 30% oxygen gasification, and from 14.1 to 20.3% in the 40% oxygen gasification, while the CO_2 gas composition varied from 16.8 to 20.1%, from 22.1 to 26.0%, and from 26.4 to 31.8%, respectively. Overall, more CO_2 gas than CO gas was produced in this study because the range of temperatures were between 600 and 800 ^oC where oxidation reactions were more favored. Thus, the CO/CO_2 ratio obtained was below 1, ranging between 0.30 (600 ^oC-0.4-21%) and 0.85 (790 ^oC-0.1-30%). Similar trends of the ratio were found from other studies in an enriched-air gasification temperature of 700 to 950 ^oC [131] and in an air fluidized gasification temperature of 790 to 864 ^oC [36]. Thus, the increasing ratio of CO/CO_2 resulted from an increasing CO production along with an increase in H_2, mainly led by the Boudouard reaction ($C + CO_2 \rightarrow 2CO$), and the water-gas reaction ($C + H_2O \leftrightarrow CO + H_2$). Also, at a higher temperature, the reverse water-gas shift reaction ($CO + H_2O \leftrightarrow CO_2 + H_2$) [139] and the reaction of CO_2 and tar ($Tar + CO_2 \leftrightarrow xCO + zH_2$) would contribute to a high CO production [34].The ratios of the H/C and O/C of feedstock also affected the composition of the syngas in that a lower hydrogen and oxygen content in fuel can cause a lower production rate in H_2 and CO gases as discussed in a previous study [63]. For comparison, the author also conducted an air gasification with woodchips containing H/C (1.72) and O/C (0.74) ratios, which produced a higher concentration of H_2 (14%) and CO (25%) gases at 800^oC than did the

processed manure containing H/C (0.91) and O/C (0.56) ratios, which produced 9% of H_2 and 12% of CO gases at an 800°C-0.1-21% condition.

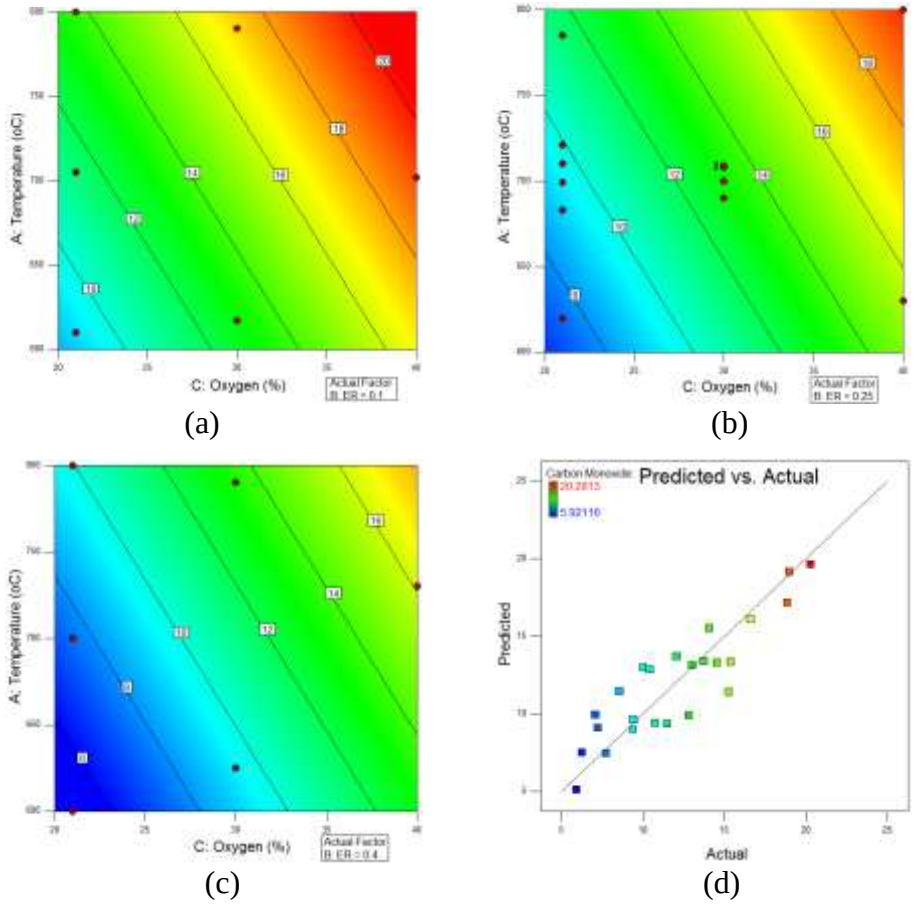

Figure 3.4. The response surface and the effect of operating conditions on CO production: (a) 21% oxygen (b) 30% oxygen, (c) 40% oxygen, and (d) actual vs. predicted plot.

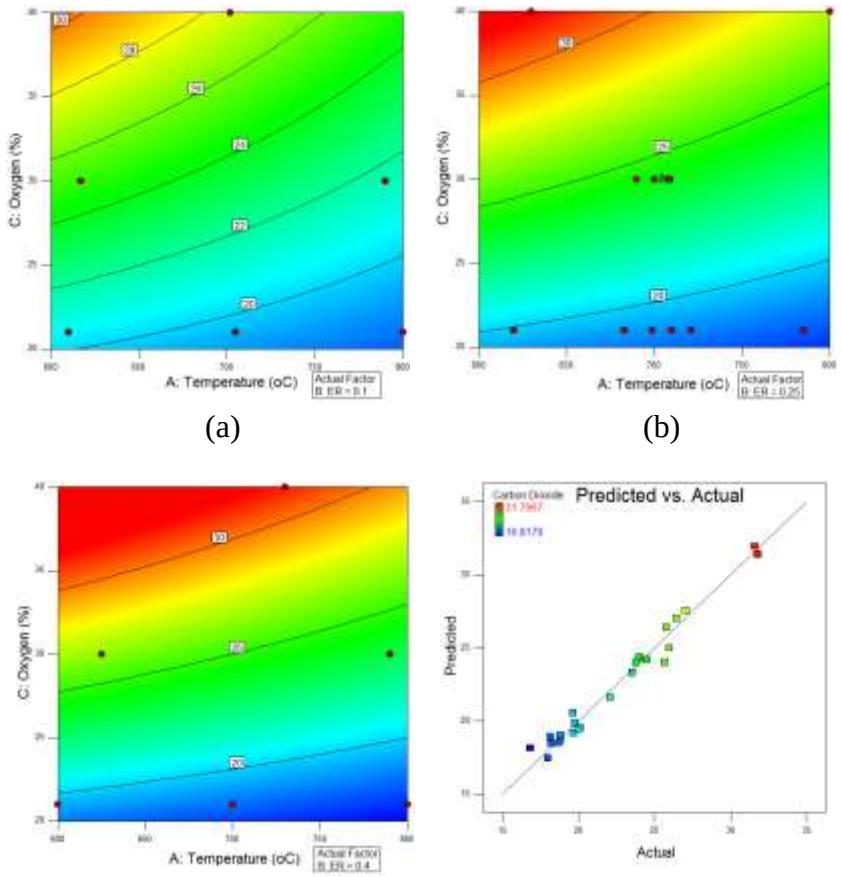

Figure 3.5. The response surface and the effect of operating conditions on CO_2 production: (a) ER=0.1, (b) ER=0.25, (c) ER=0.4, and (d) actual vs. predicted plot.

3.3.5. The effect of operating conditions on LHV (MJ/Nm^3) and CH_4 production

The lower heating value (LHV) was calculated with gas compositions as shown in Figure 3.6. The actual LHV ranged from 1.59 to 5.74 MJ/Nm^3 for the air gasification, and from 2.74 to 8 MJ/Nm^3 for the oxygen gasification. The highest actual experimental LHV (8 MJ/Nm^3) was produced at the operating conditions of 800 ^{o}C-0.25-40% (Temperature-ER$_m$-oxygen). Within the range of the operating conditions, the optimum condition for the highest expected LHV was obtained as 9.3 MJ/Nm^3 at 800 ^{o}C-0.1-40%.

The operating conditions of temperature (A=1.9) and oxygen (C=1.04) were the major independent variables determining the changes in the LHV, followed by the ER_m (B=-0.68) condition, which showed similar trends to the coefficient of CH_4 production (A=1.41, B=-0.62, and C= 0.78). Also, both the empirical equations for the LHV and CH_4 were significantly fit to a 2 factor interaction model. The increasing trends in CH_4 production with increasing temperature shown in this study is opposite to the trends in a thermodynamic equilibrium study [140]. This could be because the endothermic dehydrogenation reaction ($pC_xH_y \rightarrow qC_nH_m + rH_2$) that includes tar cracking was not considered in the equilibrium study, which increases the light hydrocarbons. Other studies also reported similar CH_4 production trends from a manure fluidization gasification with air alone [132] and air/water [141]. Also, a higher oxygen concentration intensifies the oxidation reactions, and the high temperature helps in breaking the molecular bonds through the chemical endothermic reactions of Boudouard, water-gas, dry reforming, and carbonization, which mainly increases the gas composition of H_2, and CO. The syngas heating value ranges of manure air gasification were similarly reported as 2.0 to 4.7 MJ/Nm^3 [132] and 2.2 to 4.2 MJ/Nm^3 [131]. Thus, the higher the temperature and oxygen concentration with a lower ER_m, the higher the production of LHV and CH_4.

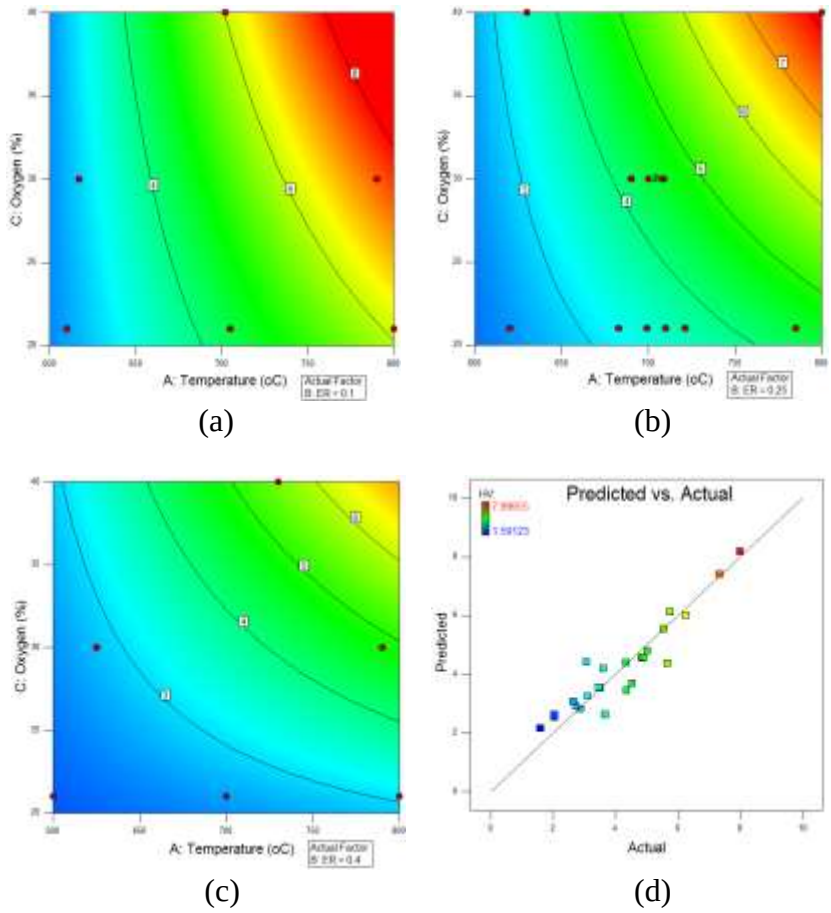

Figure 3.6. The response surface and the effect of operating conditions on LHV: (a) ER=0.1, (b) ER=0.25, (c) ER=0.4, and (d) actual vs. predicted plot.

3.3.6. Application of the empirical equations from a bench-scale reactor to a pilot-scale mobile gasification system

A pilot-scale FBG system built at TAMU was operated using processed dairy manure obtained from Tarleton State University. Figure 3.7 shows the experimental syngas compositions to compare with the syngas data obtained from the empirical equations developed from the previous sections. A similar syngas composition was predicted with less than 10% error with H_2, CH_4, and LHV, while CO and CO_2 gas

compositions showed a 30% difference for the maximum. However, when the sum of CO and CO_2 gas composition is compared, the error between syngas from the empirical equations and the experimental syngas compositions from the pilot gasifier reduces to less than 3%. It is possible that a thermal equilibrium was not closely achieved with a bench-scale gasifier as it does not have enough space and time for the further secondary reactions of syngas followed by the first oxidant reaction. In the pilot scale reactor, the produced CO_2 reacts with carbons through a Boudouard reaction to produce more CO, which help in producing hydrogen as well at a high temperature [137].

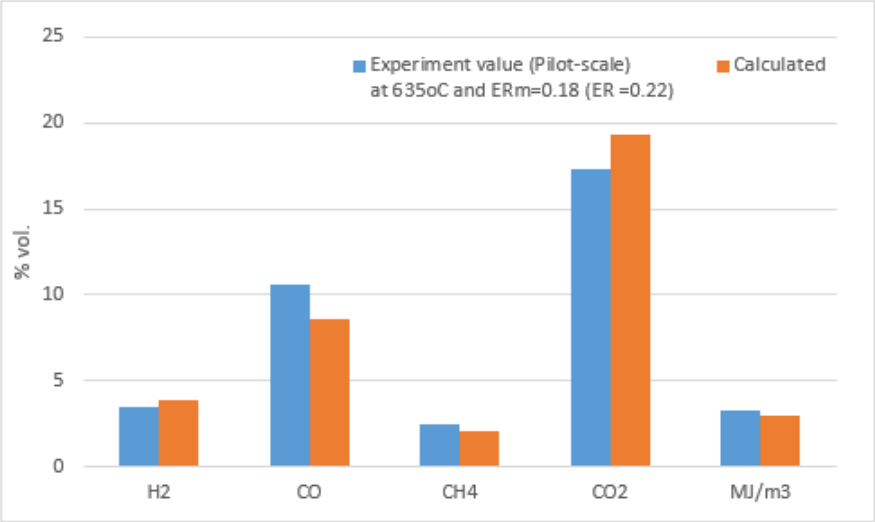

Figure 3.7. Air gasification using a pilot-scale mobile gasifier and its comparison with calculated values from the proposed empirical equations. (Experiment conditions of 635 ^{o}C and ER_m = 0.18)

3.3.7. The effect of steam on gasification syngas

Steam gasification with the processed dairy manure was investigated to increase the H_2 gas composition. By injecting the produced steam into the reactor, more steam

related reactions of a water-gas reaction, a water-gas shift reaction, and a methanation reaction took place in the reactor. The effect of the presence of steam was found significant at a higher temperature followed by the effect of temperature, as indicated in Figure 3.8. The increased hydrogen after the reactions decreased the amount of hydrocarbons accordingly. And the reaction was more active at a higher temperature. The 6% H_2 was improved to 7% with air gasification, while the 6% H_2 was increased to close to 8%. If other conditions of ER varied, the changed H_2 would be even greater.

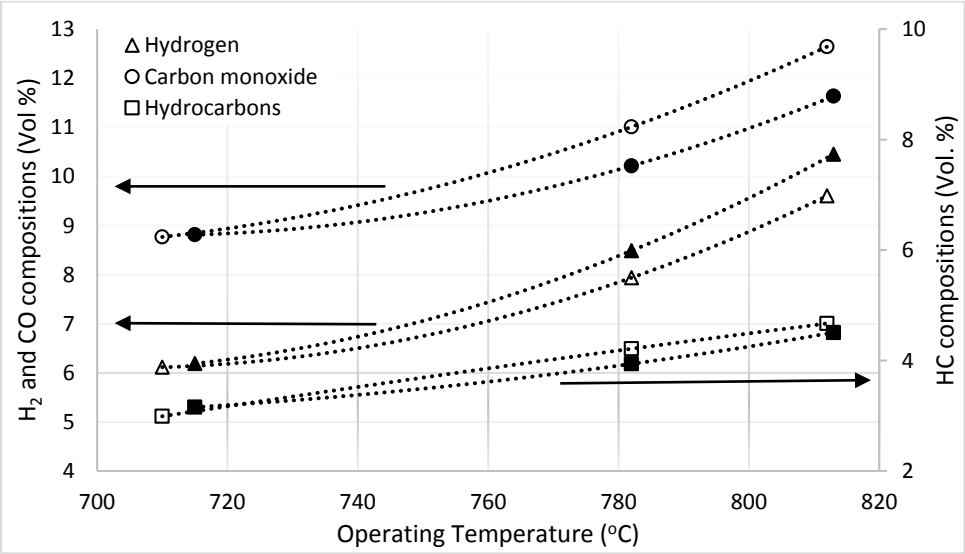

Figure 3.8. Steam gasification syngas composition of H_2, CO, and C_nH_n.

Table 3.5 shows the variation of the H_2/CO ratio and LHVs at different temperatures of air and steam gasification. As the H_2 increased and CO decreased with increasing temperature, both of the gasifications showed increased H_2/CO ratios. However, the steam operated gasification showed even greater variations on the ratio

changes from 0.7 to 0.9 of H_2/CO. In contrast, the variation of gas compositions with the presence of steam did not much affect the LHVs.

Table 3.5. H_2/CO ratio and LHV from steam gasification.

	No Steam			Steam		
	710	782	812	715	782	813
H_2/CO	0.70	0.72	0.76	0.70	0.83	0.90
LHV, MJ/Nm^3	2.93	3.91	4.47	3.02	3.91	4.37

3.3.8. Cold gas and carbon conversion efficiency

The cold gas and carbon conversion efficiencies were determined by considering the heating value of the produced syngas and the produced syngas composition using Equation (3.4) and Equation (3.5). The efficiencies of the selected operating conditions are shown in Table 3.6 (cold efficiency p-value = 0.004 and carbon efficiency p-value = 0.003). Cold gas efficiency was mainly influenced by the operating condition of temperature as the ranges of efficiency were shown from 18 to 34% for 600 ^oC, from 40 to 45% for 700 ^oC, and from 46 to 63% for 800 ^oC. A large production of H_2, CO, and CH_4 gas products at a higher operating temperature resulted in an increased cold gas efficiency (p-value = 0.009). At the different oxygen concentrations of the gasifying agent, the cold gas efficiency was determined as 18 – 46% for air (21% oxygen), 19 – 59% for 30% oxygen, and 32 – 63% for 40% oxygen, which was statistically insignificant. Wu et al. [132] reported a similar range of cold air gasification efficiency from 15 to 30% using a dairy manure fluidization gasification system. Also, Thanapal et al. [131] obtained a cold efficiency from 17 to 73% from a 10 kW fixed bed gasification

facility using dairy manure. The highest cold gas efficiency was obtained at a condition of ER_m = 0.25 at temperatures of 600, 700, and 800 °C. The experiments indicated that a better cold gas efficiency was obtained with syngas containing a low concentration of CO_2 as was also reported by Zainal et al. [142].

Table 3.6. The effect of operating conditions on the carbon and cold gas efficiencies.

Temp (°C)	ER_m	Oxygen (vol%)	Steam	Cold Eff. (%)	Carbon eff (%)
630	0.25	40	×	32	78
617	0.1	30	×	19	46
620	0.25	21	×	34	81
610	0.1	21	×	18	45
730	0.4	40	×	44	89
709	0.25	30	×	45	77
702	0.1	40	×	40	66
715	0.28	21	O	38	67
782	0.28	21	O	54	80
790	0.1	30	×	59	81
800	0.25	40	×	63	90
800	0.1	21	×	46	73
813	0.28	21	O	46	83

When it comes to carbon conversion efficiency, the ER_m condition had the most effect on the efficiency variations compared to other conditions of temperature and oxygen concentration (p-value = 0.0049). First, when the ER_m was decreased, the carbon conversion efficiency was reduced to 45% at the operating condition of 600 °C-0.1-21% from 90% at the condition of 800 °C-0.25-40%, which was a result of the incomplete

conversion of the solid fuels into volatile gases. The lowest ER_m condition can be close to the pyrolysis process that produced more bio-oil (or tar) and bio-char. It was reported that a large amount of tar at the lowest ER was produced in a fluidized bed biomass gasifier with up to 9.5% of fuel mass [143]. Also, Herguido et al. [144] observed that tar yield was 2-8 % of fuel mass in the range of 640 – 800 ^oC in a steam gasification process. Second, the oxygen concentration of the gasifying agent can also increase the carbon efficiency up to 90%, due to a large production of CO and CO_2. The composition of CO_2 gas at a 40% oxygen condition produced over 30% syngas. Last, a low temperature, under 700 ^oC, was not high enough to support a heavy hydrocarbon breakdown ($pC_xH_y \rightarrow qC_nH_m + rH_2$). A lower temperature resulted in a low conversion efficiency due to a reduction in the reaction rate [145]. A gasification equilibrium study determined that the carbon gasification efficiency varied the most with ER rather than with the oxygen concentration in the gasifying agent [146].

3.3.9. Syngas upgrading

Various materials were applied to find the CO2 gas removals for upgrading the LHV of gas. Airgas standard gas was initially used for the experiment using four different adsorbents. A molecule sieve Type 5A removed all the hydrocarbons, while the activated carbon removed all the hydrocarbons except for CO gas as shown in Table 3.7. The KOH solution and Shirasagi carbon successfully and selectively reduced only the CO_2 gas from 17% to less than 1.5% by passing off other gases.

Table 3.7. Inflammable removal of CO_2 gas using various methods.

	STD gas	1M KOH solution	Shirasagi Carbon*	Molecule Sieve (Type 5A)	Activated Carbon
H	8	8.5	9.2	14.1	10.5
O_2	1	1.2	1.6	1.6	2.1
N_2	47.25	57.4	56.9	84.3	69.9
CO	20	23.9	24.0	0.0	17.5
CH_4	5	5.8	5.8	0.0	0.0
CO_2	17	1.5	0.5	0.0	0.0
C_2H_4	1.5	1.7	1.9	0.0	0.0
C_2H_6	0.25	0.0	0.3	0.0	0.0

* (MSC 3R-181)

Figure 3.9 shows further CO2 removal experiments and the rate of use of KOH and Shirasagi carbon. The 19% CO2 gas in 1 ml/min flow of standard gas saturated the 200 ml KOH solution in 20 minutes and the 120 cm^3 carbon in 10 minutes. A better performance was found from the KOH solution than the Shirasagi carbon.

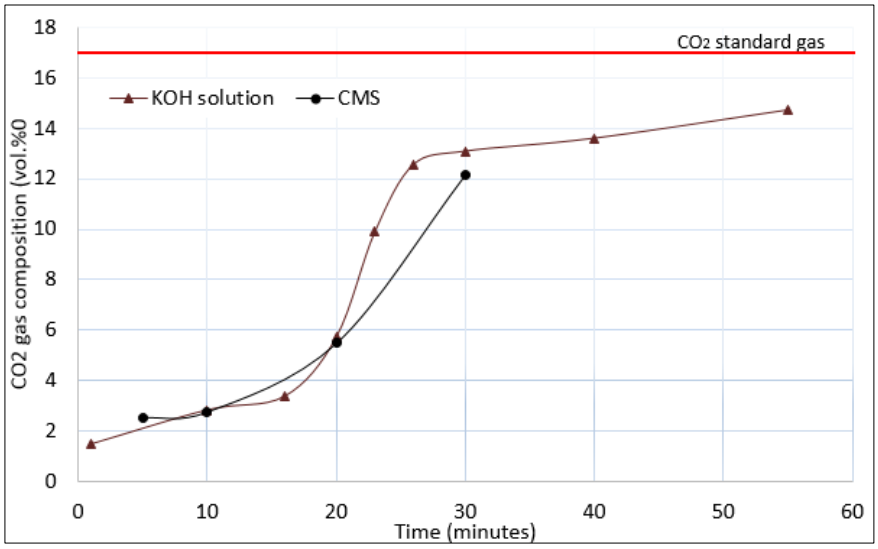

Figure 3.9. CO2 removals using KOH solution and Shirasagi MSC carbon.

The produced syngas was put through a scrubber containing four spray nozzles for gas cleanup and upgrading coupled with a bench scale gasifier. The syngas at a temperature of 680 ^{o}C for air gasification and 670 ^{o}C for oxygen gasification was upgraded using 1M of alkali solution. The CO_2 composition in the syngas was almost removed from both the air and oxygen gasification process, which resulted in a relative increase in the other gasses as shown in Figure 3.10. This helped to enhance the quality of the syngas by about 40% from air gasification and 89% from oxygen gasification. As more CO_2 was included in the syngas from the oxygen gasification, a much higher increase in syngas energy content was achieved. The LHV of the produced syngas was recommended to be greater than 4.2 MJ/m^3 for engine use according to Shah et al. [147]. The syngas upgrading process helped a low quality syngas to be useful for power generation.

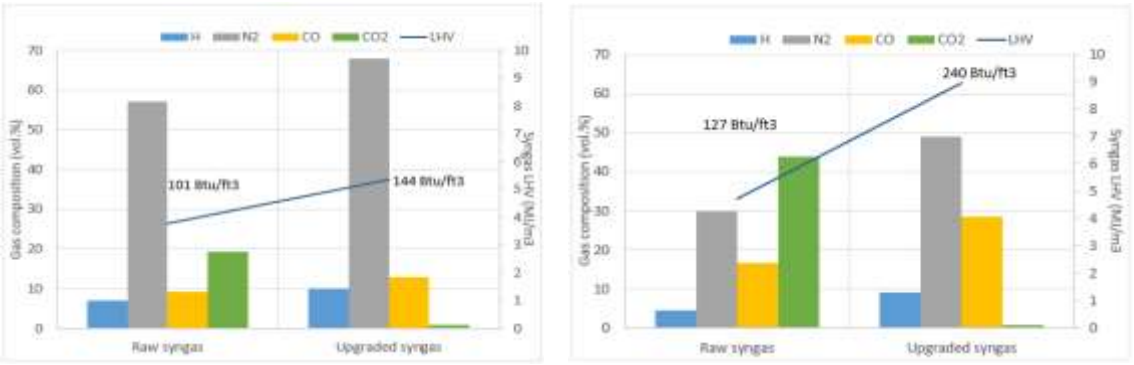

1. Air gasification (b) Oxygen gasification

Figure 3.10. Syngas upgrading using a 1M alkali solution.

3.4. Conclusions

Enriched-air fluidized bed gasification was performed using processed dairy manure that originally included a high ash content due to sand bedding. The combination of CCD and BBD for a statistical analysis was applied to understand the effect of temperature, ER_m, and oxygen concentration on the syngas and the LHV in a bench-scale reactor. The effect of temperature was the most significant on all the syngas compositions, LHV, and cold gas efficiency. On the other hand, the effect of ER significantly influenced the carbon conversion efficiency. The operating conditions necessary to obtain the highest LHV for syngas of 8.0 MJ/Nm^3 from dairy manure oxygen gasification were 800 ^oC-0.25-40% (temperature-ER_m-oxygen), while the maximum LHV from the air gasification was 5.7 MJ/Nm^3 obtained at the condition of 800 ^oC-0.1-21%. The ranges of the cold gas efficiency and carbon conversion efficiency were 19 – 63% and 45 – 90%, respectively. The empirical equations obtained from the bench-scale experiments were used to compare the syngas data produced from a fluidized bed pilot-scale TAMU gasifier. The steam gasification was conducted and produced increased H_2 gas at a higher temperature (800 ^oC), while a minimal change in H_2 yields was observed at a lower temperature. The syngas upgrading by removing CO_2 gas was successfully conducted with an alkali solution and Shirasagi carbon. The LHVs after upgrading were increased from 101 Btu/ft^3 to 144 Btu/ft^3 for air gasification, and from 127 Btu/ft^3 to 240 Btu/ft^3 for oxygen gasification.

4. EXPERIMENTAL INVESTIGATION OF TORREFACTION OF AGRICULTURAL WASTES (RICE STRAW AND COTTON STALK)*

4.1. Introduction

Torrefaction is a thermochemical process with a temperature range from 200 ^{o}C to 300 ^{o}C and a condition of no oxygen, and is sometimes referred to as mild-pyrolysis. Many studies used the chemical composition of a lignocellulosic biomass to understand the relationship of mass and energy yields with such conditions as temperature, residence time, moisture, and input gas type [41-44]. Among the chemical compounds of cellulose, hemicellulose, and lignin, lignin is the most difficult component to convert chemically [148]. Agricultural biomass with a high lignin (>15%) composition includes corn stalk, bagasse, cotton stalk, and hardwood stems, while others with a low lignin (<15%) composition are wheat straw, rice straw, grass, and paper [148,149].

The specific objectives in this study were to,

(a) find the optimized conditions for the highest energy yield between CS and RS and to determine its potential as an alternative energy source for gasification and combustion,

* Reprinted with permission from "Experimental investigation of torrefaction of two agricultural wastes of different composition using RSM (Response Surface Methodology)" by H. Nam and S.C. Capareda, 2015. *Energy*, 91, 507-516, Copyright [2015] by Elsevier.

(b) compare the extent of solid energy densification between two biomass to evaluate the possibility of alleviating difficulties of storage and transportation, and

(c) discover the influencing conditions of each biomass torrefaction using a response surface methodology.

4.2. Materials and Method

4.2.1. Sample preparation and characterization

Twelve samples of Rice straw (RS) were obtained from Bourbon, CA, and twelve samples of cotton stalk (CS) were collected from Boswell, CA for this study. The biomass was initially dried in the open air for more than a month. Then, the air-dried samples were milled and passed through 5-mm screens using Wilely Laboratory Mill model #4. The high heating value (HHV) of the sample was analyzed by using a PARR isoperibol bomb calorimeter according to ASTM E711. A proximate analysis and moisture content was done in accordance with ASTM standard D 3173, D3175 and E1755. A Vario MICRO Elemental Analyzer was used to determine the ultimate analysis, ASTM D5373. The structural compositional analysis of rice straw and cotton stalk samples was conducted using the NREL LAP #42617 and NREL LAP #42618.

4.2.2. Experimental facility

Torrefaction experiments were conducted using a bench-scale batch type Parr pressure reactor (Parr Instrument Company, Moline, IL). The 5.7 liter AISI 316 stainless

steel batch was heated with a cylindrical electrical heater. One J type thermocouple was placed inside the batch reactor and the other was located inside electric heater around the batch. A reactor controller (Parr Instrument Company, Moline, IL) was used to control the temperature inside the reactor. A condenser of a water jacketed tube was connected to the end port of the reactor and had a liquid vessel to collect condensable volatiles. The remaining incondensables went through a gas meter (METRIS 250, Itron, Oweenton, KY) to measure the volumetric gas flow rate after calibration to torrefied gas. Approximately 250 g of cotton stalk and 300g of rice straw were used for the torrefaction experiment each time. Then, N_2 gas was inserted into the reactor for 20 minutes to remove the air from the reactor. An internal stirrer was operated to mix the sample evenly. The electrical heater heated the reactor at approximately 5 ^oC/min until the set temperature (210, 250 or 290 ^oC) was reached. The residence time at the set temperatures was 20, 40 or 60 minutes.

4.2.3. Analytical methods

The torrefied solids from the torrefaction experiment was analyzed for their HHV and an ultimate analysis using the Parr bomb calorimeter and Vario MICRO Elemental analyzer. The proximate analysis and moisture content analysis were done with the torrefied solid products by again following ASTM E1755, E3175 and D3173. Both the solid and liquid products were analyzed using a Shimadzu IRAffinity-1 FTIR Spectrophotometer. The condensable liquid products were also analyzed for moisture content by using a KF Titrino 701 (Metrohm, USA Inc.) in accordance with the ASTM

E203 and its chemical composition was analyzed using a GC-MS using Shimadzu QP2010Plus. The GC column used was ZB5MS 30 m length × 0.25 mm diameter with a 0.25 µm thickness. The injector temperature was set at 280 ^{o}C and the split ratio was 50:1. The system was programmed to hold first 30 ^{o}C for 3 min, increase to 50 ^{o}C at 1 ^{o}C/min, increase to 75 ^{o}C at 2 ^{o}C/min and increase to 170 ^{o}C at 10 ^{o}C/min for 5 min. The ion source and the interface temperature were set at 250 ^{o}C and 200 ^{o}C. The gas product was obtained from each torrefaction run and analyzed to find its composition with a gas chromatograph (GC, SRI Multiple Gas Analyzer MG #1). A Thermal Conductivity Detector (TCD), 6' Molecular Sieve 13X 80/100 (2mm ID SS, Restek), and a 2 m ShinCarbon ST 80/120 (2mm ID SRI 8610C, Restek) was mounted on the GC. Argon was used as a carrier gas. The GC condition was set at 40^{o}C and then increased to a final temperature of 280 ^{o}C. The detectable gases from the GC were H_2, N_2, O_2, CO, CH_4 and CO_2.

Table 4.1. Central composite face-centered experimental design matrix.

No.	Coded variable level		Temperature (^{o}C)	Time (minutes)
	Temperature	Time		
1	-1	-1	210	20
2	+1	-1	290	20
3	-1	+1	210	60
4	+1	+1	290	60
5	-1	0	210	40
6	+1	0	290	40
7	0	-1	250	20
8	0	+1	250	60
9	0	0	250	40
10	0	0	250	40
11	0	0	250	40
12	0	0	250	40

4.2.4. Experimental design and data analysis

The central composite design (CCD) is one kind of response surface methodology (RSM) developed in the 1950s [150]. Two influential factors on torrefaction (temperature and residence time) were used in this study. Central composite face-centered (alpha value = 1) was chosen as a CCD option. The number of experiments of each sample was 12 runs as it includes two design factors with two levels, four axial runs, and four center runs (Table 4.1). The coded levels of 210, 250, and 290 ^{o}C temperature and 20, 40, and 60 minutes were marked with -1, 0, and +1.

The analysis of variance (ANOVA) was used to understand the fitness of the regression models with a 95% confidence level. This analysis helped determine if the mean of the results is significantly different or not. All the models were chosen by reducing the terms using both backward and stepwise model selection to avoid collinearity problems, which can result in large standard errors, poor numerical accuracy, and wrong partial regression coefficients.

The following equations are used for the data analysis in this study. Mass and energy were balanced with consequent losses. Energy yield shows the magnitude of the energy conversion of the initial biomass after the torrefaction, while the mass product yield represents the mass conversion of the process. The energy density of torrefied solid products represents the ratio between the increased energy yield and the converted mass yield.

$$\text{Product yield (\%)} = m_{torrefied} / m_{initial} \quad (4.1)$$

Char yield (%) + Liquid yield (%) + Gas yield (%) + Loss (%) =100% (4.2)

Energy yield (%) = $(m_{tor} \times HHV_{tor})/(m_{initial} \times HHV_{initial})$ (4.3)

Energy density = E_{energy_yield} (%) / $m_{product\_yield}$ (%) (4.4)

4.3. Results and Discussion

4.3.1. Sample characteristics

Two agricultural residues, rice straw (RS) and cotton stalk (CS) were analyzed and the results are presented in Table 4.2. The proximate analysis of the rice straw and cotton stalk samples showed that the high volatile combustible matter (VCM) and fixed carbon (FC) contents were similar or a little higher to what others found for rice straw (72 – 77% VCM, and 6 – 15% FC) [49,151,152], and cotton stalk (75% VCM, and 16% FC) [43]. The VCM content of rice straw is higher than that of cotton stalk while the fixed carbon (FC) and ash of rice straw is lower than that of cotton stalk. Since the VCM components mainly react under high temperatures over 200 ^{o}C, the amount can affect the changes of torrefied solid mass and energy. On the other hand, FC and ash are the main components of the remaining solid products after the release of the VCM, which contributes to large amounts of solid mass yield after the torrefaction process. The high heating value (HHV) of both biomass was determined to be 18.95 MJ/kg for RS and 16.90 MJ/kg for CS. The ultimate analysis supports the HHV of RS, which includes a higher carbon content. The H:C and O:C molar ratio of CS were revealed as 1.65 and 0.87, which are higher than the values of RS (H:C 1.61 and O:C 0.81). Compared to the average oxygen content (40 – 44%) of wood in a dry-ash free condition [153], the RS

and CS have a higher oxygen content (around 50%), which can be expected to produce more oxygenated volatile compounds than wood. The chemical composition of RS and CS can be expressed as $CH_{1.61}O_{0.81}N_{0.004}S_{0.003}$ and $CH_{1.65}O_{0.87}N_{0.018}S_{0.002}$, respectively.

Table 4.2. Rice straw and cotton stalk characteristics. *db* : dry basis *daf*: dried ash free

Biomass Characteristics	Rice straw	Cotton stalk		Rice straw	Cotton stalk
HHV (MJ/kg), db	19.0±0.4	16.9±0.1	*Compositional analysis (wt%), db*		
Moisture (wt%)	9.6±0.6	10.1±0.2	Extractives	15.2±0.1	17.5±1.1
			Water extractives	12.7±0.2	14.4±0.9
Proximate analysis (wt%), db			Ethanol extractives	2.52±0.1	3.15±1.1
VCM	79.6±0.5	76.8±1.5	Lignin	14.7±0.3	20.1±0.6
Fixed Carbon	15.9±0.6	16.8±1.7	Acid solubes	0.02±0.0	0.01±0.0
Ash	4.09±0.5	6.45±2.0	Acid insolubles	14.7±0.3	20.1±0.8
Ultimate analysis (wt%), daf			Protein	2.54±0.3	12.8±0.1
C	45.0±0.3	43.1±0.8	Structural HC	55.4±3.4	36.5±1.4
H	6.03±0.0	5.94±0.1	Glucan	34.4±2.5	27.2±1.5
N	0.23±0.0	0.90±0.0	Xylan	17.4±0.4	4.37±0.8
S	0.30±0.1	0.23±0.0	Galactan	1.15±0.5	1.58±0.2
O (by difference)	48.4±0.4	49.9±0.6	Arabinan	2.50±0.5	3.38±0.9

A compositional analysis of each biomass was also conducted to better determine the thermal conversion by the decomposition of lignocellulosic materials into the products. Five components that constitute the biomass are cellulose, hemicellulose, lignin, extractives, and protein. Cotton stalk (CS) contains four times less xylan (4.4 wt%), a major hemicellulose monomer unit, than rice straw (RS, 17.4 wt%). On the

other hand, lignin, a highly branched large polyaromatic compound, was larger in CS than in RS due to its characteristics as a woody type agricultural biomass. The amount of cellulose can be predicted from the weight of glucan since it is a polymer of glucose. The larger protein content (12.7%) and extractive content (17.5%) of CS can be a big contributor to an amount of nitrogen four times larger in CS than in RS as determined by ultimate analysis [154]. Possible main components of water extractives contain inorganic materials, non-structural carbohydrates, and nitrogenous materials, whereas ethanol extractives include waxes, chlrophyll, starches, and pigments [155]. The rice straw compositions revealed in the previous studies [156,157] were reported as 32 – 47% cellulose, 19 – 27% hemicellulose, and 5 – 24% lignin. Another study [158] using the NREL standard biomass analytical procedures reported 20% lignin, 36% glucan, 11% xylan, and 10% other components. For the composition data of cotton stalk, the weight percentages of compositions from previous studies [159,160] are close to those reported in Table 4.2.

4.3.2. Product yields

Torrefaction experiments, the thermal decomposition of low energy density lignocellulosic biomass of rice straw (RS) and cotton stalk (CS), were conducted to examine the effects of temperature (210, 250 and 290 ^{o}C) and residence time (20, 40, and 60 minutes). Each experiment was identified with the biomass name-temperature-residence time (for example, RS210-40). The yellow color of the biomass started to become brown at the lower temperature and darkened at the higher temperature. Also,

the longer the torrefaction residence time, the darker the color of the biomass. Generally, with torrefied lignocellulosic products, the yield of both solid products decreased with higher temperatures while the yields of liquids and gases increased, as shown in Figure 4.1. The yields of products were also similarly affected by the different residence times. The product yields are related to the thermal reaction of cellulose, hemicellulose, and lignin content in each biomass at the different temperatures and residence times. Bergman et al. [161] proposed that hemicellulose starts to decompose at 200 ^{o}C and extensive decomposition occurs above 250 ^{o}C to 300 ^{o}C, while the extensive decomposition of cellulose happens between 305 ^{o}C and 375 ^{o}C, and lignin decomposes between 250 ^{o}C and 500 ^{o}C. Other studies reported a slightly different range in decomposing temperatures for hemicellulose (200 – 250 ^{o}C), cellulose (240 – 350 ^{o}C) and lignin (280 – 500 ^{o}C) [26]. In the present work, the yield of solid products at the 210 ^{o}C, 250 ^{o}C and 290 ^{o}C with a 40 minute residence time were shown as 81.1%, 68.7% and 52.5% for rice straw and 87.1 %, 72.7% and 52.5% for cotton stalk. A significant weight loss for rice straw as opposed to cotton stalk took place at 210 ^{o}C and 250 ^{o}C because rice straw contains four times more xylan (a main component of hemicellulose) than cotton stalk, as shown in Table 4.2. Other torrefaction studies also reached similar conclusions [4,41]. Moderate biomass weight loss was obtained as the residence time increased at temperatures of 210 ^{o}C and 290 ^{o}C compared to the large weight loss at 250^{o}C from both biomass. This can easily be explained by the large decomposition of hemicellulose that mainly takes place at around 250 ^{o}C [162]. This also supports other studies that found that hemicellulose decomposes from around 250 ^{o}C [161].

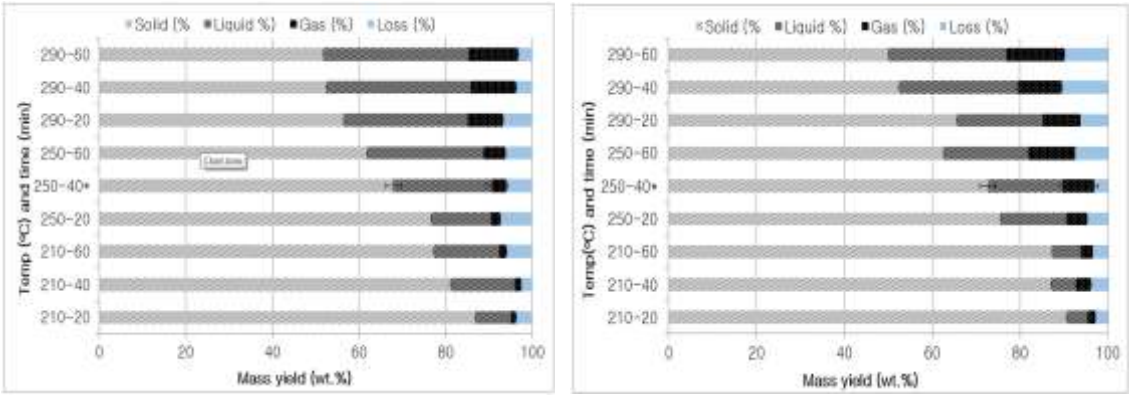

(a) Rice straw (b) Cotton stalk

Figure 4.1. The product yield of solid, liquid, and gas. *average value

The equations shown below, in terms of actual factors, present the volatiles of the condensable and non-condensable portions as a result of a mass conversion increase with torrefaction temperature and residence time. The increase of RS volatile products was linearly augmented depending on each independent condition of temperature and residence time (linear model p-value <0.0001), while the CS mass conversion took place with the interaction factors of temperature and time, the 2-factor interaction model (2FI p-value <0.0001). However, based on the code factors, temperature effects have the most influence in the torrefaction process compared to time and temperature interaction terms.

$$\text{RS mass conversion (wt\%)} = -73.40 + 0.36 \times \text{Temp.} + 0.27 \times \text{Time} \quad (4.5)$$

$$\text{CS mass conversion (wt\%)} = -42.32 + 0.23 \times \text{Temp.} - 0.67 \times \text{Time} + 3.66\text{E-}3 \times \text{Temp} \times \text{Time} \quad (4.6)$$

Significant changes of volatile mass yields (liquid and gas) were noticed at the different temperatures, while the yields at different times did not always constantly

increase. For both RS and CS volatile products, at the temperatures of 210 ^{o}C and 290 ^{o}C, a significant decrease of volatile mass yields occurred between 20 and 40 minutes, whereas a moderate decrease of mass yields was detected between 40 and 60 minutes. However, the gas and liquid yields of RS and CS at 250 ^{o}C constantly decreased.

4.3.3. Torrefaction solid product characteristics

Figure 4.2 presents the proximate analysis and the heating value of solid products at different conditions. The volatile combustible matter (VCM) decreased from 79.6% for raw RS to 44.5%, and 78.1% for raw CS to 48.1% at the conditions of 290 ^{o}C and 60 minutes, which was the most severe condition. Similar to the product yield shown in Figure 4.2, the decrease rate of the VCM from both biomass at different conditions were affected more by temperature than residence time. The decrease in the slope of the VCM percentages for RS was steeper than that for CS. One possible reason is because the xylan content of RS is four times higher than that of CS. Another reason can be the more reactive property of the rice straw. Wang et al., 2011 [163] found similar results with VCM degradation with wheat straw and cottons stalk. Also, it was observed that minimal changes in the VCM contents occurred between the conditions of 290-40 and 290-60 of both biomass. On the other hand, the relative amount of fixed carbon (FC) and ash contents to the VCM content increased. The decreased VCM content and increased FC content caused an enhanced high heating value (HHV, dry basis) of both products from 19.0 MJ/kg for raw RS to 28.60 MJ/kg and 16.90 MJ/kg for raw CS to 23.13

MJ/kg for torrefaction at 290 ºC for 60 minutes. This is an HHV augmentation of 50% for RS and 37% for CS from raw biomass.

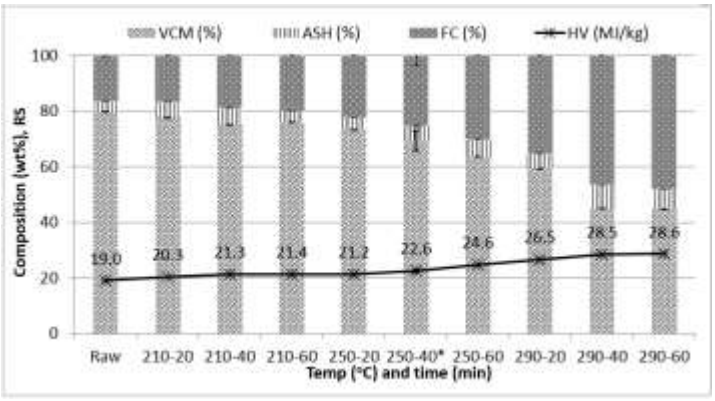

(a) Rice straw

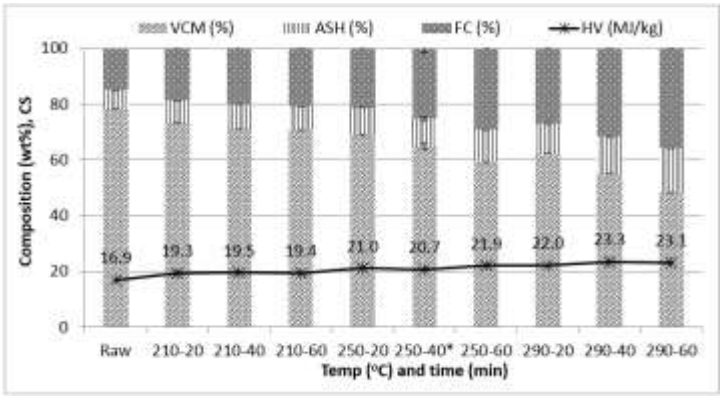

(a) Cotton stalk

Figure 4.2. Proximate analysis and its HHV of torrefied RS and CS products at the different temperature and residence time conditions. *average

The following empirical equations in terms of actual factors for HHV show how the conditions and heating value are related. The RS heating value can be determined depending largely on the effects of the temperature term and the second-order effect of temperature (modified quadratic model P-value < 0.0001), while both temperature and

time terms are considered linearly to determine the CS heating value (linear model p-value<0.0001).

$$\text{RS HHV (MJ/kg)} = 76.34 - 0.53 \times \text{Temp.} + 0.055 \times \text{Time} + 1.24\text{E-}3 \times \text{Temp.}^2 \quad (4.7)$$

$$\text{CS HHV (MJ/kg)} = 8.62 + 0.045 \times \text{Temp.} + 0.024 \times \text{Time} \quad (4.8)$$

An ultimate analysis was also conducted to find the content of C, H, N, S and O (by difference) of torrefied products, as shown in Table 4.3. With the higher temperature and the longer time, an increase in carbon content and a decrease in oxygen, hydrogen and nitrogen contents were found in both biomass. The removal of the hydroxyl radical group from the hemicellulose can be one reason for the decreased hydrogen and oxygen as the temperature increases as Nguila Inari et al., 2007 [164] reported. However, the RS and CS carbon content at 210 ^{o}C increased slightly along with the different residence times. This verifies a previous study that most hydrogen, C–C and C–O bonds form into volatile liquid or gas products between 200 ^{o}C and 250 ^{o}C [165].

A Van Krevelen diagram was used to understand the application of char as fuel and is shown in Figure 4.3. The lower the O/C and H/C ratio, the higher the energy of the products. The torrefaction process reduced the raw RS O/C atomic ratio from 0.81 to 0.24 (RS 290-60) and the H/C atomic ratio from 1.61 to 0.89 (RS 290-60), while the O/C atomic ratio of CS decreased from 0.87 to 0.21 (CS 290-60) and the H/C atomic ratio from 1.65 to 0.94 (CS 290-60). The atomic ratio of torrefied RS (above 210 ^{o}C) and CS (above 250 ^{o}C) are comparable to sawdust [166]. The atomic ratio of torrefied products

at 290 ºC can be used as a substitute for brown coal and peat as the torrefied products are located between them.

Table 4.3. Ultimate analysis of RS and CS solid products after torrefaction process at the different conditions (*daf*: dry ash free basis and * by difference).

daf	Raw	210 ºC			250 ºC			290 ºC		
wt%	RS	20min	40min	60min	20min	40min ag	60min	20min	40min	60min
C	45.0	53.6	54.0	54.4	54.7	60.1±1.3	60.7	60.4	65.3	71.5
H	6.03	6.32	6.22	6.04	6.15	5.9±0.06	5.94	5.86	5.95	5.30
O*	48.4	39.5	39.2	39.0	38.6	33.6	32.9	33.3	28.4	22.6
N	0.23	0.25	0.26	0.27	0.22	0.29±0.01	0.31	0.31	0.31	0.43
S	0.30	0.32	0.31	0.30	0.28	0.17±0.02	0.18	0.13	0.13	0.14

daf	Raw	210 ºC			250 ºC			290 ºC		
wt%	CS	20min	40min	60min	20min	40min ag	60min	20min	40min	60min
C	43.1	51.2	52.7	53.1	55.3	57.1±1.2	61.6	59.2	63.8	72.0
H	5.94	6.25	6.05	6.07	6.16	6.1±0.08	5.81	5.87	5.82	5.64
O*	49.9	41.4	39.9	39.4	36.9	35.1	30.7	33.1	28.3	19.9
N	0.90	1.00	1.17	1.13	1.38	1.31±0.008	1.52	1.42	1.73	2.04
S	0.23	0.20	0.24	0.27	0.27	0.31±0.25	0.36	0.33	0.39	0.45

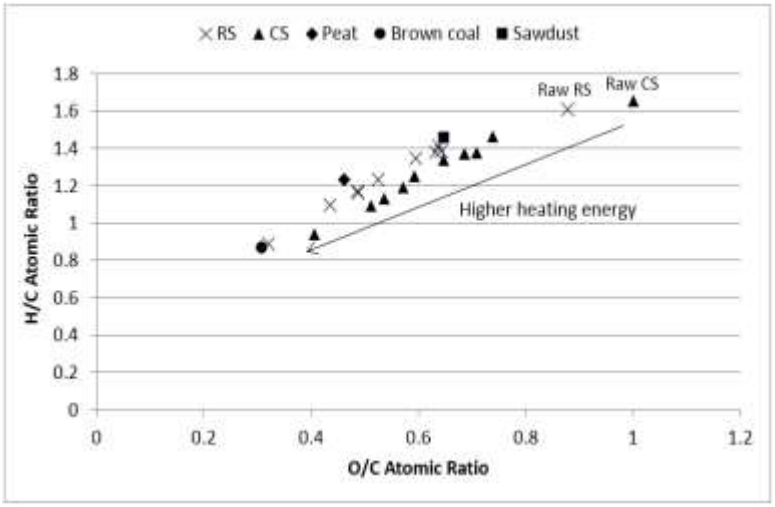

Figure 4.3. Van Krevelen diagram in daf. (Peat, brown coal and peat adapted from E. Kurkela et al. [39]).

Fourier transform infrared spectroscopy (FTIR) was used to understand the chemical structure changes of torrefied products from raw biomass. The magnified FTIR spectra from 850 cm^{-1} to 1800 cm^{-1} of torrefied rice straw and cotton stalk is shown in Figures 4.4 (a) and (b).

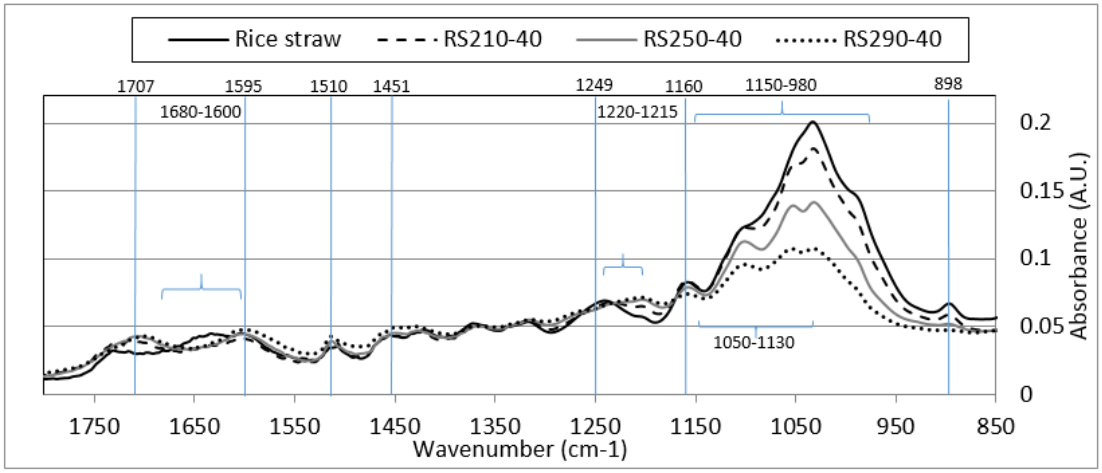

(a) Rice straw

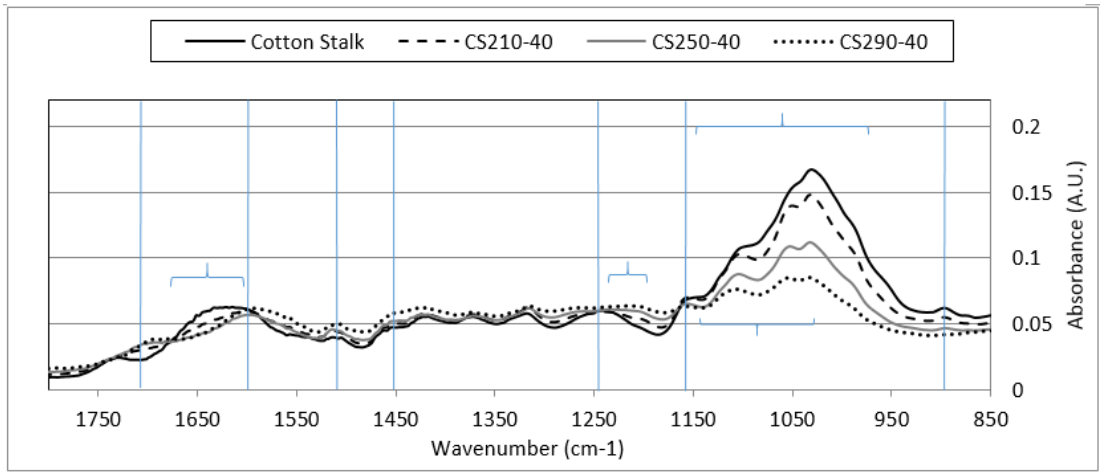

(b) Cotton stalk

Figure 4.4. FTIR spectra of the torrefied solid products of the magnified spectra between 1800 and 850 cm^{-1}.

Some important peaks from previous studies [41,158,159,167] were used to explain the chemical changes of the torrefied char in the present study. Due to the different composition of both biomass, the FTIR spectra changes after the torrefaction treatment appear dissimilar. As the temperature condition increased, there were large decreases in the rice straw and cotton stalk bands at 3350 cm^{-1} (the O-H stretch) assigned to various polysaccharides and alcohols and at 1150-980 cm^{-1} of the C-O stretch of starch (1130-1050 cm^{-1} for intense polysaccharides), which was assigned to cellulose [168]. Also, the reduced spectra at 897-898 cm^{-1} of the C-H deformation from both torrefied biomass was led by the cellulose decrease [41]. The FTIR band from 1680-1600 cm^{-1} reported as a C=O stretch of carboxylic acid, the esterified pectin, was found to decrease after the torrefaction process of both products [168]. This was because pectin consists of many polysaccharides that easily decompose under heat treatment. On the other hand, several peaks related to the lignin of torrefied RS and CS increased; 1595 and 1510 cm^{-1} (a C=C stretch of aromatic skeleton vibrations), and 1215-1220 cm^{-1} (a strong vibration of C-C, C-O and C=O stretches) [169]. Also, the 1707 cm^{-1} peak increased, which is assigned to the C=O ester–including compounds attached to hemicellulose or to the carboxyl stretch of lignin at 1705-1720 cm^{-1}). The augmented lignin composition of the torrefied biomass resulted in an increased heating value and energy density because of the ether and C-C linkages in the lignin, which has a higher energy than any other bonding. This result is similar to the one found by Jae-Won Lee et al., 2012 [44]. The band at 1249 cm^{-1} assigned to the syringly ring and the C-O stretch in lignin and xylan was shifted to a lower wavenumber of 2000cm^{-1}, similar to other bands

at 1625 and 1735 cm^{-1}. This means there were chemical changes around the functional groups after the torrefaction treatment [170,171]. The study by P. Rousset et al., 2011, [170] found a similar trend of spectrum changes in that 1720, 1599, 1511, 1451, and 1239 cm^{-1} bands increased after bamboo torrefaction treatment. FTIR bands of both torrefied products from 1300-1480 cm^{-1} assigned to C-H deformation and C-O stretch for outer surface-suberin/cutin increased after torrefaction treatment [168]. Larger spectrum changes for cotton stalk in this range compared to that of rice straw indicate that cotton stalk contains relatively more outer surface-suberin/cutin composition.

4.3.4. Torrefaction liquid product characteristics

The liquid products produced by torrefaction have an irritating smell and a brownish color. The higher the torrefaction temperature, the darker the brownish color of the liquid products. As hemicellulose and cellulose were the main decomposed components, the main liquid products should be related components of cellulose and hemicellulose. After the dehydration reaction at 100 ^{o}C, a depolymerization reaction takes place at 150 ^{o}C [161]. Then a limited devolatilzation and carbonization of hemicellulose starts at the torrefaction reaction temperature (from 200 to 300 ^{o}C). Figure 4.1 shows that the largest amount of the decomposed liquid product was obtained at the most severe condition (290 ^{o}C-60 minutes). This can also be supported by the smallest amount of water inclusion at 290 ^{o}C (74% water for RS and 77% water for CS) as shown in Table 4.4 since the other remaining liquid product portions are supposed to consist of organic components such as acids, ketones, furans, and phenols. Water composition

showed a decreasing trend as the severity became higher. Different amounts of water content were mainly determined by the degree of dehydration, which occurred through the release of the hydroxyl group during the thermal treatment.

Table 4.4. Relative chemical compounds of liquid products obtained from torrefaction process at different conditions.

	Rice straw, 40min			20min	Cotton stalk, 40min			20min
	210°C	250°C	290°C	250°C	210°C	250°C	290°C	250°C
Water[a]	83.76	81.10	74.64	82.02	87.20	87.26	76.68	91.03
Acids[b]	34.90	43.80	55.98	38.80	33.44	30.21	25.22	16.10
Ketones[b]	14.82	12.48	10.63	15.14	13.02	16.70	18.04	21.53
Furans[b]	39.30	34.43	26.08	36.12	45.75	41.19	40.96	42.18
Phenols[b]	10.98	9.30	7.30	9.94	7.79	11.90	15.78	20.19

[a] Weight (%)
[b] Relative content (%)

The chemical composition of the liquid products of the rice straw and the cotton stalk was analyzed using GC-MS after a liquid-liquid extraction with nitrile acetate. Table 4.4 summarizes the group of identified compounds while Table 4.5 shows the relative percent area of the identified peaks of RS and CS liquid products at the condition of 250 °C-40 minutes. The main chemicals from both biomass torrefactions were acids, ketones, furans, and phenols. The relative percentages of identified chemical groups were largely influenced by the amount of lignin, hemicellulose, and cellulose contained in the biomass. Accordingly, the hemicellulose and cellulose content of RS was the main contributor of the grouped composition, while the lignin and protein content of CS was the leading effecter. For this reason, the structural hydrocarbon

related acid compounds of the RS liquid product increased significantly with an increase in the torrefaction temperature and time, while the relative peak values of ketones, furans, and phenols decreased. The representative acid chemical was acetic acid, which was led by the acetoxy groups attached to the xylose unit [172]. In contrast, the amount of ketones and phenols in cotton stalk was augmented with an increase in torrefaction temperature. Phenols mainly consisted of 2-methoxy-phenol and phenol. Those main identified compounds after torrefaction were similar to the previous wood torrefaction study; acids for acetic acid and propionic acid; ketones for 2-propanon; furans for furfural and 2-furanmethanol [41]. Another study also found 2-methoxy-phenol (gauiacol), 2,6-dimethoxy-phenol (syringl) and 2-methoxy-4-alkyl-substituted phenol from lignin torrefaction [173].

Table 4.5. Relative chemical compositions of the liquid products at 250 ^{o}C-40 minutes, identified from GC-MS.

Ret. Time	Chemical compounds (RS 250^{o}C-40min)	Relative content (%)	Chemical compounds (CS 250^{o}C-40min)	Relative content (%)
	Acids	*43.80*	*Acids*	*30.21*
3.57	Acetic acid, anhydride with formic acid	43.53	Acetic acid	29.42
3.93	-	-	Propanoic acid, 2-methyl-, methyl ester	0.79
26.70	Hexanoic acid, phenyl ester	0.26	-	-
	Ketones	*12.48*	*Ketones*	*16.70*
3.54	-	-	2-Propanone, 1-hydroxy-	2.17
3.97	2-Pentanone	0.49	-	-
4.24	2,3-Pentanedione	1.41	2,3-Pentanedione	2.14
4.54	2-Butanone, 3-hydroxy-	0.96	2-Butanone, 3-hydroxy-	1.34
6.80	1-Hydroxy-2-butanone	1.60	1-Hydroxy-2-butanone	2.69
7.85	Cyclopentanone	0.69	-	-
13.89	2-Propanone, 1-(acetyloxy)-	4.10	2-Propanone, 1-(acetyloxy)-	4.92
16.62	2-Cyclopenten-1-one, 2-methyl-	0.59	2-Cyclopenten-1-one, 2-methyl-	0.13
17.20	Ethanone, 1-(2-furanyl)-	1.02	Ethanone, 1-(2-furanyl)-	0.67
23.97	2-Butanone, 3,3-dimethyl-	0.44	2-Butanone, 3,3-dimethyl-	0.87
24.34	2-Butanone, 1-(acetyloxy)-	0.62	2-Butanone, 1-(acetyloxy)-	0.31
36.12	2-Cyclopenten-1-one, 3-ethyl-2-hydroxy-	0.56	2-Cyclopenten-1-one, 3-ethyl-2-hydroxy-	0.91
36.38	-	-	4-Hexen-3-one, 4,5-dimethyl-	0.55
	Furans	*34.43*	*Furans*	*41.19*
5.98	2-Methoxytetrahydrofuran	0.55	2-Methoxytetrahydrofuran	1.02
10.67	Furfural	29.99	Furfural	30.54
12.57	-	-	2-Furanmethanol	3.37
23.12	2-Furancarboxaldehyde, 5-methyl-	1.71	2-Furancarboxaldehyde, 5-methyl-	1.74
28.23	2-Furanmethanol, tetrahydro-	2.18	2-Furanmethanol, tetrahydro-	4.52
	Phenols	*9.30*	*Phenols*	*11.90*
26.50	Phenol	1.29	-	-
35.94	Phenol, 2-methoxy- (gauiacol)	4.31	Phenol, 2-methoxy- (gauiacol)	7.43
40.01	Phenol, 4-ethyl-	1.20	Phenol, 4-ethyl-	1.66
40.50	Phenol, 2-methoxy-4-methyl-	0.77	Phenol, 2-methoxy-4-methyl-	1.03
42.61	Phenol, 4-ethyl-2-methoxy-	1.15	Phenol, 4-ethyl-2-methoxy-	1.78
44.03	Phenol, 2,6-dimethoxy- (syringyl)	0.57	-	-

4.3.5. Torrefaction gas product characteristics

A summary of gas products after the torrefaction process at various conditions are shown in Figure 4.5. The major gases produced from the reaction were CO, CO_2, and traces of CH_4 and H_2.

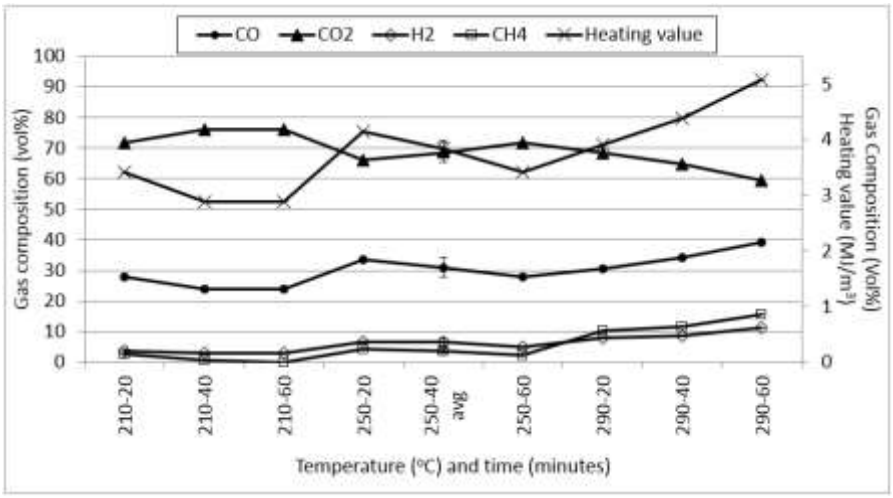

(a) Rice straw

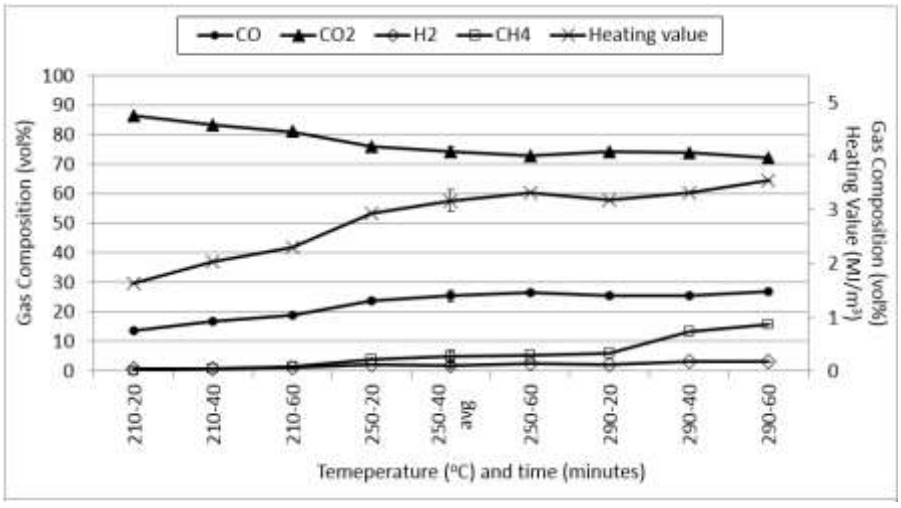

(b) Cotton stalk

Figure 4.5. Gas components at different torrefaction conditions and their heating value.

The concentration of combustible gas (CO, H_2, and CH_4) tended to increase as the temperature and time conditions increased, while the non-combustible gas (CO_2) decreased. The main reason for the increase in CO_2 was caused by the decarboxylation reaction of the acetyl group connected to the xylan chain (hemicellulose structure) of rice straw and cotton stalk [4,174]. On the other hand, the production of CO can occur for several known reasons. The CO_2 can be converted into CO through the secondary reactions of CO_2, and the reaction between steam (H_2O) and char (C) in a high temperature and pressure condition [41]. Another possible reason is because of the decomposition of carbonyl compounds at an elevated temperature [174]. These reactions increased the content of CO, H_2 and CH_4. The rate of thermal reactions of rice straw are expected to be more reactive than that of cotton stalk because the slope of the RS gas compositions with each condition is larger compared to the slope of the CS gas compositions. This obviously affects the heating value changes at each condition of the RS and CS gas products. The highest gas heating values of RS and CS were observed as 5.08 and 3.55 MJ/m^3 at 290 ^oC-60 minutes, respectively. The main contributor of high gas energy is the large portion of CO (39 vol% and 4.7 MJ/m^3) and lower portion of CO_2 (59 vol%) at the 290 ^oC-40 minutes condition, while the CS gas composition had CO (27 vol% and 3.2 MJ/m^3) and CO_2 (72 vol%) at the same conditions. The energy contents of H_2 and CH_4 are very minimal to the total gas content of RS and CS after the torrefaction process.

4.3.6. Energy yield

The energy yield of torrefied solids, liquids, and gases shown in Figure 4.6 was calculated as a percent energy yield, which represents the magnitude of the energy conversion of the initial sample after the torrefaction process.

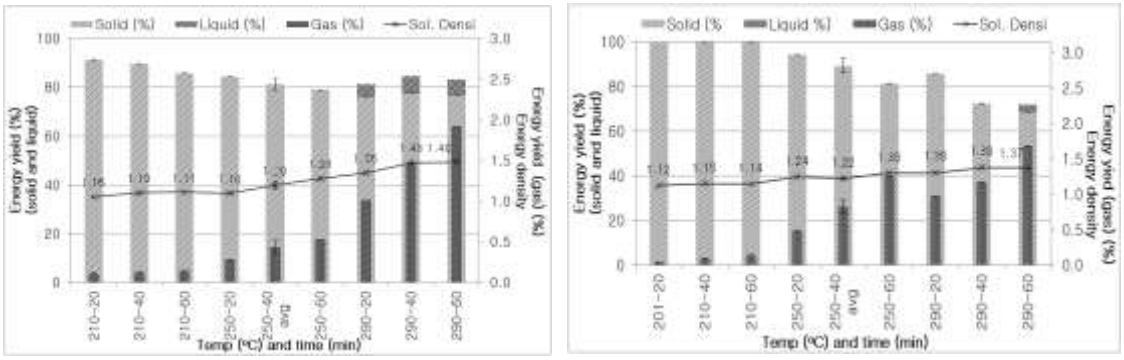

- Rice straw (b) Cotton stalk

Figure 4.6. Energy yields and energy density of solid products at different torrefaction conditions.

The highest solid energy yields of torrefied RS (91.3%) and CS (99.4%) were obtained at the 210 ^{o}C-20 minutes condition and it decreases to 76.61% of RS and 68.45% of CS at 290 ^{o}C-60 minutes. The CS solid energy yield abruptly decreases at 40 minutes at each temperature in a way similar to the product yield, while the RS solid energy yield steadily decreases along the time condition. This means that the CS begins to complete the thermochemical conversion at a point of time between 20 to 40 minutes. A woody type biomass similar to cotton stalk can obtain a relatively high energy yield under 250 ^{o}C compared to a general agricultural biomass like rice straw. A similar trend

was observed by Wang et al. [163] for the energy yield of the solid char of cotton stalk and wheat straw.

The release of volatile compounds rich in oxygen and hydrogen shown in Table 4.2 leads to an increase in the energy yield. The increased gas and liquid yields at severe conditions support the energy conversion of structural components of raw biomass to increase the heating value of torrefied char. However, only some of the torrefied liquid energy at severe conditions was analyzed since many of them had an energy content too low to be analyzed.

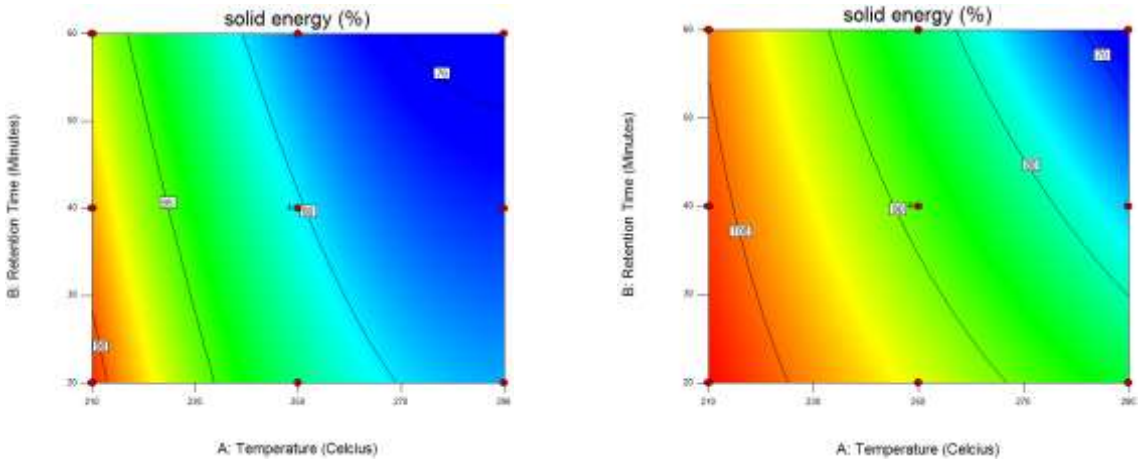

31 Rice straw (b) Cotton stalk

Figure 4.7. Contour plots of torrefied solid product energy yield (%).

The empirical models for the solid energy yield of RS and CS were obtained as follows and the contour plots are illustrated in Figure 4.7. The RS energy yield equation includes a second-order temperature term as its RS solid heating value models (modified quadratic model < 0.0001). This indicates that the RS energy yield is more affected by

heating values than mass conversion. In contrast, the effect of the CS mass conversion is larger than the effect of the increased heating value on the CS solid energy yield as it includes a 2-factor interaction term as shown below (2FI model < 0.0001).

$$\text{RS solid energy yield (\%)} = 230.3 - 1.02 \times \text{Temp.} - 0.099 \times \text{Time} + 1.75\text{E-}3 \times \text{Temp}^2 \quad (4.9)$$

$$\text{CS solid energy yield (\%)} = 120.6 - 0.09 \times \text{Temp.} + 1.09 \times \text{Time} - 5.36\text{E-}3 \times \text{Temp} \times \text{Time} \quad (4.10)$$

Energy densification is one important advantage of the torrefaction process. The energy density of torrefied solid products represents the ratio between the increased energy yield and the converted mass yield. The energy density values after the torrefaction process ranged from 1.05 to 1.48 for RS and from 1.10 to 1.37 for CS. At the condition of 250 ^{o}C – 40 minutes, the energy density slopes of the biomass are cross-linked in that cotton stalk at a lower temperature shows a higher energy density than rice straw, while rice straw at a higher temperature has a higher energy density than cotton stalk. The torrefaction temperature of 250 ^{o}C can be the middle condition of the average energy yield and energy density of both biomass. Thus, the condition can be chosen depending on the intended use of the torrefied char. If a high energy yield is important, a temperature lower than 250 ^{o}C can be applied, especially with woody-type agricultural biomass cotton stalk. Conversely, a high temperature over 250 ^{o}C is better for obtaining densified bio-char which significantly increases heating value.

The highest energy yields of both biomass after torrefaction were obtained at the condition of 210 ^{o}C – 20 minutes. This indicates that the mass product yield of torrefied

char at the condition was recovered at 86% for RS and 90% for CS on a weight basis, while the energy recovered was almost 91% for RS and 99% for CS. In other words, the mass yield of condensable products has almost no energy value so that the energy value of torrefied char increases with a decrease in its weight. For instance, the torrefaction process of a metric ton of RS (17,130 MJ) and CS (16,900 MJ) can produce 870 kg for RS (17,458 MJ) and 910 kg for CS (17,290 MJ). The average densification value at 210 ^{o}C showed 1.09 for RS and 1.14 for CS, which indicates that a decrease in weight from the initial biomass of 9% for torrefied RS (910 kg) and 14% (860 kg) for torrefied CS (a metric ton) is needed to meet the same energy.

4.4. Conclusions

The torrefaction study was conducted with two different types of agricultural biomass, cotton stalk and rice straw, in a fixed-bed batch reactor using RSM. The different compositions of two agricultural biomass wastes (straw type and woody type) led to different results after the torrefaction process. A comprehensive analysis of torrefied char, liquid, and gas was conducted.

The biomass wastes processed at the highest temperature (290 ^{o}C) was converted into a comparable fuel source, which can be a substitute for brown coal and peat as the highest heating value was determined to be 28.6 MJ/kg through the torrefaction process. The increased heating value with a decrease in the weight of the biomass can be a good alternative source for gasification and combustion. The maximum solid energy densification for RS was 1.48, which is higher than that for CS at 1.37. This indicates

that the torrefied char at the highest temperature can reduce the weight of the original biomass to 52% for RS and 63% for CS and the energy recovery was over 70 – 80% of the solid energy yield. This can help alleviate the difficulties of storage and transportation.

5. PYROLYSIS OF RICE STRAW USING BENCH-SCALE AUGER, BATCH AND FLUIDIZED BED REACTORS*

5.1. Introduction

Pyrolysis technologies not only help control mass production of rice straw wastes, but they also assist in converting the wastes into valuable soil amendments and catalysts with a deoxidized bio-char. Also, the bio-oil and the gas generated during pyrolysis can be used in power generation. Thus, the comparison of energy conversion efficiencies of different pyrolysis technologies would be of great significance in making use of the rice straw for soil amendment and production of value added products.
The pyrolysis process using the abundant rice waste (rice husk and rice straw) has been done by many researchers. Pyrolysis of rice husk in a fixed bed reactor for a comparison of slow and fast pyrolysis was completed and the maximum bio-oil yield was achieved at 50.5 wt% at 500 ^{o}C [52]. The yield of bio-oil from rice straw pyrolysis increased from 30% to 40%, whereas the bio-char yield decreased from 58% to 40% in the lab-scale slow pyrolyzer, as the temperature rose from 300 to 700 ^{o}C [51].

In this study,

(1) The pyrolysis product yield and property from an auger type, a batch type, and a fluidized bed type reactor are compared.

---

* Reprinted with permission from "Experimental investigation of pyrolysis of rice straw using bench-scale auger, batch and fluidized bed type reactors" by H. Nam, S.C. Capareda, N. Ashwath and J. Kongkasawan, 2015. *Energy*, 93, 2384-2394, Copyright [2015] by Elsevier.

(2) Mass and energy recovery efficiencies are investigated and compared between the reactors.

5.2. Materials and Method

5.2.1. Sample characterization

Rice straw was obtained from Beaumont, Texas, and air-dried. A Wiley Laboratory mill (model #4) was used to mill the sample using 2 mm sieve. The methods described in Section 4.2.3 were used for the proximate analysis, high heating value (HVV) and elemental analysis.

5.2.2. Experimental facility

Pyrolysis experiments were conducted using an auger type, a batch type, and a fluidized bed (FB) type reactor as shown in Figure 5.1. The auger and batch type reactors will represent slow pyrolysis, and the fluidized bed type reactor represents fast pyrolysis, according to EIA bioenergy group report [175]. The auger type reactor can also be defined as intermediate pyrolysis as the residence time ranged between 20 and 25 minutes, which is an intermediate residence time between slow pyrolysis (over 4 hours) and fast pyrolysis (less than 1 second). All three reactors are regarded as bench-scale reactors, as the maximum processing rate of 100 g/min in auger reactor, 80 g/min in FB reactor, and the one time processing capacity of 300 g in batch reactor can be used.

An auger based reactor was used for slow or intermediate pyrolysis. A 3-zone cylindrical electric furnace (Linberg/Blue M from Thermoelectron Corporation, North

Carolina) was used to heat the main tube reactor of 10.2 cm diameter and 150 cm length with an auger flight connected to the feed hopper (61cm x 61cm x 130cm). Nitrogen gas of 10 L/min was passed into the reactor during the experiment to make sure that the produced gas was pushed into the exhaust pipe. One K-type thermocouple was placed inside the tube reactor to measure the actual reaction temperature, along with three thermocouples which were attached to the electric furnace. A bio-char bin was fitted at the end of the tube reactor. Two outlets were provided to collect volatile gas from the tube reactor. Glycol water at -4 ^{o}C was used to condense the bio-oil in an indirect heat exchange condenser. Then, a four-staged solvent condenser was placed to capture the remaining condensable volatile matter. The feed rate was set at about 10 g/min. The number of solvent condensers used were determined based on a preliminary experiment. The volumetric gas flow was measured with a gas meter (METRIS 250, Itron, Oweenton, KY) after calibration. Then, the sampled gas was analyzed using a gas chromatograph (GC) equipped with thermal conductivity detector (TCD).

A stainless steel batch type reactor (Series 4580 HP/HT, Parr Instrument Company, Moline, IL; Figure 5.1) was used for slow pyrolysis. The same set up was used in previous torrefaction study described in a previous chapter. A few different setups included a chiller using -4 ^{o}C glycol water was connected to an indirect heat exchange condenser and a two-staged solvent condensers connected to a chiller. The temperature was increased to the set temperature (500 ^{o}C) at the rate of 4 ^{o}C/min.

A fluidized bed reactor was used for fast pyrolysis, which was explained in a previous gasification chapter. A few different setups included a six-staged condenser for

bio-oil capture; the first canister was empty, whereas the others contained solvents (acetone).

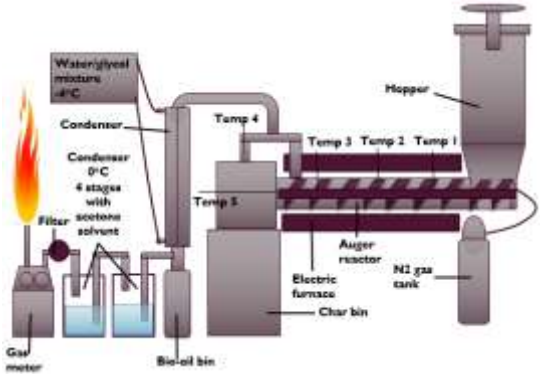

(a) Auger type

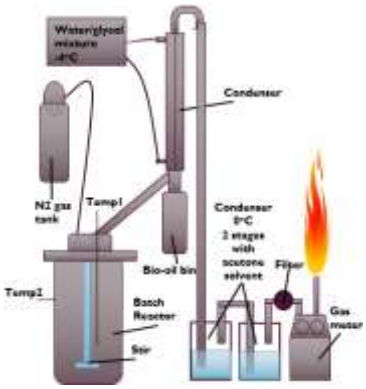

(b) Batch type

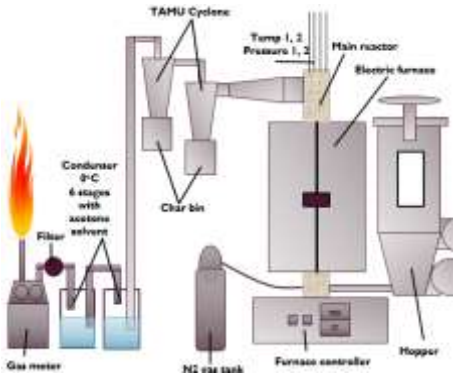

(c) Fluidized bed type

Figure 5.1. Schematic diagrams of the three pyrolysis reactors.

5.2.3. Analytical methods

The solid, liquid, and gas products from the rice straw pyrolysis experiment were analyzed using the following analytical methods. The equipment and standards for the product analysis are the same as described in a previous chapter 4. A high heating value, elemental analysis (C, H, N, and S), proximate analysis for (VCM, FC, and ash contents). ASTM E203 was used to measure water contents in bio-oil. The pH of the bio-oil was measured using a digital pH meter. GC-MS for relative chemical composition, GC-TCD for produced gas, Shimadzu IRAffinity-1 FTIR spectrophotometer were used to analyze the produced products. The mineral contents of samples were determined using ICP-OES of Spectro Blue, while the protein content was obtained from total nitrogen content which was determined by a high temperature combustion process.

5.2.4. Experimental design and data analysis

Three replications were used for each condition. The temperature was set at 500 ^{o}C in all the experiments, as the maximum bio-oil yield was obtained at this temperature [49,54,59,119,176]. The particle size of the rice straw was controlled by grinding the samples using a fixed sieve of 2 mm. The quantities of the feedstock used in each trial were about 250 g (batch reactor), 200 g (auger reactor) and 200 g fluidized bed reactor. Pyrolysis using the auger type reactor is regarded as a slow or intermediate pyrolysis which is set at the speed of 1.03 RPM, and corresponds to the 20 – 25 min reaction time from Equation (5.1). The nitrogen gas flow was maintained at 10 L/min. For the slow

pyrolysis, the reactor was heated at 4 ^{o}C/min until the set temperature (500 ^{o}C) and maintained for 30 minutes after nitrogen gas filled the reactor before each run. The residence time in the fluidized bed (FB) reactor was 1.6 seconds according to Equation (5.2) [148]. The inert gas flow rate of the fluidized bed reactor was set at 45 L/min.

Residence time of the auger (s) = Auger length (m)/ Biomass flow velocity (m/s) (5.1)

Residence time of the FB (s) = FB reactor volume (L)/Volumetric flow rate (L/s) (5.2)

Product mass and energy yields were obtained using Equations (5.3), (5.4), and (5.5). The yield balance was established after accounting for the losses. Mass yield was calculated on a weight basis whereas the energy yields of each of the solid, liquid, and gas product was calculated based on the amounts of energy converted from the initial biomass after pyrolysis.

$$\text{Product yield (\%)} = m_{product}/\ m_{initial} \quad (5.3)$$

$$\text{Bio-char yield (\%)} + \text{Liquid yield (\%)} + \text{Gas yield (\%)} + \text{Loss (\%)} = 100\% \quad (5.4)$$

$$\text{Energy yield (\%)} = (m_{product} \times HHV_{product})/(m_{initial} \times HHV_{initial}) \quad (5.5)$$

5.3. Results and Discussion

5.3.1. Rice straw characteristics

The proximate analysis showed the presence of a high proportion of volatile combustible matter (VCM) and ash, which contributed to about 69% and 22% of the rice

straw used, respectively as shown in Table 5.1. The fixed carbon (FC) contents showed only 9%. These results are similar to those reported previously (60 – 79% VCM, 4.6 - 16% FC, and 9.8 – 23% ash) [49,51,118,151,152,177]. The presence of a large proportion of ash led to relatively low heating value (14.2 MJ/kg) compared to the reports of other studies (15 – 16.2 MJ/kg). This also affected the carbon and hydrogen concentrations, which were as low as 36% C and 4.9% H. The H/C and O/C molar ratios of RS were revealed as 1.61 and 0.65, respectively. The chemical composition of rice straw is: $CH_{1.61}O_{0.66}N_{0.02}S_{0.002}$.

Table 5.1. Rice straw characteristics. (db: dry basis, [a]:[49,51,151,177,178])

Biomass characteristics	Rice straw	Literature[a]
High Heating Value (MJ/kg), db	14.2±0.2	15 – 16.2
Moisture (wt%)	9.2±0.1	8.9 – 14.1
Proximate analysis (wt%), db		
VCM	69.3±0.1	60 - 77
Fixed Carbon	9.01±0.96	4.6 – 16
Ash	21.7±1.1	9.8 – 23
Ultimate analysis (wt%), db		
C	36.6±0.2	40.8 – 54
H	4.9±0.15	5 – 7.6
N	0.77±0.02	0.4 – 3.9
S	0.23±0.02	0.5 – 0.56
O (by difference)		30 – 51.6

5.3.2. Yields of pyrolysis products

Pyrolysis experiments were conducted to evaluate the effects of different reactors on product yield and characteristics with rice straw. Product mass yields of bio-char,

liquid (bio-oil and aqueous phase) and the gas produced from an auger, a batch, and a fluidized bed reactor are shown in Figure 5.2. The mass product yield from the auger and batch pyrolysis systems exhibit similar trends of highest yield of bio-char (45 – 48%), followed by the liquid product (25 – 31%) and then by the lowest yield of gas (11 – 13%). On the other hand, the highest yield of the liquid portion (43%) was obtained from the fluidized bed pyrolysis, followed by the bio-char (27%) and gas (23%). The mass yields of bio-char and liquid in fluidized bed and other reactors showed a complete reversal of the above results mainly due to the use of different heating rates. The fluidizing medium caused a broad and abrasive contact with biomass at a faster rate, resulted in a high yield of liquid portion. More of the direct heating surface of the fluidized bed medium would have converted the biomass into more volatile matters. Furthermore, the volatile matters did not have enough time, energy or both to decompose into gases at 500 ^{o}C [59]. On the other hand, high yields of bio-char were obtained from the slow pyrolysis process of auger and batch type reactors due to slower heat transfer rates to the biomass. Similar results were observed from the slow and fast pyrolysis studies. A mass product yield from rice straw pyrolysis processed at 500 ^{o}C and 1.2 sec residence time produced 20% bio-char, and 36% liquid from a fluidized bed reactor [179]. A lab scale rice straw fast pyrolysis showed similar data at 23% bio-char, 50% bio-oil, and 27% gas at 520 ^{o}C [180]. In a slow pyrolysis process, about 40% bio-char, 38% bio-oil and 20% gas were obtained [51]. Thermogravimetric analysis (TGA) also showed 40% bio-char from rice straw pyrolysis [152]. The pyrolysis yields of corn stover in the same fixed bed reactors were reported at 32% for bio-char, 28% for liquid,

and 18% for gas. Also, the bio-char output yield from the auger pyrolyzer gained around 50% by weight of biomass input [148].

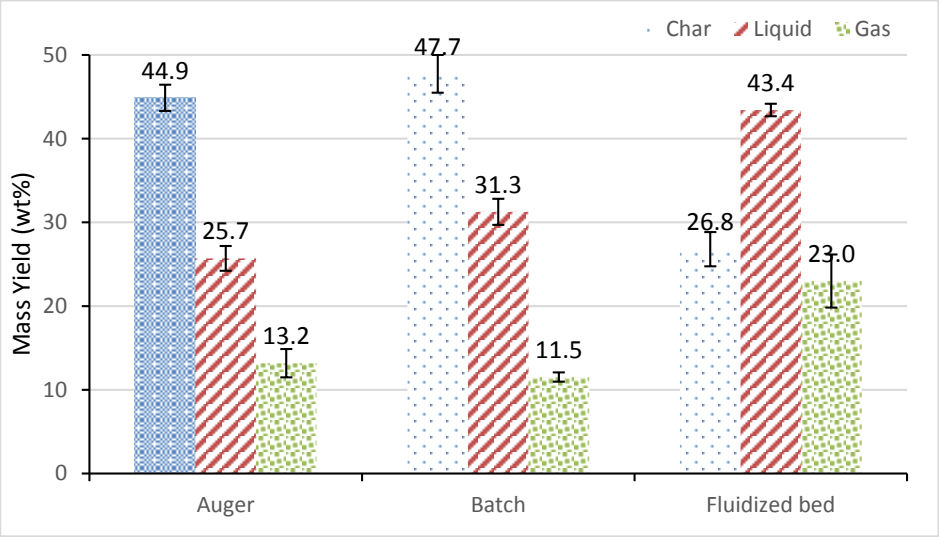

Figure 5.2. Bio-char, liquid and gas product yields from rice straw pyrolysis.

Mass conversion efficiencies of different process reactors were calculated based on Equation (5.4). The average loss from each reactor was 35% for the auger, 9% for the batch, and 12% for the fluidized bed reactor. Those losses were generated mostly from uncondensed liquid bio-oils that remained on the sides of the reactors and pipes as well as uncollected bio-char and the gas. The auger reactor had the highest loss as the quantity of the samples used was too small in such a large scale equipment. Despite the weaknesses, the experimental data show a clear trend and they will be useful when developing a large-scale pyrolyzer for commercial applications. The auger type reactor for slow/intermediate rate pyrolysis has some technical advantages; it is easy to operate

compared to fluidized bed reactor, and is also possesses faster production ability compared to a batch type reactor. Furthermore, the system can be automated, thus making it more user-friendly and cost effective.

5.3.3. Bio-oil properties

The liquid products from each reactor had different visual appearances. The bio-oil product from the FB reactor was homogenous and dark brown in color and produced a smoky odor. On the other hand, the liquid from the slow pyrolysis process of the auger and batch reactors separated into two layers of top organic portion (bio-oil) and a bottom aqueous portion (bio-liquor). The bio-oil composition contained alkanes, alkenes, alcohols, ketones, phenols, aromatics, and others in the top layer bio-oil from slow/intermediate pyrolysis and fast pyrolysis. The top layer bio-oil from the slow pyrolysis process was more viscous and darker brown color than the bio-oil from fast pyrolysis process. The slow pyrolysis bio-oil smelled strong and irritating. The bottom layer aqueous portion was watery (less viscous) and yellowish in color. The separated liquid phase from slow pyrolysis was also reported from other biomass wastes of lignocellulose biomass [181-184] and aquatic wastes [185]. The bio-oil from fast pyrolysis also showed unseparated liquid in different studies [183,186]. However, invisible separation was found after a month of storage, and bottom portion had a higher portion (55%) of water than the middle or the top portions (23%) of bio-oil [186].

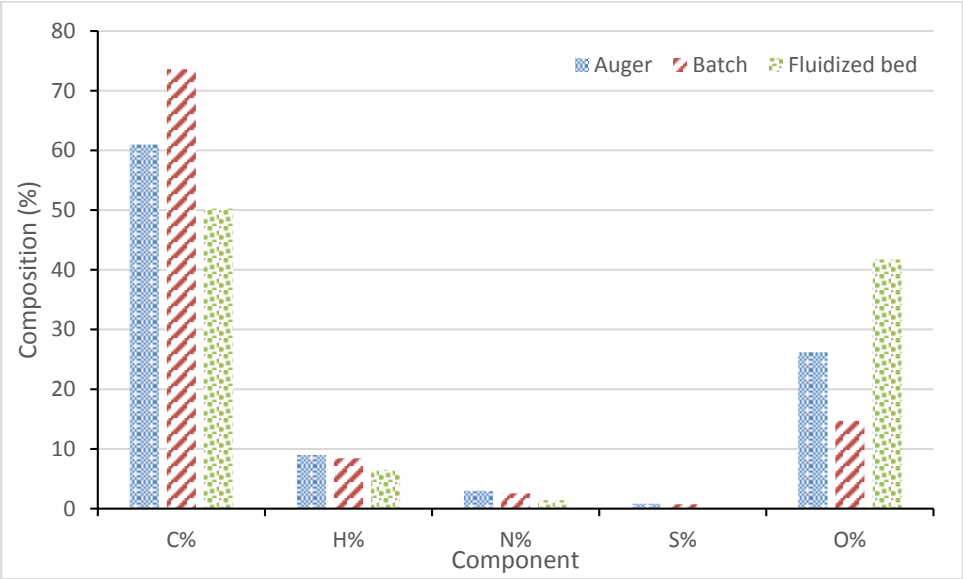

Figure 5.3. Ultimate analysis of bio-oil from different reactors.

Figure 5.3 shows the elemental compositions of pyrolytic bio-oils from three reactors. The highest carbon content (74%) of bio-oil was obtained from batch reactor, followed by auger reactor (61%), and fluidized bed reactor (50%). Conversely, the oxygen contents of bio-oil were 15% from the batch, 26% from the auger, and 42% from the FB reactor. The highest oxygen content was from the FB bio-oil which indicated the presence of oxygenated chemical compounds, as compared to the other two reactors. The trend in a higher oxygen content from the FB reactor to the fixed-bed (batch) type was also reported in a previous study [59]. Oxygen content of 21 - 28% was obtained from the fixed-bed reactor, whereas that of 30 - 48% was from the FB reactor. The presence of high oxygen content presents several weaknesses to the fuel; low heating value, unstable bio-oil, and immiscibility with other hydrocarbons [187]. The chemical formula for the three bio-oils are: $CH_{1.8}N_{0.04}O_{0.32}S_{0.005}$ (auger), $CH_{1.4}N_{0.03}O_{0.15}S_{0.004}$

(batch), and $CH_{1.6}N_{0.02}O_{0.62}S_{0.009}$ (FB). For a better understanding of the elemental composition of bio-oil, the Van Krevelen diagram was plotted as shown in Figure 5.4. This diagram includes the results from the current study as well as many other studies [49,51,119,183,185,188,189].

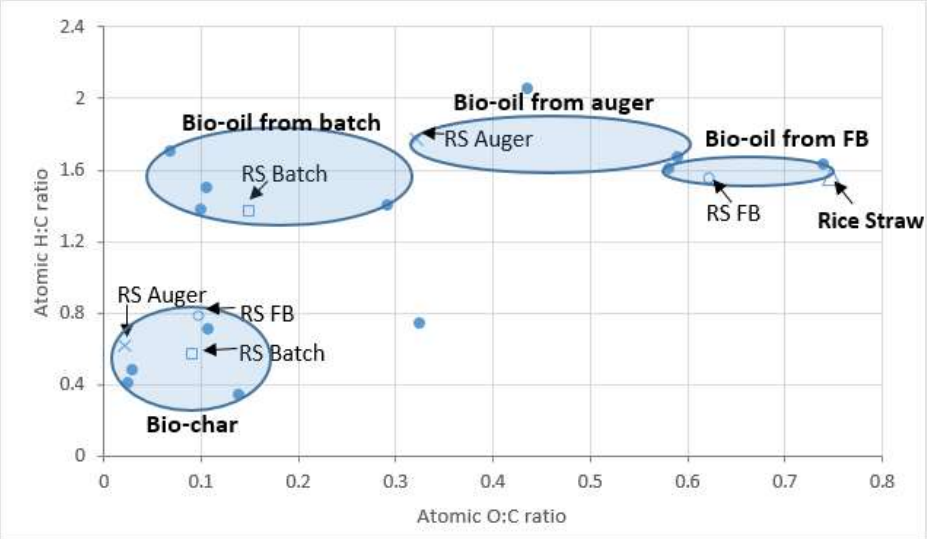

Figure 5.4. Van Krevelen diagram for the liquid and solid products from different pyrolyzers (Reference of biomasses; corn stover, sorghum, rice straw, switchgrass, algae, and corn cob [49,51,119,183,185,188,189]).

The O/C ratios (0.03 – 0.62) of rice straw bio-oil from different reactors varied to a greater extent than did the H/C ratios (1.37 – 1.77). The previous pyrolysis studies from different feedstocks and reactors showed similar trends with the current study for H/C and O/C ratios. The bio-oil from the FB reactor had higher O/C ratio (0.58 – 0.74) compared to those from the batch reactor (O/C ratio of 0.07- 0.29) and the auger reactor (O/C ratio of 0.32 – 0.59). The elemental ratio of the petroleum products are between 1.5

and 2.0 for H/C, and less than 0.06 for O/C [190]. The closest O/C ratio to a petroleum fuel was obtained from the batch reactor bio-oil (0.15). The results show that the pyrolysis oil needs further processing before it can substitute a petroleum oil. However, the mixing of bio-oil with petroleum products can be used without upgrading.

Table 5.2. Physicochemical properties of the pyrolysis bio-oil.

	Auger	Batch	FB	ASTM standard D7544	
HHV(MJ/kg)	29.4±2.6	30.7±2.1	20.6±2.2	15min.	ASTM D2015
Ash (wt.%)	<0.2	<0.2	1.0±0.1	0.25max.	ASTM D482
pH	5.3±0.3	3.1±0.0	2.6±0.1	Report	pH meter
MC (wt.%)	14.3±0.8	10.2±0.3	5.7±0.4	30max.	ASTM E203

Table 5.2 shows physicochemical characteristics of bio-oils. The high heating value (HHV) of bio-oil was found at 29 MJ/kg from the batch reactor, 31 MJ/kg from the auger reactor, and 21 MJ/kg from the FB reactor. These value were all above the ASTM standard of 15 MJ/kg. A high ash content of the fuels can contribute to wear of pumps, valves, and reactors by fouling and slagging. The ash content obtained from this study was less than 0.2 wt% from the slow/intermediate pyrolysis process, whereas 1.0 wt% in the FB bio-oil. The ash content of the bio-oil from an FB reactor can vary depending on the feedstock size and the reaction temperature [183]. The smaller the feedstock size and the lower the reaction temperature, the lesser will be the ash content was produced. A higher pH value from the auger pyrolysis bio-oil was determined at 5.3, which was higher than the bio-oils from the batch and the FB reactors. The bio-oil pH

value which ranged between 2 and 4.5 was found from bagasse in a batch reactor, and from energy sorghum in an FB reactor [183,191]. As the low acidity is corrosive to metals, the low acidity should be treated before it is used in an engine. Moisture contents of bio-oils were determined at 14% from the auger, 10% from the batch, and 6% from the FB reactor. The amount of moisture present in the bio-oil affects the overall viscosity, the heat of combustion, and the flame temperature when used in the engines.

The relative chemical composition of bio-oil was determined using GCMS, and the results are shown in Table 5.3. More than 100 chemical compounds were detected in FB bio-oil, but a fewer number of chemical compounds were found in the bio-oils of auger and batch reactors. The compounds were categorized by chemical groups of phenols, alkanes, alkenes, alcohols, ketones, aromatics, nitriles, and others. The largest relative chemical from all three reactors was the phenol group at 28 – 35%. The 2-methoxyphenol is one of the main chemical compounds produced from the lignin portion of the biomass. More oxygenated compounds contributed to a higher phenolic content [178]. The phenol compounds were also found to be a major components of lignocellulose biomass [59,119,183]. Many oxygenated compounds of aromatics and ketones were produced mainly from cellulose and hemicellulose [192]. As the rice straw feedstock has high portion of glucan and xylan from the main components of cellulose and hemicellulose, respectively, a large percentage of the oxygenated chemicals were inevitably found in the derived bio-oils. Additionally, almost 20% of aliphatic compounds of alkanes and alkenes were obtained in the bio-oils of slow pyrolysis

process whereas the bio-oil from the fast pyrolysis had only traces of aliphatic chemicals.

Table 5.3. Chemical composition of bio-oil determined by GC-MS.

Auger	Batch	FB
Compound (Relative %)	Compound (Relative %)	Compound (Relative %)
Alkanes (13.75)	**Alkanes (11.33)**	**Acids (4.27)**
Tridecane	Nonane	Acetic acid, methyl ester
Dodecane	Decane	Butanoic acid
Tridecane, 4,8-dimethyl-	Tridecane	Propanoic acid, 2-oxo-, methyl ester
Hexadecane	Dodecane, 2,6,11-trimethyl-	
		Alkenes (0.5)
Alkenes (8.88)	**Alkenes (10.18)**	3-Hexene
1-Dodecene	1-Decene, 4-methyl-	1-Butene, 3-methyl-3-(1-ethoxyethoxy)
3-Tetradecene, (Z)-	1-Dodecene	
1,4-Methanonaphthalene, 1,4-dihydro-	3-Tetradecene, (Z)-	**Alcohols (6.91)**
1-Tetradecene	2-Hexadecene, 2,6,10,14-tetramethyl-	2-Furanmethanol
1-Hexadecene	1-Tetradecene	1,4-Butanediol, 2,3-bis(methylene)-
1-Docosene		1,3-Propanediol, 2-(hydroxymethyl)-2-
	Alcohols (3.89)	1,3-Propanediol, 2-ethyl-2
Alcohols (4.83)	1,2-Ethanediol, diacetate	
Nonanol, 4,8-dimethyl-	2-Furanmethanol, tetrahydro-	**Ketones (17.72)**
2-Furanmethanol, tetrahydro-		1-Hydroxy-2-butanone
	Ketones (19.03)	2-Pentanone, 4-hydroxy-4-methyl-
Ketones (12.04)	2-Pentanone, 3-methyl-	4-Nonanone, 7-ethyl-
2-Cyclopenten-1-one, 2-methyl-	Cyclopentanone	Cyclohexanone
2-Cyclopenten-1-one, 3-methyl-	Cyclopentanone, 2-methyl-	2-Cyclopenten-1-one, 3-methyl-
2-Cyclopenten-1-one, 2,3-dimethyl-	Cyclopentanone, 3-methyl-	2-Furanone, 2,5-dihydro-3,5-dimethyl
Acetophenone	2-Cyclopenten-1-one, 2-methyl-	2-Cyclopenten-1-one, 3-ethyl-2-hydroxy
	2-Cyclopenten-1-one, 2,3-dimethyl-	
	Cyclopentanone, 2-ethyl-	

Table 5.3. Continued.

Auger	Batch	FB
Compound (Relative %)	Compound (Relative %)	Compound (Relative %)
Phenols (35.27)	**Phenols (27.72)**	**Phenols (33.04)**
Phenol	Phenol	Phenol
Phenol, 2-methyl-	Phenol, 2-methyl-	Phenol, 2-methyl-
Phenol, 3-methyl-	Phenol, 3-methyl-	Phenol, 3-methyl-
Phenol, 2-methoxy-	Phenol, 2-methoxy-	Phenol, 2-methoxy-
Phenol, 4-ethyl-	Phenol, 2-methoxy-4-methyl-	Phenol, 4-ethyl-
Phenol, 2,3-dimethyl-	Phenol, 2,4-dimethyl-	Phenol, 4-ethyl-2-methoxy-
Phenol, 2-ethyl-5-methyl-	Phenol, 4-ethyl-	Phenol, 2,6-dimethoxy-
		Phenol, 2-methoxy
Aromatics (20.25)	**Aromatics (25.27)**	Phenol, 2,6-dimethoxy-4
Ethylbenzene	Ethylbenzene	Vanillin
Benzene, 1,2,3-trimethyl-	p-Xylene	1,2-Benzenediol
1H-Indene, 1-chloro-2,3-dihydro-	Benzene, 1,3-dimethyl-	1,2-Benzenediol, 4-methyl-
Benzene, 2-ethenyl-1,4-dimethyl-	Benzene, 1,2,4-trimethyl-	2-Methoxy-4-vinylphenol
Benzene, 1-ethyl-2-methyl-	Benzene, 2-ethenyl-1,4-dimethyl-	Hydroquinone
	Benzene, 1-ethyl-2-methyl-	
Nitriles (4.43)	Toluene	**Aromatics (2.01)**
Benzonitrile	Indene	1,2,4-Trimethoxybenzene
	1,4-Methanonaphthalene, 1,4-dihydro-	1,3-Benzenediol, 2-methyl-
	Naphthalene	
		Others (29.31)
	Nitriles (1.56)	Furfural
	Butanenitrile, 3-methyl-	Benzofuran, 2,3-dihydro-
	Pentanenitrile	D-Allose
		Butanedial
		Hexanedial
		3-Acetoxybenzaldehyde

The FTIR spectra was used to understand the absorption of the functional groups of the bio-oil and aqueous product as shown in Figure 5.5. The FTIR functional groups at each peak are referenced from other studies [119,185,193]. The peak ranged between 3600 and 3200 cm^{-1} which indicates that the O-H stretching vibrations show the presence of water, phenol, and alcohol, which was the dominant peak of the aqueous product from both the auger and batch pyrolysis processors due to the presence of large quantity of water. The C-H bending vibration at 3200-2800 cm^{-1} and 1475-1350 cm^{-1} indicate the presence of alkanes in the bio-oils from both processes (2941, 1455, and 1380 cm^{-1}). The aliphatic acids that include ketones, aldehydes and carboxylic acids were detected in both the aqueous products and the bio-oils as the C=O vibration peaks from 1750 to 1650 cm^{-1}. A higher peak at 1654 cm^{-1} was observed in the aqueous product as compared to the bio-oil mainly by the wide spectrum bands of ketones, whereas a higher peak at 1710-1696 cm^{-1} was obtained in the bio-oil indicating the presence of aldehydes and carboxylic acid [194-196]. The C=C bending vibration peaks between 1650 and 1580 cm^{-1}, corresponding to the presence of alkenes and aromatic compounds were observed in both auger and batch type bio-oils (1600 cm^{-1}) as well as in the aqueous product (1640 cm^{-1}). The broad peak ranges of 1150-980 cm^{-1} (the C-O stretch of polysaccharides) [168], and 1215-1220 cm^{-1} (a strong vibration of C-C, C-O and C=O stretches) [169] were detected in the bio-oil, while no or small peaks in the ranges exist in the aqueous component. Polycyclic aromatics were found in the bio-oil (825 and 752 cm^{-1}) as the peaks between 900 and 675 cm^{-1}. This indicated the presence of polycyclic and substituted aromatic rings.

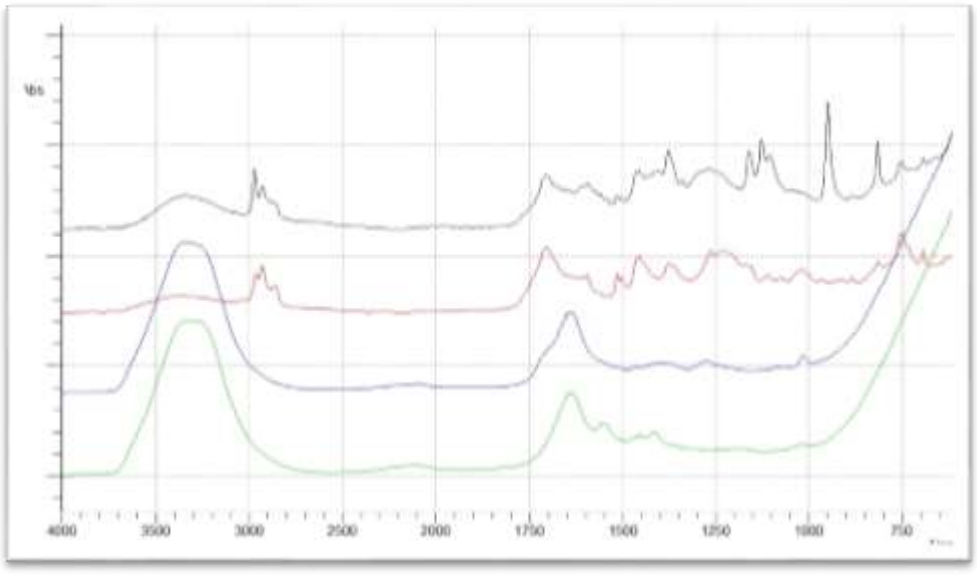

Figure 5.5. FTIR of slow pyrolytic liquid fractions (from top; bio-oil from auger and batch, and aqueous portion from auger and batch).

5.3.4. Bio-char properties

Bio-char samples were collected from the three process reactors. Proximate analysis of the bio-char from all reactors indicated the presence of the highest amount of ash content among others of the volatile combustible matter (VCM) and fixed carbon (FC) (Figure 5.6; p-value 0.0185). It was reported that lignin was the main component of FC in the bio-char, which does not easily decompose at 500 ^{o}C [197]. As the pyrolysis temperature was set at 500 ^{o}C, a large portion of the VCM was reduced from 69% to 20 – 27% due to the removal of most of the cellulose and all of the hemicellulose. The FC from a batch reactor showed relatively higher amounts than other reactors (p-value 0.0023). This could be due to the pyrolysis reactions occurring statically in batch reactor, in comparison with that in a FB reactor where the reactions occur in the moving bed in

N_2 flow. The conversion rate of lignin (FC) from the same materials can vary depending on the different process types. The heating value (HV) of the FB bio-char was 13 MJ/kg, whereas that from an auger and batch reactors was 16 (auger) and 19 (batch) MJ/kg. The higher heating value of the bio-char from the batch reactor as compared to the FB reactor can be explained by the sum of the VCM and FC contents.

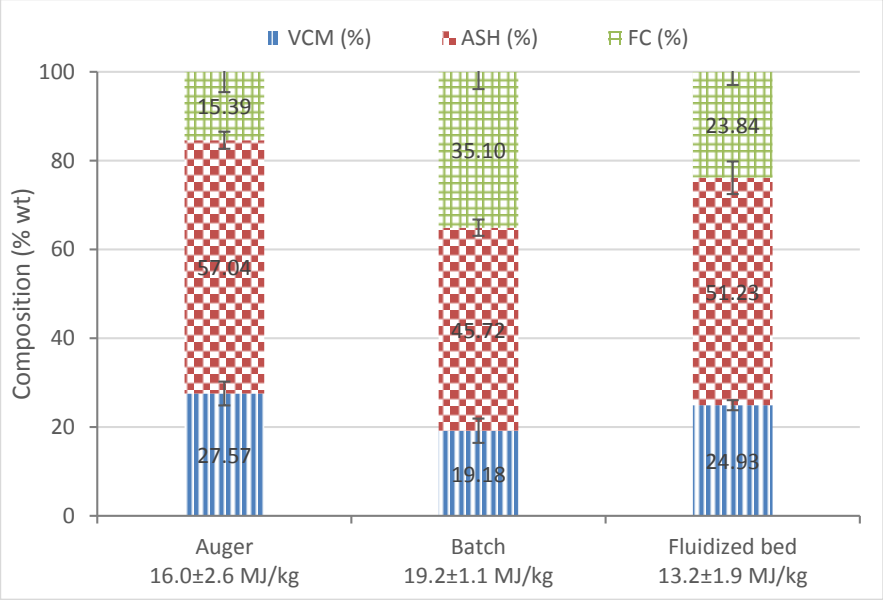

Figure 5.6. Proximate data and high heating value for the bio-char products (dry basis).

The elemental compositions of bio-chars of different reactors were also determined. The carbon content was found to be between 38% and 45%, which was higher than that of rice straw (37%). As shown in the Van Krevelen plot in Figure 5.4, the H/C (0.56 – 0.78) and O/C (0.02 – 0.1) ranges of rice straw bio-char did not vary much in spite of the use of different reactors. Also, the different feedstock (corn stover,

sorghum, switchgrass, algae, and corn cob) showed similar H/C (0.36 – 0.78) and O/C (0.03 – 0.32) ranges in the bio-chars. Thus, regardless of the type of feedstock and process reactors used, similar ratios of H/C and O/C were produced during the pyrolysis at around 500 ^{o}C as indicated in Figure 5.7. However, the different operating temperatures from 200 to 300 ^{o}C lead to different ratios of H/C (0.89 – 1.65) and O/C (0.21 – 0.87) of rice straw and cotton stalk samples according to Nam and Capareda [118]. The highest bio-char carbon content was obtained from the batch pyrolysis, whereas the lowest was recorded from the auger bio-char. The protein contents of the bio-chars from the auger and batch reactors are (8.3%), which verified the amount of nitrogen at 1.5% in bio-char from both reactors. The protein content of 2% from the FB reactor supported the nitrogen content of 0.49%.

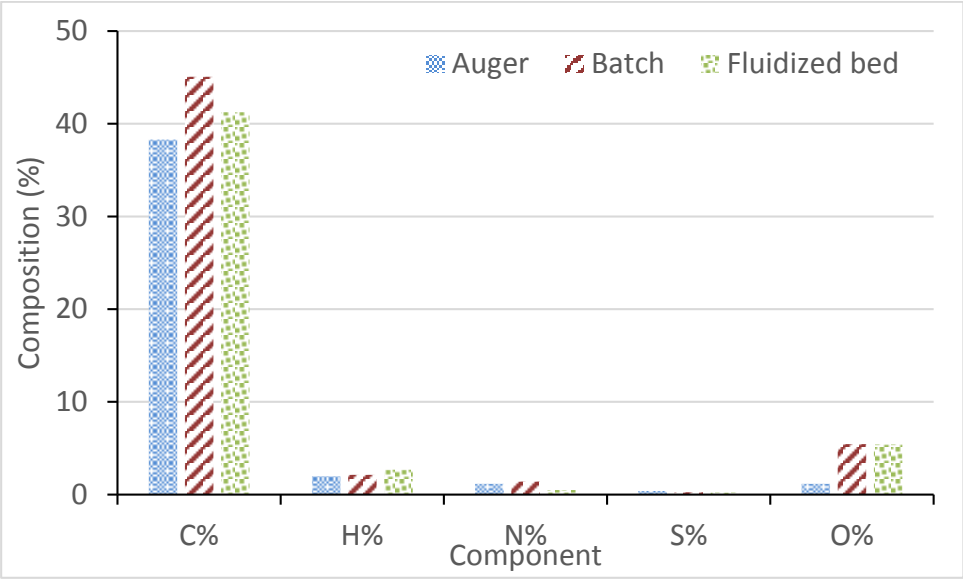

Figure 5.7. Ultimate data of bio-char from the rice straw pyrolysis (dry basis).

5.3.5. Gas composition

Combustible gas products were obtained from different reactors after pyrolysis as shown in Figure 5.8. The composition of combustible gases were H_2, CO, CH_4, C_2H_2, C_2H_4, C_2H_6, C_3H_6, and C_3H_8. Since an N_2 carrier gas was used in the auger and fluidized bed, high N_2 gas composition was obtained in the product gas, which would have led to a low gas heating value of 7 (auger) and 0.4 (FB) MJ/m^3. On the other hand, the gas from the FB reactor contained a large portion of non-combustible gas of about 95%. A high H_2 production from the auger pyrolyzer was noticeable among three reactors. Higher composition of H_2 gas can be obtained at the increased temperatures from the auger based reactor [198]. After calibrating the gas compositionsd by removing the O_2 and N_2 gases, the gas heating values from all reactors were increased to around 10 MJ/kg. Large amounts of CO and CO_2 gas production from pyrolysis process was produced by the cracking and reforming of functional carboxyl groups [185].

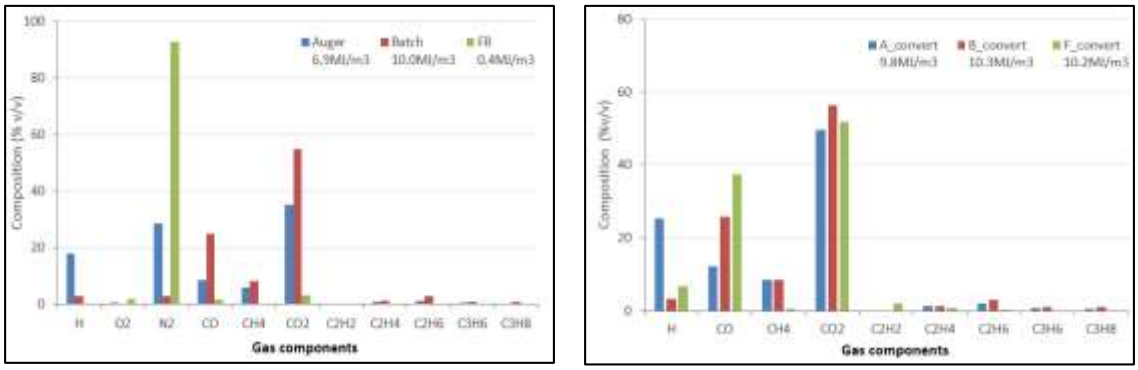

(a) (b)

Figure 5.8. Composition of gas product from the rice pyrolysis (a) as received (b) after removing O_2 and N_2 gases.

5.3.6. Energy balance

Figure 5.9 shows the energy recovery distribution of pyrolysis products from different reactors at 500 ^{o}C. It can be observed that the recovery of the energy yields were similar for batch and auger pyrolyzers. More than half of the initial energy was recovered by bio-char, and 10 – 15% of the energy was derived from volatile products (bio-oil and gas) in slow pyrolysis reactors. The low energy recovery of the volatile products is the result of the low quantities of bio-oil and non-combustible CO_2 gas. In contrast, the energy recovery from an FB bio-oil reached 47%, which was due to large mass production with moderate bio-oil heating value. On an average, the total energy recovered from these processes achieved ranged from 65% for the auger pyrolyzer to 75% for the batch pyrolyzer. Since the auger reactor was large, the energy loss was higher with the same amount of initial samples than with the other pyrolyzers. Otherwise, the product energy efficiency of the auger reactor was 81% [198]. Other researchers also reported energy loss as much as 25% and 18% during the pyrolysis process caused by reactor heat loss and energy lost from condensers [188,199]. The Sankey diagram helps in understanding how energy is transferred from raw biomass wastes to other types of products (bio-char, bio-oil, and bio-gas) as shown in Figure 5.10. The process rate of biomass input was set at 1 kg/hour for three reactors, which corresponds to 12.9 MJ/hour. From the diagram, the energy of gas production from all types of reactors was close to 1 MJ/hour. Large amounts of energy were contained in the solid products that were obtained from auger and batch reactors, while a major energy product from the FB reactor was bio-oil.

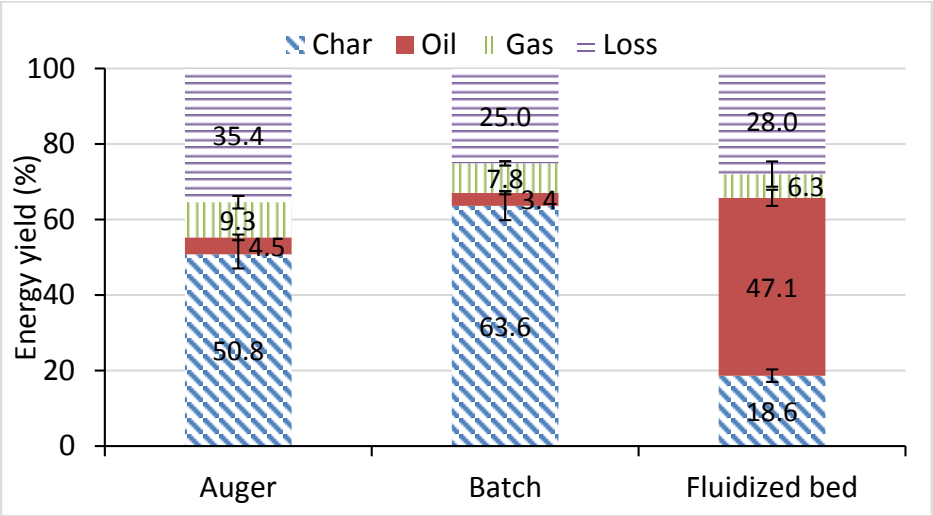

Figure 5.9. Energy recoveries of pyrolysis process from different reactors

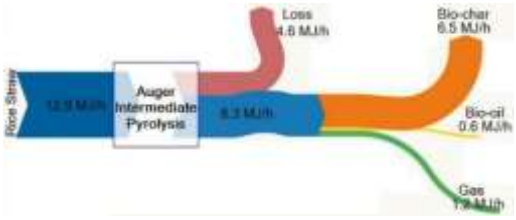

(a) Auger type reactor

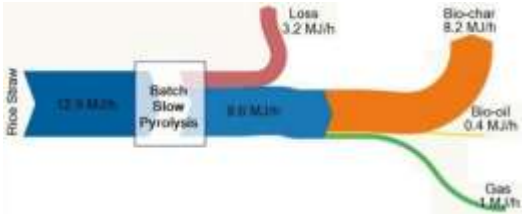

(b) Batch type reactor

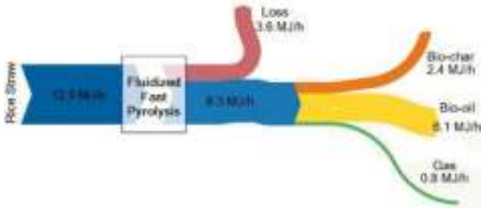

(c) Fluidized bed type reactor

Figure 5.10. Sankey diagram for bio-char, bio-oil, and bio-gas product distribution via various pyrolysis reactors.

5.4. Conclusion

Three reactors (an auger type, a batch type, and a fluidized bed type) were utilized for the pyrolysis study. The temperature condition was set at 500^{o}C with 2 mm milled rice straw. The slow process of the auger and batch type reactors resulted in higher yields of bio-char, while the fast process of the fluidized bed reactor produced a larger quantity of bio-oil. The fast heat transfer rate due to the fluidizing medium led to a high mass yield of bio-oil. The higher heating value (HHV) of bio-oils from the auger and batch type reactors showed a relatively higher HHV than the fluidized bed reactor. The bio-oil from all reactors had a majority of phenolic compounds, and more aliphatic compounds were detected from the slow pyrolysis reactors. The bio-oil elemental composition ratio (O/C) showed different ranges depending on the type of reactor used, while the H/C ratio remained similar among the three reactors. On the other hand, both the O/C and H/C ratios of bio-chars were similar among three different reactors were obtained in similar ranges. In summary, a batch and an auger reactor can be recommended for bio-char production, whereas a fluidized bed reactor is optimal for bio-oil production even though the best bio-oil quality can be obtained from a batch reactor.

6. COMPARISON OF PRODUCT DISTRIBUTIONS FROM VARIOUS PROCESSING AND WASTES AND ECONOMIC EVALUATION OF DAIRY MANURE GASIFICATION

6.1. Introduction

Representative thermochemical conversion processes of gasification (Chapter 3), torrefaction (Chapter 4), and pyrolysis (Chapter 5) were investigated using various biomass wastes and reactors. The variables of temperature, reactor, waste type, and the amount oxygen present gave different mass and energy yields. The main products from the thermochemical conversion included bio-oil, bio-char, and gas. The main application of bio-oil and the liquid phase can be biofuel substitutes and specialty chemicals depending on the biomass type. Bio-char has more applicable usages as catalyst, electrode material, activated carbon, adsorption material, and a soil enhancer. The produced gas from pyrolysis and gasification also has applications in the production of electricity through an engine generator and a heat power generator, and chemical production through catalytic reactions (e.g. Fisher Tropsch). A comparison of the product yields and product properties from different processes and wastes were conducted for a better understanding of the uses. Also, an economic evaluation was done on a dairy manure gasification because the study was done in a pilot scale reactor, and the major product (syngas) does not require a further downstream process to be used as a fuel source.

In this study,

1) the product yields of bio-char, bio-oil, and gas produced from different conditions are compared and discussed,
2) the properties of bio-char, bio-oil and gas products are compared and discussed, and
3) the economic evaluation of dairy manure gasification is studied.

6.2. Experimental

6.2.1. Biomass feedstock

Various biomass were utilized for the thermal conversion process of pyrolysis and gasification as follows. Most pyrolysis and gasification data were imported from previous chapters, and some pyrolysis results using corn stover and sorghum were imported from other studies [119,183].

Pyrolysis: AJ (Ashe Juniper), Ag (microalgae), BLT (beauty leaf tree fruit seed), CS (cotton stalk), CrS* (corn stover), DM (dairy manure), RS (rice straw), and Sg* (sorghum). *imported work from other studies [119,183].

Gasification: DM (dairy manure), RS (rice straw), Slg (sewage sludge), and WC (woodchip).

6.2.2. Thermochemical processes and experimental conditions for comparison

Auger, batch, and fluidized bed type reactors were used for the pyrolysis experiments, while only the batch type was used for the torrefaction process as introduced in previous chapters (Chapter 4 and Chapter 5). The temperature conditions

used with the batch reactor were 250, 290 and 500 ºC for a 30 min residence time, while an auger reactor was used at 500 ºC for a 15 – 20 min residence time. The residence time for a fluidized bed reactor was about 1.6 sec at 500 ºC.

The gasification results reported in this chapter were from a bench-scale fluidized bed reactor, introduced and shown in Chapter 3. The oxidant agent was air and an air-oxygen mixture. The operating conditions used for comparison were temperatures from 600 to 800 ºC, while the ER ranged between 0.15 and 0.4. Some gasification ER conditions for runs were not reported as they were done in a preliminary test. Table 6.1 shows conditions used for the pyrolysis and gasification process.

Table 6.1. Operating conditions of pyrolysis and gasification processes

	Pyrolysis			Gasification
	Auger	Batch	Fluidized	Fluidized
Feed Size (mm)	< 2	< 2	< 2	< 2
Reaction type	Intermediate	Slow	Fast	Fast
Heating Rate (ºC/min)	30 - 500	4 - 5	> 10,000	> 10,000
Vapor residence time	15 - 20 min	120 min	1.6 sec	1.6 sec
Reaction Temperature (ºC)	500	250 - 500	500	700 - 800

6.2.3. Economic assumptions

An economic evaluation for gasification power generation was done with the data from this study and economic guides [200-205]. The annual fixed capital investment (FCI) and variable costs for operation and maintenance were assumed based on the pilot-scale TAMU mobile gasification system. The price of a 3-ft diameter

fluidized bed gasifier is $321,736 and the initial fixed capital investment (FCI) was estimated by modifying the reported data [201,204] as shown in Table 6.2. The prices of other equipment were imported from the pilot-scale mobile pyrolysis unit with some modifications [204]. The assumptions for the economic analysis of the mobile plant were as follows: (i) the plant has no salvage value [200], (ii) plant life was estimated to be 15 years [200], (iii) the annual variable operating costs of labor and maintenance were assumed to be 20% and 5% of the FCI, respectively [202], (iv) The capacity exponent of 0.7, based on the sixth-tenths-factor rule, was used to calculate the price of scaling up the gasifier using Equation (6.1) as the capital cost does not vary linearly with plant capacity [202,206,207].

Fixed capital investment (FCI),

$$FCI_B = FCI_A \left(\frac{Capacity_B}{Capacity_A}\right)^X \quad (6.1)$$

where, X = capacity exponent (0.7)

(v) the annual tax rate was set at 35%, (vi) the mass yield and price of bio-char were assumed to be 5% and 0.1 $/kg, respectively [203,204], (vii) the dry solid manure production from each head of dairy cattle was obtained as 8.2 kg/day-animal dry matter [127], (viii) the operation period for the plant process of daily production of dairy manure was set at 365 days, (ix) the high heating value (HHV) of processed sand mixed dairy manure was obtained as 12.3 MJ/kg, (x) The overall efficiency of electricity generation from feedstock to power generation was set as 15% [201], (xi) no land cost

was assumed as the estimate is based on mobile facilities, (xii) a MARCS (modified accelerated cost recovery system) was used to calculate the discounted cash flow return on investment (DCF ROI), the discounted payback period (DPBP), and production selling cost, (xiii) a 7-year depreciation schedule was applied to the MARCS with a 10% IRR (internal rate of return), and (xiv) no state tax was applied as the model dairy area is located in Texas.

Table 6.2. Fixed capital investment costs of a 3-foot mobile gasifier designed for use with 2000 dairy cows [27,30].

Fixed Capital Investment		
$	321,736	3-foot diameter gasifier
$	18,000	Cost to and from the site for delivery
$	2,500	Cost to dismantle and assemble the slab each time
$	62,500	1 used tractor to pull trailers
$	4,500	40 ton capacity box trailer
$	2,000	Flatbed trailer for feedstock
$	139,250	Trailer mounted feedstock dryer
$	22,333	Equipment/tool storage
$	10,000	Blower
$	15,000	Sand separator and blower
$	30,000	In loader 3 yard
$	30,000	Power generator
$	5,000	Other
$	662,819	TOTAL

6.3. Results and Discussion

6.3.1. Comparison of pyrolysis yield and product properties

The mass recovery from various waste thermochemical conversions through different reactors were balanced. An auger, batch, and fluidized bed reactors were used for pyrolysis at 500 ^{o}C. A batch reactor was utilized for the torrefaction process at 250 ^{o}C and 290 ^{o}C. Figure 6.1 shows the mass recovery of a solid bio-char, a liquid bio-oil and aqueous phase, and gas products. Two other pyrolysis studies of corn stover [119] and sorghum [183] were also referenced for comparison purposes. As a lower temperature was used in the torrefaction process, the mass yields of bio-char ranged from 68% to 71%, which were higher yields than the bio-char from pyrolysis at the constant temperature of 500 ^{o}C ranging from 23% to 63%. A higher product mass yield of microalgae bio-char than other wastes through an auger reactor was caused by not enough residence time for the wastes to be fully volatilized and its larger amount of ash content. The production of bio-char from batch and auger reactors showed a similar amount regardless of the biomass types. On the other hand, the oil crop of BLT (beauty leaf tree) seed cake (48%), sludge pellet (54%) and corn stover (32%) produced a high mass yield of bio-oil even in a slow pyrolysis, which was comparable to the mass yields from fast fluidized bed pyrolysis (32 – 42%).

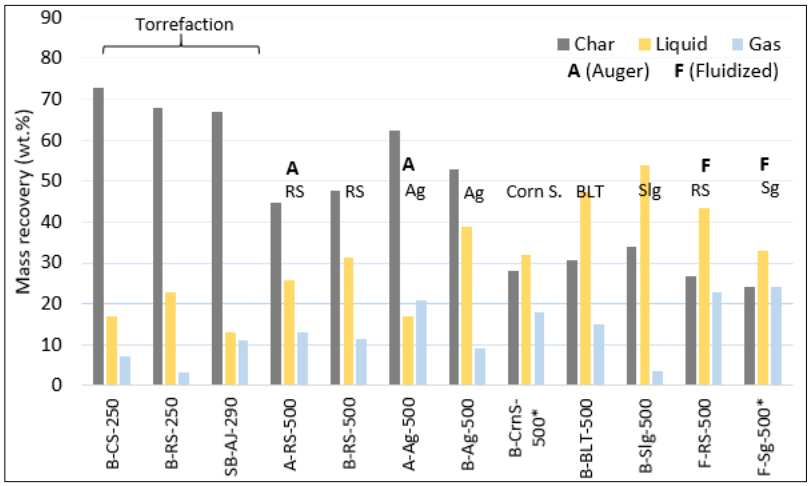

Figure 6.1. Mass recovery of bio-char, bio-oil and gas from various pyrolysis experiments.

Figure 6.2 shows the energy recovery of products produced from torrefaction and pyrolysis through various reactors. Some process products showed a similar distribution of mass and energy yields, while others did not. The energy from torrefied bio-char products recovered over 80%, while no energy was recovered in bio-oil and gas products as they included mostly water in bio-oil and non-combustible gases in gas products. In contrast, a high yield of bio-oil was obtained from a lignocellulosic fluidized bed pyrolysis (44 – 48%) and a microalgae slow pyrolysis (50%), which was a much larger amount of bio-oil than other feedstock (5 – 18%). It can be concluded that a slow pyrolysis is not recommended for producing bio-oil if considering only energy recovery. However, the HHV of bio-oil produced from a slow pyrolysis showed a much higher value than that produced from fast pyrolysis as shown in Figure 6.3. As was discussed in Chapter 4, a higher HHV for rice straw bio-oil was obtained from a slow and intermediate pyrolysis (29 – 31 MJ/kg) compared to a fast pyrolysis of 20 MJ/kg.

Another classification of biomass can be based on the protein content as wastes including a large amount of protein such as microalgae, BLT cake and sludge pellet showed a relatively higher HHV of bio-oil (over 34 MJ/kg) compared to other lignocellulosic wastes (29 – 32 MJ/kg). The HHV of torrefied bio-char ranged from 21 to 24 MJ/kg, while most of the pyrolytic bio-char showed from 7 to 19 MJ/kg except for that of corn stover (23 MJ/kg) and BLT de-oiled cake (28 MJ/kg). A high HHV for bio-char can be inferred from the existence of a high VCM content and oil. The highest HHV of bio-char obtained from the current study was 29 MJ/kg for rice straw torrefaction at the condition of 290 ºC and 60 min.

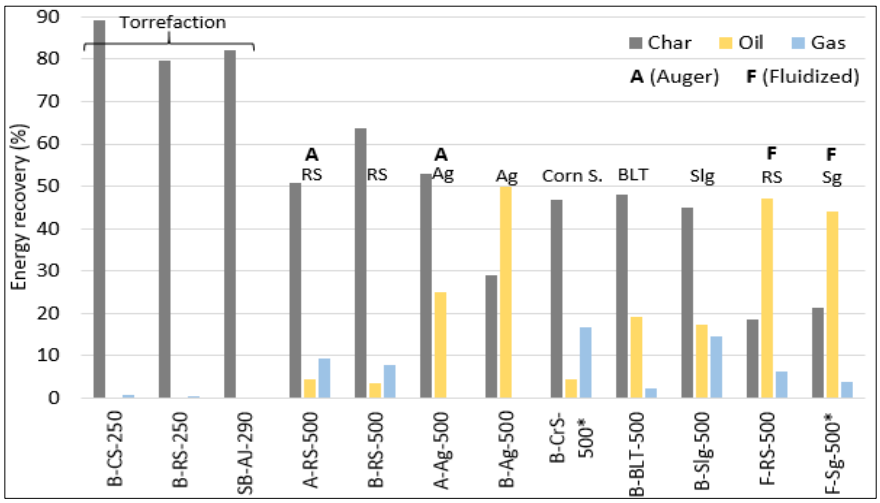

Figure 6.2. Energy recovery of bio-char, bio-oil and gas from various pyrolysis experiments.

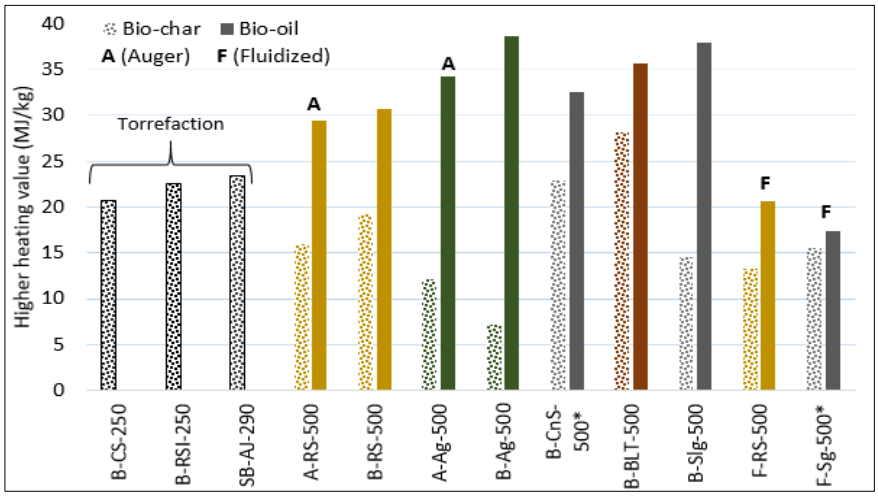

Figure 6.3. Higher heating value of bio-char and bio-oil from different reactors, biomass and temperatures.

Figure 6.4 shows a Van Krevelen diagram that helps in understanding the elemental compositions of bio-char and bio-oil products. As discussed in Chapter 5, the O/C and H/C ratios of bio-oil and bio-char products were gathered in at designated ratios. The high oxygen content in a bio-oil produced from a fluidized bed reactor caused a higher O/C ratio (0.6 – 0.9), while the bio-oil from a batch and an auger reactor showed O/C ratios of 0.1 – 0.15 and 0.22 – 0.33, respectively. However, the H/C of bio-oil produced from different reactors showed more or less similar ranges between 1.4 and 1.8, which is close to the H/C ratio of petro fuel (1.65 – 2.0). The bio-oil with the lowest H/C ratio (1.0) was produced from BLT de-oiled cake in a batch reactor as the hydrogen content (6.1%) was the least compared to other bio-oils, while the most nitrogen content (8.8%) and the second most sulfur content (1.6%) were found from BLT cake bio-oil. The highest sulfur content was from sludge pellet pyrolytic bio-oil (2.4%). The different trends in O/C contents from different reactors can be explained by the amount of oxygen

in the bio-oil of 11 – 15% from a batch, 20 – 26% from an auger, and 41 – 50% from a fluidized bed reactor. As the dotted lines of dehydration and decarboxylation show, the bio-oil elemental property from a fluidized bed to a batch reactor can be expected to produce CO_2 and CO gas through decarboxylation (loss of carboxyl groups, -COOH) and H_2O through dehydration reactions (loss of hydroxyl groups, -OH). The decarboxylation reaction is preferred so that the bio-oil is close to the petro fuels.

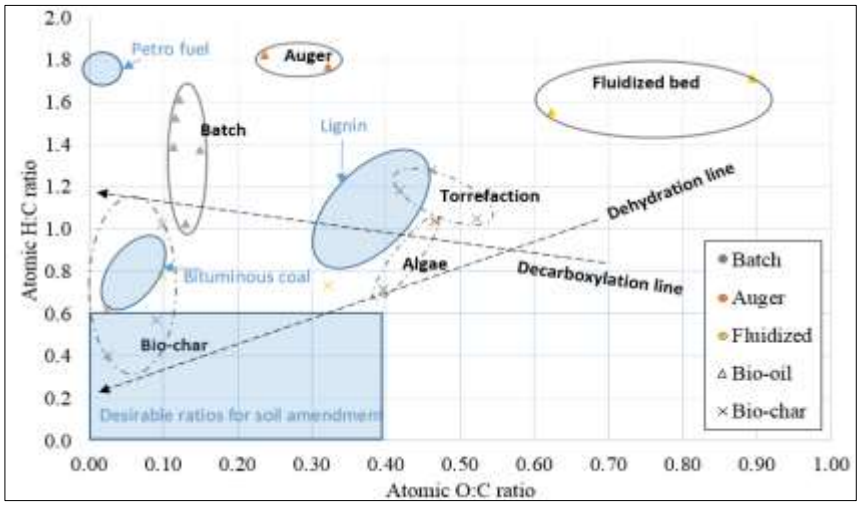

Figure 6.4. Van Krevelen diagram for the various feedstocks and its pyrolysis (or torrefaction) solid and liquid products.

The ratio ranges of solid product were separated depending on the temperature or feedstocks. The initial ratios of lignocellulosic biomass wastes locates in 1.4 – 1.62 of H/C and 0.6 – 0.75 of O/C, whereas *N. Oculata* microalgae located at around 1.9 of H/C and 0.36 of O/C. The high O/C and H/C of organic materials (lignin, cellulose, brown coal like torrefied bio-char, and pyrolyzed algae char as indicated in Figure 6.4 are more

degradable than the less O/C and H/C ratios of bio-char as the higher amount of oxygen and hydrogen leads to more chemical reactivity against stability of bio-char in soils. Most of the pyrolytic bio-chars were represented in the range of 0.4 – 1.0 of H/C and 0.02 – 0.1 of O/C, similar to bituminous coal ranges. Some were located in a range of desirable ratios for soil amendment. The square box was imported from Schimmelpfennig et al. [64] in that the high C content was caused by the substantial amount of aromatic C with low functional groups, and they suggested that the carbon contents close to 100% can be classified as hardly degradable in the environment. The bio-char defined from Kuhlbusch and Cruten [208] had an H/C ratio less than 0.2, which should be recalcitrant to degradation in soils due to C sequestration. The utilization of bio-char in soil was positively proved because of its characteristics of nutrient retention, water-holding capacity, and microbial growth, which helped product yields and growths [209,210].

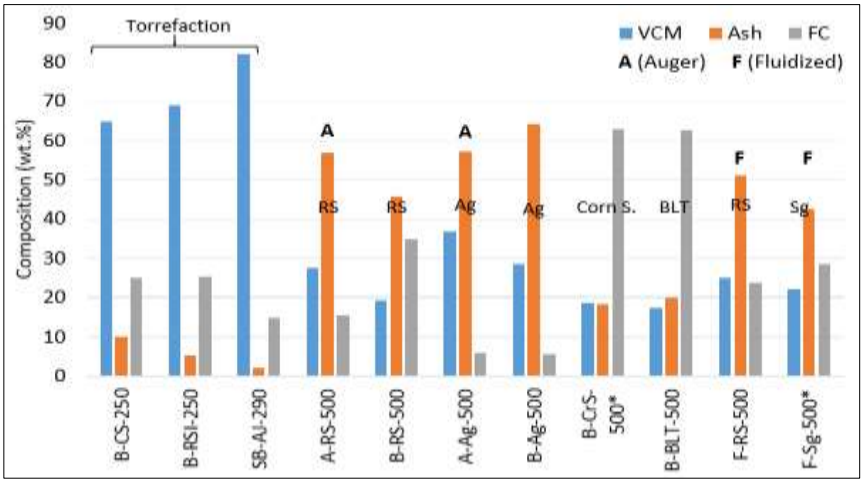

Figure 6.5. Proximate analysis of bio-chars from various samples, reactors and reaction temperatures.

The proximate analysis of the torrefaction pyrolysis solid products are compared in Figure 6.5. As a lower temperature was used in torrefaction, more VCM (volatile combustible matter) ranging from 65 to 82% were obtained at the operating temperature from 250 to 290 ^{o}C. Because of the discrepancy in weight loss of hemicellulose, cellulose, and lignin contents, the solid yield and VCM content at different temperatures and biomass types resulted accordingly. However, at a higher temperature of 500 ^{o}C, the highest amount of ash content was found at 42 – 65% from most biomass wastes. Only the wastes of corn stover and BLT cake obtained the most fixed carbon at about 64%.

6.3.2. Comparison of gasification and pyrolysis syngas

The gases produced from gasification and pyrolysis was flared and injected into a 10 kW gasoline engine as presented in Figure 6.6. The pyrolysis gas from batch and auger reactors was able to be flared, while the pyrolysis gas from a fluidized bed reactor wouldn't catch fire due to the almost 90% nitrogen gas that was used as a fluidizing agent. All the gasification experiments were conducted using a bench scale fluidized bed reactor. The engine operation tests were conducted using a sludge pellet and gas from dairy manure gasification. Both successfully started a 10 kW engine even though the engine didn't produce enough for a power out, which indicated there was not enough fuel for the full operation of an engine. The dairy manure syngas with an LHV of 3.8 MJ/Nm^3 didn't at first initiate the engine with the 1/8 inch gas intake pipe which was worked with a sludge pellet producing syngas of 7.7 – 10.6 MJ/Nm^3 for engine

operation. After replacing the gas intake pipe with one measuring ¼ inch, the syngas from the dairy manure gasification also successfully started the engine.

(a) **(b)**

Figure 6.6. Pictures of (a) flared sludge pellet pyrolysis gas and (b) the engine operation with the sludge pellet gasified syngas.

Figure 6.7 indicates the gas compositions and their LHV produced from the gasification and pyrolysis processes. All the gasification gas was produced with a fluidized bed reactor, while the pyrolysis gas was from batch, auger, and fluidized bed reactors. The biomass used for the gasification were woodchip, dairy manure, sludge pellet, and a mixture of dairy manure and sludge pellet. The air gasification with woodchip showed a higher LHV (5.4 – 8.2 MJ/Nm^3) compared to the LHV (3.8 – 5.7 MJ/Nm^3) of dairy manure at operating temperatures from 700 to 800 ^{o}C. For upgrading the LHV of dairy manure, a mixture of sludge pellet and dairy manure gasification was conducted and showed increasing LHVs with an increasing amount of sludge pellet. When additional oxygen was applied, the LHVs were increased to 8.0 MJ/Nm^3 with

dairy manure and 10.6 MJ/Nm^3 with sludge pellets, which was comparable to the pyrolysis sludge pellet gas of 11.7% from an auger reactor at 676 ^oC. A slow pyrolysis gas of rice straw at 500 ^oC showed relatively high LHVs (10 MJ/Nm^3) than other air gasification LHVs as they produced higher hydrocarbon gases. In contrast, the gas from a fluidized bed showed 0.4 MJ/Nm^3 of LHV due to a larger amount of nitrogen gas that was used as a fluidized agent. The trends of produced gas LHVs followed the amount of combustible gases of H_2, CO, CH_4 and other hydrocarbon gases. Air gasification obtained CO_2 gas at around 18 – 21% regardless of the temperature and biomass wastes at an ER ranging from 0.2 to 0.3. The CO_2 gas showed higher with oxygen gasification due to more combustion reactions. The reason for much higher CO_2 gas (35 – 55%) from pyrolysis was not just because of the combustion reactions, but because of significant decarboxylation and decarbonylation reactions.

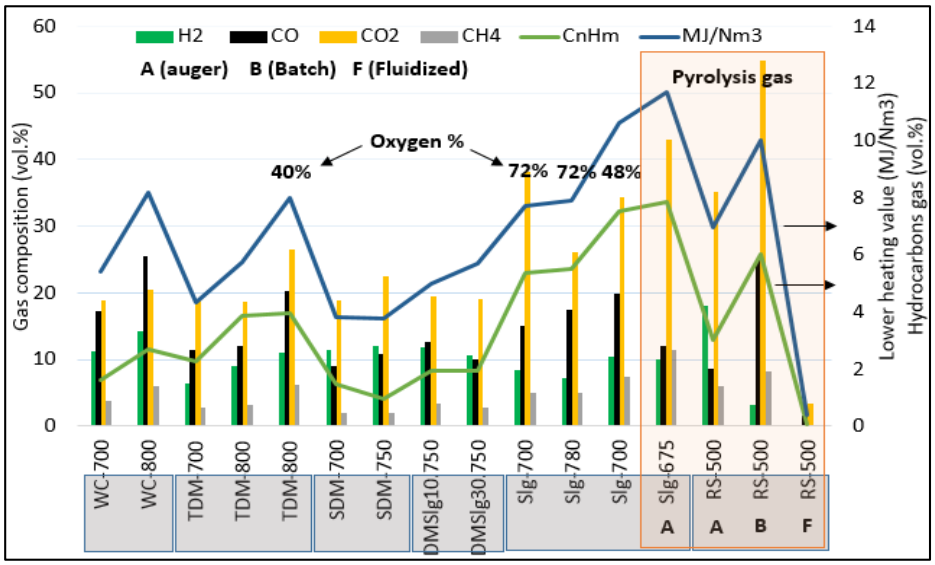

Figure 6.7. Produced gas compositions from gasification and pyrolysis processes (1 MJ/m^3 = 26.8 Btu/ft^3).

6.3.3. Economic analysis of dairy manure gasification

A total of four dairy farms in the Panhandle of Texas were considered in this study. The number of dairy cows on the four farms was estimated to be 14,500 [201]. The FCI was obtained as $662,819, and the annual variable operating costs were determined to be $165,704. Capareda et al. [201] reported that a 3 ft. gasifier can handle the manure of about 2000 head of cattle per day. The capacity exponent factor of 0.7 was used to calculate the price of scaling up the gasifier to meet the number of head on the four dairy farms in the Panhandle region. As the FCI increased with the scaled-up facility, the annual labor costs and annual operating costs also increased accordingly, as shown in Table 6.3. The potential possible power generation was determined to be 2.5 MW for the four dairy farms with a gasification process and engine generation efficiency of 15%.

Table 6.3. The scaled-up costs of FCI and annual variable costs [6,27,30].

Region	Total Head	FCI	Labor	Operation	Power(MW)
Standard	2,000	$662,819	$132,564	$33,141	0.4
Panhandle	14,500	$2,652,354	$530,471	$132,618	2.5

Since the average retail price of electricity for residential use was found to be 0.1264 $/kWh in 2015 [205], the range of electricity selling prices for the sensitivity analysis was cheaper than the retail price. The power production costs from the four dairies were determined to be 0.053 $/kWh. A further sensitivity analysis based on the electricity selling price ranging from 0.06 to 0.125 $/kWh of generated electricity was

performed to understand the discounted cash flow return of investment (DCF ROI) and the discounted payback period (DPBP). The four indicators from the economic analysis approve it as a recommended project. 1) The project can make $6.96 MM of net profit in today's currency after all the initial installation expenditures are paid off, with a 10% annual deterioration of the currency value. 2) The DCF ROI above 17% at the minimum selling price of 0.08 $/kWh exceeds the assumed IRR (internal return rate) of 10% as shown in Figure 6.8. 3) The DPBP ranges from 3.7 to 5 years. 4) The gasification technology and the raw materials have a limited risk since the manure is produced on a daily basis. Other important possible factors which can add profit to the project are the waste disposal charges and the use of on-site electricity, which can also improve the ROI and PBP. It was reported that the average electricity use of a dairy farm in the Panhandle of Texas is about 285 kWh/year/head (0.47 MW) [128]. The electric power of 2.5 MW from the pilot mobile gasification system can cover the electric power requirements of 1.89 MW of the four dairy farms in the Panhandle area.

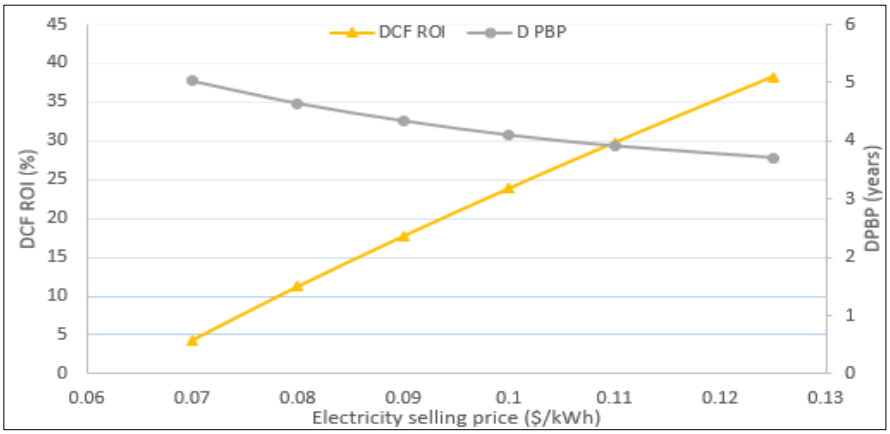

Figure 6.8. Sensitivity analysis of the electricity selling price on DCF ROI and DPBP.

6.4. Conclusions

The product yields and product properties from different reactors, biomass types, and processes were compared and discussed. A much higher yield of bio-char was obtained from torrefaction than pyrolysis and the gasification process as a lower temperature was applied. Also, a slow pyrolysis (auger and batch reactors) compared to fast pyrolysis (fluidized bed reactor) produced relatively higher amounts of bio-char products from most of the wastes except for corn stover, BLT cake, and sludge pellet. However, energy yields from some wastes showed a different trend from mass yield (algae, corn stover, and sludge pellet). This was because of the different energy densifications of bio-oil and bio-char products as well as the different proximate compositions of bio-char. Fast pyrolysis always produced the largest amount of bio-oil and its energy. All the bio-oil products from pyrolysis represented the highest HHV among the products. Also, the gas composition was compared and it was concluded that the lesser the oxygen amount used for reactions, the higher the LHV gas produced. Other conditions of temperature and biomass type affected the energy and mass yields of the gas as well. Finally, the gasification process was selected for an economic analysis. The syngas production price was determined to be at 0.053 $/kWh, which is economically viable.

7. UTILIZATION OF PYROLYSIS PRODUCTS: ACTIVATED BIO-CHAR CARBON FOR CAPACITANCE, ADSORBENT AND BIO-OIL UPGRADING[*]

7.1. Introduction

Waste management, pollution management, and energy production are three important fields to be explored and put into practice as the world population increases, especially in an industrialized countries. Unrecycled (or unrecyclable) wastes must be responsibly disposed to prevent environmental issues. Most solid wastes can be converted into bio-char and bio-oil through thermal conversion processes. The potential applications of char has been investigated and it can be used for combustible energy material, a soil amendment, and activated carbon. The value of activated carbon can vary based on how the carbon is used, such as for metal catalyst support, a gas or liquid purification media, or an electrode material for energy storage.

The chemical activation using a KOH solution is known as the most effective method for activating the bio-char as a higher pore sizes can be achieved compared to a physical activation method. Based on many studies, analytical techniques using BET, isotherms, XRD, EDX, SEM, and ultimate analysis were used, depending on the application of the activated carbon. The adsorption material, as activated carbon, was applied for the removal of various pollutants such as metals, dyes, phenolic compounds,

---

[*] Part of the data reported in this chapter is reprinted with permission from "Comparative study of vacuum and fractional distillation using pyrolytic microalgae (*Nannochloropsis oculata*) bio-oil" by H. Nam, J. Choi and S.C. Capareda, 2016. *Algal Research*, accepted on April 2016, Copyright [2016] by Elsevier.

and pharmaceuticals. Acetaminophen and ibuprofen are the major consumable medicines all over the world, and they are partly soluble in water and in organic solvents. Also, the use of activated carbon as a supercapacitor is well defined and commercially available, for example, from Matsushita Electric Industrial (Japan) and Pinnacle Research (USA). The advantages of a higher energy density than capacitors and a higher power density than batteries with long life cycles due to the absence of chemical reactions has gained the attention of many industries. The last application introduced in this chapter is a catalyst for bio-oil upgrading. The high porosity of the activated carbon makes it easy for it to hold various metal catalysts. The trial with cheap and effective nickel, applied in the hydrotreament process, compared to the expensive palladium prevalently used in oil and gas industries is one example of a practical use for activated carbon.

In this study,

1. The effect of temperature on chemical activation of rice straw (RS) bio-char was investigated to obtain an activated carbon with the highest surface area and micropores.
2. The effectiveness of produced activated carbon as water pollutant adsorption and supercapacitance material was evaluated.
3. The nickel supported on activated carbon (Ni/AC) was used to upgrade vacuum distilled microalgae bio-oil for fuel substitutes or additives.

7.2. Experimental

7.2.1. Materials

Bio-char (BC) for activated carbon synthesis was obtained from the thermochemical pyrolysis process with rice straw obtained from Beaumont, Texas. The temperature used was 500 ^{o}C for a 30 min residence time using a batch type reactor discussed as Chapter 5. Commercial activated carbon of mesh 20 – 40, nickel nitrate hexahydrate ($Ni(NO_3)_2*_6H_2O$) and commercial 5% Pd/C were purchased from Sigma Aldrich, and they were used for a comparison. The developed activated carbon from the bio-char and commercial activated carbon are abbreviated as AC and C, respectively (eg. RSAC750: rice straw activated carbon at 750 ^{o}C, Ni/AC: nickel on activated carbon, and Ni/C: nickel on commercially purchased activated carbon).

Microalgae pyrolytic bio-oil was produced to find the effectiveness of the metal supported on the activated carbon on the hydrotreatment. A batch type pyrolysis reactor was utilized at 500 ^{o}C for a 30 minute residence time. The produced pyrolytic bio-oil was then fractionated into the distillate fractions 1, 2, and 3 using a vacuum distillation setup as shown in Figure 7.1 (a). The temperature of the heating medium and vacuum pressure were, respectively, set at 120 ^{o}C and 90 Pa.

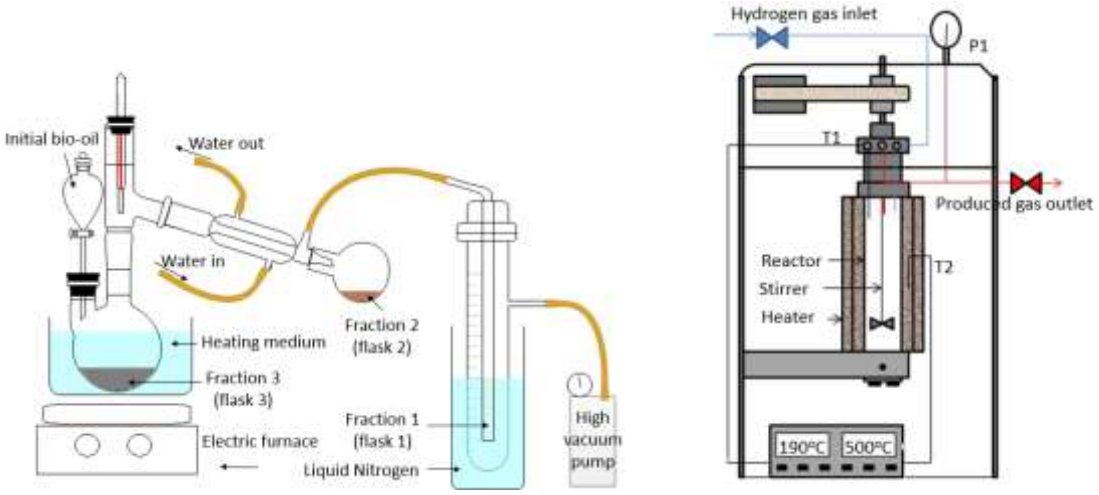

Vacuum distillation setup (b) Catalytic pressure reactor [185]

Figure 7.1. Experimental set-up used for distillation and catalytic upgrading.

7.2.2. Activated carbon (AC) and nickel supported catalyst synthesis

The BC was chemically activated using a KOH solution. The char sieved with US Mesh 20 and 40 pans was impregnated in 3 and 8 M KOH solutions for 3 hours at room temperature with magnetic stirring at 600 rpm. The sample was oven dried at 105 ^{o}C overnight. The oven dried sample was then activated at temperatures of 550, 650, 750 and 850 ^{o}C for 30 mins under a nitrogen flow of 0.5 L/min. The AC was washed with deionized water before a 0.1 mol HCl solution was used for an hour-long acidic treatment to remove impurities. The deionized water was again used to wash the AC until the pH was close to 7.0. The neutralized AC was then finally dried in a 105 ^{o}C oven overnight.

The prepared AC and C (commercial activated carbon) supports were impregnated in a solution of 0.05 g $Ni(NO_3)_2$/mL for 12 hours at a 600 stirring rpm and

40 ^{o}C. The amount of solution was determined based on the weight of the AC and C to make a 10% Ni loading on the activated carbon. The impregnated catalysts were then dried in a 105 ^{o}C oven overnight. The catalysts were identified as Ni/AC (10 wt.% Ni supported on the prepared activated carbon) and Ni/C (10 wt.% Ni supported on the commercial activated carbon). The EDX (Energy dispersive X-ray) equipped with a SEM (Scanning electron microscope) and XRD (X-ray diffraction) was used to observe the presence of nickel on the activated carbon.

7.2.3. Cell construction and electrochemical measurements

The produced activated carbon from Ashe Juniper wastes and rice straw were used for electrochemical tests. Also, a commercially available activated carbon (Sigma Aldrich) was used for comparison. The capacitance samples were prepared as ink to evaluate their electrocatalytic activities. A mixture of 7 mg of RSAC750 and 160 µL of 5 wt.% Nafion solution (Fuel Cell Earth) was distributed in a DI water (500 µL) and ethanol (170 µL) solution. Then the prepared inks were well dispersed using a sonicator (FB-120, Fisher Scientific) for more than 1 hour, and was loaded on a glassy carbon electrode of BASi. The ink on the electrode was oven dried at 40 ^{o}C for the cyclic voltammetry (CV) experiment. CV tests were carried out with a three-electrode system using a 604D CHI electrochemical station in a 0.5 M H_2SO_4 electrolyte. The three electrodes were composed of a working electrode of the AC sample, a Pt wire as a counter electrode, and an Ag/AgCl electrode in saturated KCl as a reference electrode. Nitrogen was continuously purged to the electrolyte. For a comparison purpose, a

commercial activated carbon and Ash Junipers activated carbon were also prepared for electrochemical measurements.

7.2.4. Experimental procedure of acetaminophen and ibuprofen adsorption

Acetaminophen and ibuprofen solutions of 10 mg/L were initially prepared using analytical grade ethanol solution and pharmaceutical powers of acetaminophen and ibuprofen. As the RSAC750 sample showed the highest surface area, this carbon was selected as an adsorbent and 0.05 g of AC was added into the 100 ml of pharmaceutical solution after adjusting the pH value to 4.0 using a 1.0 M H_2SO_4 solution. The adsorbance characteristics were determined using a UV-vis (Shimadzu), and the calibration curve was constructed using an initial concentration from 2 to 10 mg/L for both the solutions of acetaminophen and ibuprofen. The 10 mg/L concentrate of both solutions with the activated carbon were agitated for 24 hours before the last scans to understand the final concentration of chemicals.

7.2.5. Experimental setup and procedure of bio-oil upgrading

A batch type pressure reactor, shown in Figure 7.1 (b) was utilized to upgrade the pyrolytic bio-oil and distilled oil. Each run was made with 7 g of bio-oil with a 5 wt.% of prepared catalyst. Hydrogen gas was used to flush the air from inside the reactor as much as possible. Then the reactor was pressurized with 4.1 MPa of hydrogen gas at room temperature. Once the experiment was ready to run, the heater jacket heated the reactor to 190 ^oC for 3 hours and the oil was stirred at 400 rpm. After the reaction time,

the reactor was quenched to room temperature with the help of a water jacket. Gas samples were first obtained for analysis before the pressure was released. Finally, the upgraded bio-oil was collected after filtering with a Ni supported on an AC catalyst using a pre-weighted class filter. Then the remaining catalyst and bio-oil in the reactor was washed out thoroughly using acetone. Both the class filter and washed bio-oil were then dried in a 60 ^{o}C oven to completely remove the acetone solvent. The weight of the dried catalyst and dried washed bio-oil were identified as coke and tar, respectively, for mass balance analysis.

7.2.6. Analytical methods

The size characterization of activated carbon was analyzed using a Quantachrome Instrument (autosorb-iQ model). First, the samples were degassed for 3 hours at 300 ^{o}C. The adsorption and desorption isotherms were also measured from the different relative pressures (0.0 – 1.0) of N_2 adsorption under a -196 ^{o}C chamber. A specific surface area (m^2/g), pore volume (m^3/g), and pore size distribution were determined based on a carbon equilibrium slit-pore model (NLDFT, non-local density functional theory). XRD (X-ray diffraction) patterns using a Bruker-AXS D8 VARIO were examined to understand the inorganic compounds. The Cu Kα radiation was set from 2Θ = 20 to 60^{o} with a step size of 0.007^{o}. The AC and nickel impregnated AC morphology were obtained by a Hittachi S-2400 SEM (Scanning electron microscope) and the elemental analysis was scanned using an EDS of energy dispersive x-ray spectroscopy (Kevex Ltd., Sigma). The EDS of the used catalyst was also done to

understand any changes in the elemental compositions. The chemical percent was obtained as an average percent of 5 – 6 scans from a 1 × 1 mm window.

The pyrolytic bio-oil, distillated bio-oil, and upgraded bio-oil were analyzed using the following analytical methods. A Vario MICRO Elemental analyzer was utilized for determining carbon, hydrogen, nitrogen, and sulfur contents in accordance with ASTM D5373. The oxygen content was determined by difference assuming there was no ash inclusion in the bio-oils. The HHV (higher heating value) was obtained using a Parr bomb calorimeter (ASTM D711). The ASTM E203 based a Karl-Fisher Titration setup was used to find the moisture content. A color titration indication method of ASTM D974 was used to find the TAN (total acid number). A GCMS (Shimadzu QP2010Plus) equipped with a 30 m × 0.25 mm × 0.25 µm thick was used to determine the chemical compositions of the bio-oils. The same temperature programs used in a previous pyrolysis chapter (Chapter 5) were set.

7.3. Results and Discussion

7.3.1. Characteristics of the activated carbon and catalyst

The N_2 adsorption-desorption isotherms of the RSACs and Ni/AC samples at -196 ^{o}C was done as shown in Figure 7.2 (a). According to the IUPAC guidelines and a reference [65], all the RSACs showed a combination of Type I (b) and Type II isotherms with Type H4 hysteresis (slit-shaped pores). Type 1 (b) indicates the existence of wide micropores different from the narrow micropores of Type 1 (a), which can be understood from the round knee at a relative pressure (P/P_o) below 0.15 where the formation of

monolayer finishes and the formation of multilayer begins. The narrow hysteresis loop present in all samples also indicates the presence of mesopores in the result of inter-particle capillary condensation [65]. The capillary condensation caused the steeper slope with RSAC 650 ^{o}C compared to others showing the existence of more mesopores above 35 Å width as found in Figure 7.2 (b).

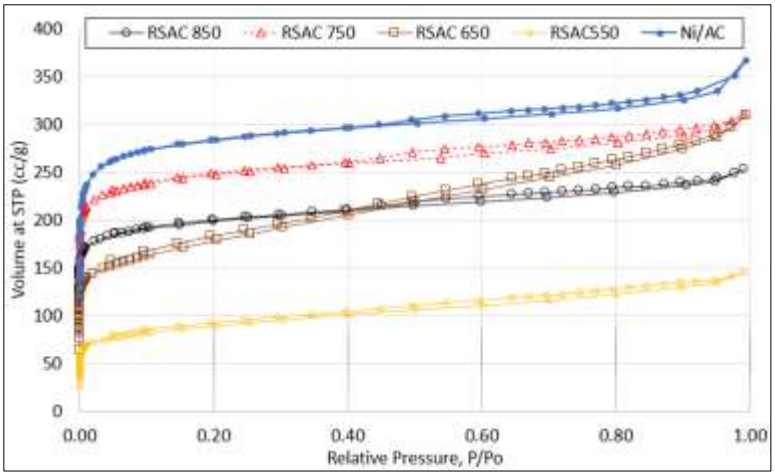

(a)

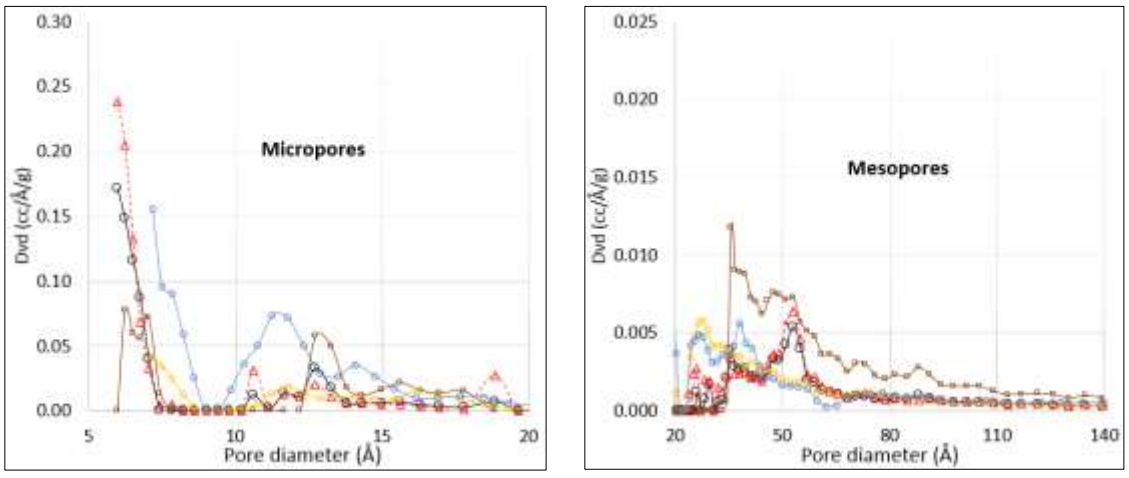

(b)

Figure 7.2. Analysis of (a) adsorption-desorption isotherms and (b) pore size distribution of activated carbons

The pore size distribution analyzed by using NLDFT (non-local density functional theory) shows the heterogeneous structure of porous material. The pore size width of less than 20 Å is classified as micropores, while the size between 20 and 500 Å is classified as mesopores. Above 500 Å is macropores. This study found that the activated carbons mostly contained micropores with some mesopores. The height of curvature at an initial relative pressure as illustrated in Figure 7.2 (a) was highly correlated to the pore size of less than 10 Å and in the larger area below 10 Å from Ni/AC, RSAC750, RSAC850, RSAC650, and RSAC550, a higher height of the isotherm curvature at an initial relative pressure was obtained. Aside from the width of less than 10 Å, the predominant pore widths were found at 11.7 Å with Ni/AC, 10.6 Å with RSAC750, 12.9 Å with RSAC850, 13.3 Å with RSAC650, and 11.8 Å with RSAC550. The increased pore width at around 10 Å was caused by the nickel impregnation on RSAC750 as the largest pore width of nickel was found near 15 Å [211].

The BET surface area and the pore volumes are shown in Table 7.1. The largest surface area (1330 m^2/g) of the activated carbon was produced at a temperature of 750 ^oC, while the smallest (373 m^2/g) was from 550 ^oC from rice straw bio-char (6 m^2/g). The surface area (1076 m^2/g) at the highest operating temperature at 850 ^oC showed narrower than that at 750 ^oC as a result of the breakage of the micropore walls forming larger macropores [75]. This led to the decrease in pore volume from 0.522 cm^3/g with RSAC750 to 0.375 cm^3/g with RSAC850. From the comparison of the surface area and pore volume at 650 and 850 ^oC, one (RSAC850) represented a higher surface area whereas the other (RSAC650) showed a higher pore volume. This can be explained by

the different portion of mesopores and micropores. The more mesopores induced a broader volume, while more micropores resulted in a broader surface area. The nickel impregnation on RSAC750 decreased both the surface area (1330 m^2/g) and pore volume (0.522 cm^3/g) of RSAC750 to 1102 m^2/g and 0.489 cm^3/g. As nickel is known as a nonporous or macroporous material based on the isotherm from Zhang et al. [211], the surface area and volume per gram should be reduced accordingly.

Table 7.1. BET surface areas and pore volume of activated carbons

	surface area (m^2/g)	pore volume (cm^3/g)
RS char	6.0	N/A
RSAC 550	373.2	0.200
RSAC 650	870.6	0.445
RSAC 750	1331 ±54	0.522 ±0.086
RSAC 850	1076.9	0.375
Ni/AC 750	1102.6	0.489

Ultimate analysis of raw biomass, bio-char, and activated carbons was done to find the elemental compositions of carbon, hydrogen, nitrogen, sulfur and oxygen (by difference after considering ash content) as shown in Table 7.2. The low carbon content of raw biomass (36%) was increased in char after pyrolysis at 500 ^oC, while the oxygen was significantly reduced with an increase in ash content due to the combination of decarboxylation, dehydration, and demethylation reactions. After the activation of bio-char, the ash content was noticeably reduced at the lowest temperature of 550 ^oC as the activation process including KOH, HCl solution, and water washing removed the

washable ashes. However, the ash content was again increased at increasing activation temperatures because of the removal of the VCM content. The hydrogen, nitrogen and oxygen were mainly volatilized during the activation, which led to a relative increase in ash content at a higher activation temperature. Thus, the H/C and O/C ratios decreased as the activating temperatures increased. The degree of changes were almost constant above 750 ^{o}C. Similar results of an increase in carbon and a decrease in hydrogen, nitrogen, and oxygen contents during KOH activation were reported by previous studies [212,213].

Table 7.2. Ultimate analysis of activated carbon of rice straw on a dry basis.

	C	H	N	S	O*	ash	H/C	O/C
Rice straw[a]	36.6	4.90	0.77	0.230	32.0	21.7	1.61	0.66
RS char[a]	45.1	2.13	1.40	0.235	6.2	45.0	0.57	0.10
RSAC 550	64.8	2.75	1.80	0.106	17.0	13.6	0.51	0.20
RSAC 650	65.4	2.06	1.71	0.088	14.9	15.9	0.38	0.17
RSAC 750	67.5	1.09	0.54	0.052	9.1	21.8	0.19	0.10
RSAC 850	67.1	1.16	0.76	0.068	8.5	22.4	0.21	0.10

* By difference

[a] the elemental and ash data was referenced from the previous study (Chapter 5)

Figure 7.3 shows the SEM images and EDX (energy dispersive X-rays) spectrums of RSAC (activated carbon) at 750 ^{o}C and its nickel impregnated Ni/AC. Both of the images show a generation of pores after the carbonization. Some pores on the surface of the straw can also be identified. The EDX scanned chemical compositions were determined by averaging 6 random scans on a 0.5 × 0.5 mm SEM screen. The normalized chemical compositions were shown in an agreement with the elemental data

obtained from an ultimate analyzer shown in Table 7.2. The carbon and oxygen was mostly comprised of the AC as well as a trace of silicate and potassium as is also discussed in the XRD analysis. The normalized wt.% of impregnated nickel on AC was determined to be 9.1% after averaging 6 scans. The Ni/AC was evaluated as a catalyst for fuel upgrading, which can be substituted for an expensive noble metal catalyst that will be discussed in a later section.

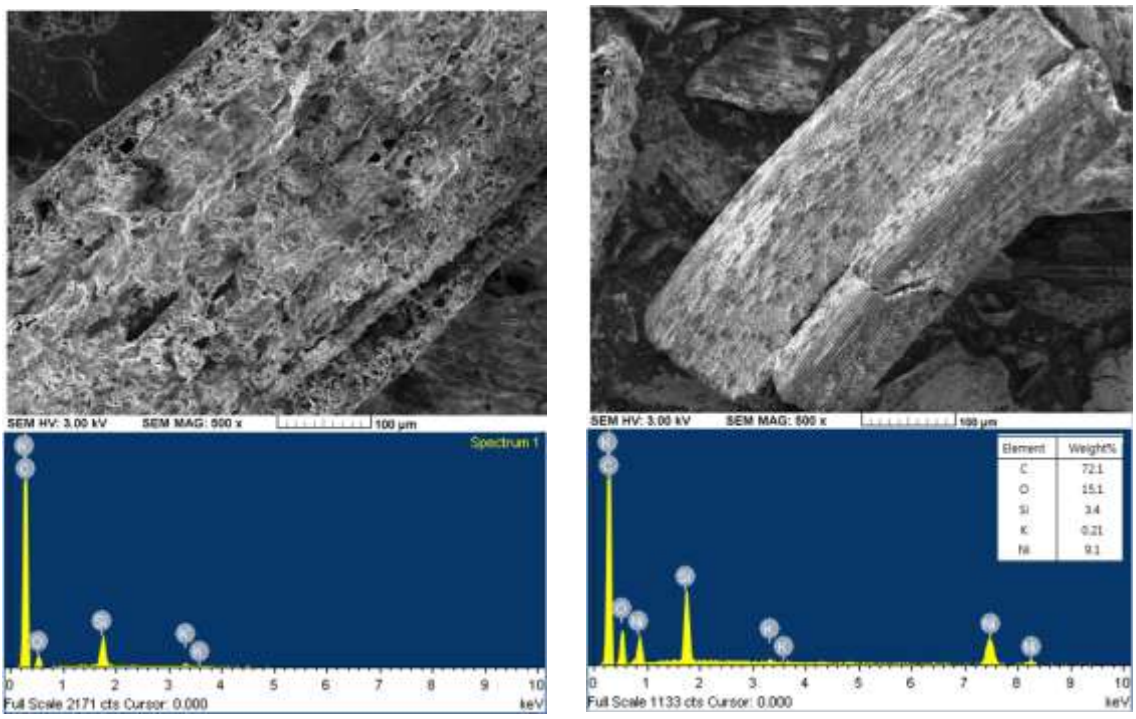

(a) (b)

Figure 7.3. SEM and EDX of (a) activated carbon and (b) nickel impregnated carbon.

The XRD patterns of bio-char, activated carbons, and nickel impregnated carbons were analyzed and are presented in Figure 7.4. As a previous study reported, the

XRD patterns ① of bio-char (Chapter 5) [214-216], the char included sylvite (KCl) at the angles at 2Θ = 28.3º and 40.4º, amorphous silica (cristobalite, SiO_2) at 2Θ = 22.5º, and quartz (SiO_2) at 2Θ = 26.6º. Also, broad peaks of 2Θ = 15º – 30º indicated randomly oriented aromatic layers in the amorphous carbon structure [213]. The broad peak at around 2Θ = 24º is attributed to an amorphous silica content in the untreated bio-char. The amorphous carbon patterns were reduced as a higher mole KOH solution and a higher activating temperature were applied as indicated at ②, ③, and ④. The complete removal of Ca and K related peaks by KOH washing was obtained from 8M KOH AC of ③ and ④. A further removal of the amorphous carbon peak of wide and weak was found from 8M KOH at 750 ºC pattern ④ indicating the presence of more ordered carbon structures. In other words, the removal of volatiles from the bio-char reveal a sharp peak near 43º and 53º, which was expected to be copper (Cu). The XRD pattern confirmed the formation of more structured carbon along with increasing temperature conditions. The sharp peak on the pattern indicated a highly crystalline structure [73]. The patterns of ⑤ and ⑦ represented nickel impregnated on commercial activated carbon ⑥ and developed activated carbon ④ at 750 ºC. Nickel peaks were determined at 44.5º on (111) plane and 51.8º on (200) plane which was also detected in the same degree from a previous study [211]. This also indicated the presence of nickel impregnated on the activated carbon.

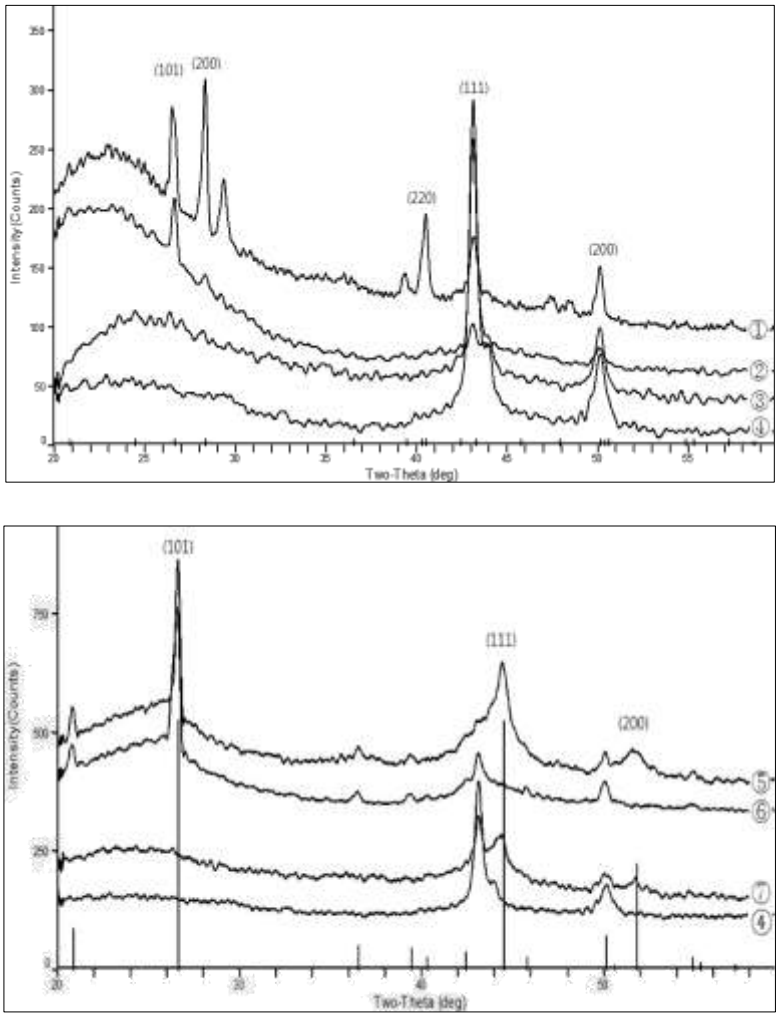

Figure 7.4. XRD of activated carbons and nickel impregnated activated carbons (① untreated bio-char, ② AC in 3M KOH at 750 ºC, ③ AC 8M KOH at 550 ºC, ④ AC 8 M KOH at 750 ºC, ⑤ Ni-C, ⑥ C, and ⑦ Ni-AC).

7.3.2. Electrode material application for a supercapacitor

The electrochemical tests of the produced activated carbon of commercially available, Ashe Juniper waste and rice straw samples were conducted to evaluate their performance as supercapacitors. Figure 7.5 (a – c) indicates a specific capacitance (F/g) of three activated carbons at different sweep rates (10, 50, and 100 mV/s), and Figure 7.5

(d) represents cyclic voltammograms of three samples at 10 mV/s for direct comparison purposes. A general trend in specific capacitance at an increasing sweep rate was decreased from 42 to 30 F/g for a commercial carbon, 35 to 22 F/g for AJAC, and 93 to 56 F/g for RSAC because of ion diffusion and adsorption arrival delays inside the smallest pores. This phenomena is often observed in activated carbons [84]. At the slowest sweep rate of 10 mV/s, the closest rectangular shape of a CV was obtained, but it was not symmetrical, indicating a substantial pseudocapacitance contribution to all of the carbons. The AJAC sample showed the worst symmetrical shape with peaks, which was associated with unbalanced reduction and oxidation (redox) reactions. On the other hand, the commercial carbon with the least oxygen containing functional groups among other samples showed the fewest redox reactions. The pseudocapacitance peaks had almost disappeared at the sweep rate of 100 mV/s with a commercial carbon.

The small surface areas of AJAC of 480 m^2/g and commercial carbon of 680 m^2/g contributed to a lower slope at the 0 – 0.2 V region compared to that of RSAC, which also led to a smaller ion adsorption capacity. Even though the strongest EDLC electrode was found from a commercial carbon, the highest specific capacitance was found from RSAC with 93 F/g at 10 mV/s compared to the other two samples as indicated in Figure 7.5 (d). The obtained capacitance of RSAC can be used as it meets the commercially available supercapacitors of 70 – 120 F/g. Some other activated carbon capacitors were reported. ACM8 (activated carbon of green monoliths) in 1 M H_2SO_4 showed 80 F/g at 1 V and 1 mV/s [217]. Activated carbon of cellulose and wood in 1 M $TEABF_4$

(tetraethylammonium tetrafluoroborate salt) in acetonitrile, respectively, represented 140F/g and 236 F/g at 2 V and 1mV/s [84].

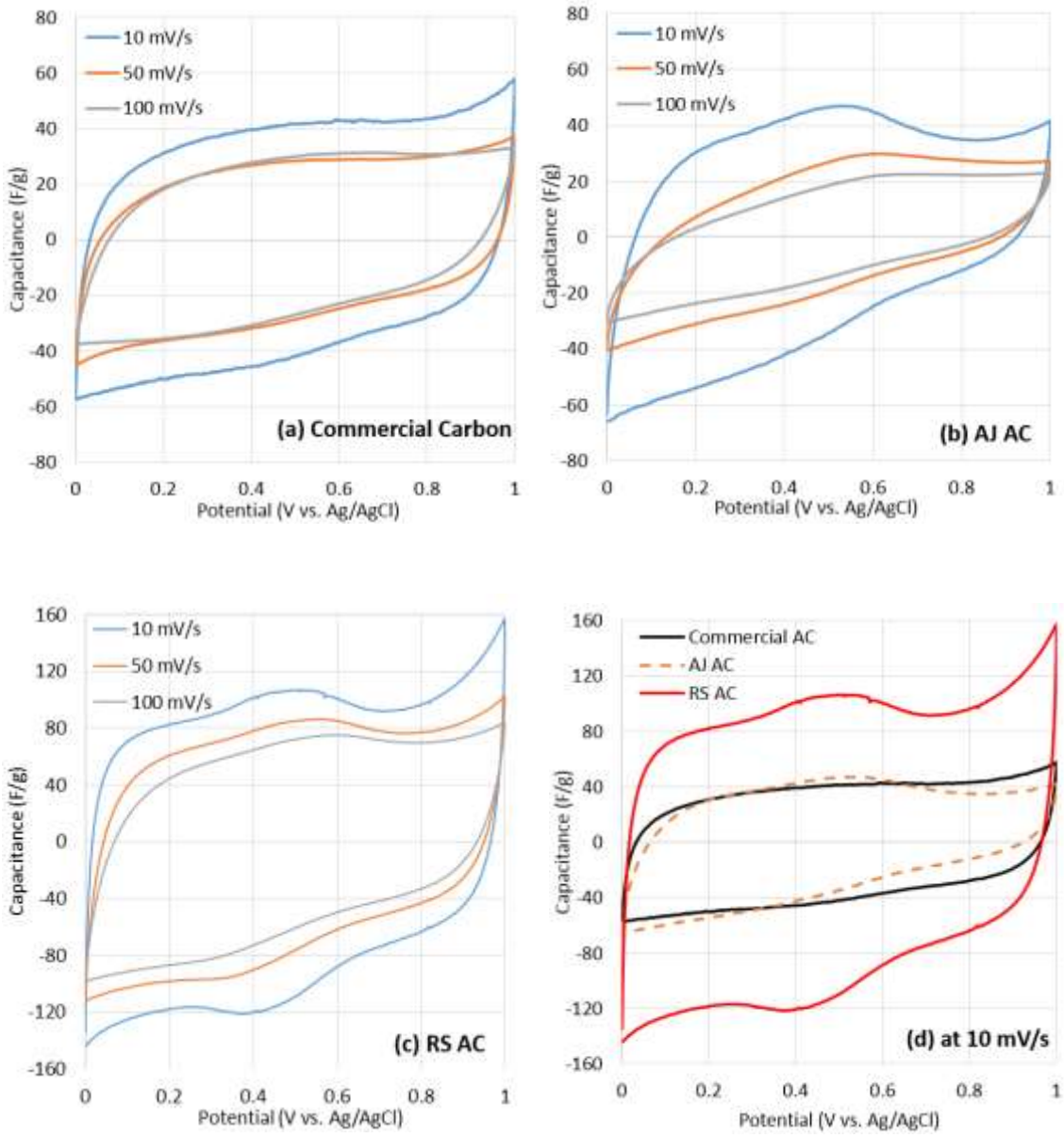

Figure 7.5. Cyclic voltammograms of (a) commercial carbon, (b) Ashe Juniper activated carbon, (c) rice straw activated carbon, and (d) comparison voltammograms of three activated carbons at 10 mV/S.

7.3.3. Adsorption of acetaminophen and ibuprofen

Table 7.3 shows the percent of acetaminophen and ibuprofen removal from the initial concentration. After 24 hours of agitation of the pharmaceutical solution and activated carbon, the acetaminophen and ibuprofen were reduced by 95.0% and 95.3%, respectively, which was similar to the percent of removal reported by other studies; 95.9% of Eriochrome Black T dye using rice straw activated carbon by Luna et al. [78] and 99% of acetaminophen contaminant using pomegranate wood activated carbon by Mashayekh-Salehi and Moussavi [79]. The adsorption was conducted under pH ranges from 2 to 12. The removal percent declined from 83 to 70% when the pH was decreased from 10 to 12 due to no electrostatic attraction occurrence at a higher pH. It was also determined by Liu et al. [80] that the removal percent of acetaminophen was almost constant (91 – 92%) under a pH from 2 to 9, while a pH above acetaminophen pK_a of 9.38 led to a significant removal rate of 70%. This was expected due to the electrostatic repulsion between the negatively charged activated carbon and anionic solution. In the case of ibuprofen, a pH < 4 resulted in over 90% removal while a pH > 4 led to a significant decrease due to electrostatic repulsion as reported by Mestre el al. [81]. Thus the pH has to meet the acid-base property of the contaminant.

Table 7.3. Adsorptive removal of acetaminophen and ibuprofen solution using rice straw activated carbon at 750 ^{o}C.

Compounds	Initial conc.	Final conc.	% Removal
Acetaminophen	10.0 mg/L	0.50 mg/L	95.0%
Ibuprofen	10.0 mg/L	0.47 mg/L	95.3%

7.3.4. Catalyst application for pyrolytic bio-oil upgrading

Upgrading of vacuum distilled bio-oil was conducted using a developed Ni/AC and Pd/C for comparison under the same operating condition of 190 ^{o}C and 4.1 MPa of hydrogen gas. The temperature condition used for distillation was set at 120 ^{o}C and the second fraction was used for the current experiment.

Table 7.4 shows the product yields of upgraded biofuel with two different catalysts of palladium (Pd) and nickel (Ni) impregnated on carbons. The reason for using a Pd/C catalyst for upgrading comparison was that it has been reported as one of the best catalysts for pyrolysis bio-oil [99]. A higher product yield of 72% was found from Pd/C compared to a 63% yield with a Ni/AC catalyst. The upgraded product yields of different bio-oils with different catalysts showed higher product yields of 43% with Pd/C at 250 ^{o}C [99] and 53% with Pd/C at 300 ^{o}C [218], while they are lower than the yields of 86% with zeolite upgrading at 215 ^{o}C [219]. A higher yield of Pd/C upgraded bio-oil can be explained by the amount of hydrocracking. The more hydrocracking took taken a place with Ni/AC from a higher amount of loss + gas than that from Pd/C, indicating that nickel helped better in cracking carbon chains. The amount of coke and tar was found at more or less 21% from both the catalysts as the amount of coke varied highly depending on the temperature and the residence time conditions [220].

Table 7.4. Percentile yields of products after hydrotreatment.

	Temp. – Pressure	Yield	Coke	Tar	Loss+Gas
F2 – Pd/C	190 ^{o}C – 4.1 MPa	72%	7%	13%	7%
F2 – Ni/AC	190 ^{o}C – 4.1 MPa	63%	6%	16%	15%

The total acid number (TAN) and moisture content (MC) of bio-oil, distillates, and the upgraded bio-oils were measured as well as their higher heating value (HHV). The TAN value shows the total acid chemicals in the bio-oil so that it directly indicates the concentration of acidic compounds that corrode metallic materials.

A TAN of 12.2 mgKOH/g varied to 0.1 mgKOH/g in the light fraction and 21.5 mgKOH/g in the middle fraction after distillation. The tendency of lower acidity in the lighter fraction was also reported from a previous study by Jewel and Capareda [93] that the light and middle fraction of corn stover bio-oil were 4.1 and 15.1 mgKOH/g, respectively. The middle fraction (F2) of 21.5 mgKOH/g after upgrading was significantly reduced to 5.7 mgKOH/g with Pd/C and 5.5 mgKOH/g with Ni/AC. An increase in a saturated hydrocarbon from the unsaturated mainly caused the decrease in TAN. By blending or further treatment, the TAN can be reduced to meet the standards of petro based fuel. Moisture content indicates the amount of water included in the chemicals. An initial MC of 8.2% was greatly reduced in the distillation fractions, whereas the MC of upgraded fractions was barely reduced from the vacuum distillated fractions (F2). Due to the small amount of water formed during the hydrotreating, the separation was not made under the reactions [218]. The HHV of upgraded fuels from F2 (41.1 MJ/kg) was merely increased to 41.7 MJ/kg for Pd/C and 41.4 MJ/kg for Ni/AC. However, a higher HHV of distillates and upgrades was determined compared to HHVs of the direct microalgae bio-oil zeolite upgrading (37.5 – 39.6 MJ/kg) [219] and the distilled corn stover bio-oil Ru/C upgrading (40.2 MJ/kg) [218]. A hydrothermal catalytic study of pretreated microalgae oil by Bai et al. [221] reported that the upgraded

bio-oil with Pd/C at 400 ºC was 42.6 MJ/kg. The physical properties of MC and HHV of distillates and upgrades were close to the crude oil and biodiesel standards, while further treatment may be required to reduce the TAN.

The elemental compositions of algal bio-oil, distillates, and upgrades were analyzed to understand how the physical and chemical treatments effectively improved the fuels shown in Table 7.5. The carbon and hydrogen content was raised from bio-oil to upgrades by 6% and 14%, while the sulfur and oxygen contents were reduced by 86% and 42%. Through the reduction reaction, the oxygen and sulfur were removed mostly after reaction with hydrogen purge. Also, many unsaturated hydrocarbons were saturated, which will be discussed in a following section. The significant hydrodeoxygenation and hydrodesulfurization reactions through hydrotreating compared to distillation improved the fuel to be even close to petro fuel. However, the nitrogen (5 – 6%) and oxygen (about 7%) compounds still need a further treatment for deoxygenation and denitrogenation. The variation of the two elemental compositions from different catalysts were minimal like the other physical characteristics of upgrades. The results from the physical and elemental data indicated that the much cheaper metal catalyst nickel can economically replace the expensive noble metal palladium.

Table 7.5. Physical and elemental properties of bio-oil, distillates, and upgrades compared to the petro fuels (V_F1: vacuum distilled fraction 1).

	TAN (mgKOH/g)	MC (%)	HHV (MJ/kg)	C	H	N	S	O*
Bio-oil	12.2	8.2	38.6	72.2	9.7	6.0	0.22	11.9
V_F1	0.10	1.7	40.5	66.3	9.4	4.1	0.20	19.9
V_F2	21.50	0.50	41.1	74.1	10.4	5.2	0.17	10.1
5% Pd/C of F2	5.73	0.69	41.7	76.6	11.12	5.3	0.03	6.93
10% Ni/AC of F2	5.46	0.48	41.4	76.6	11.05	5.2	0.05	7.05
Crude oil [21]	-	<0.5	41~43	83-87	14-10	0.1-2	0.05-6	0.05-1.5
FAME [26]	<0.5[a]	<0.05[a]	39	76.2	12.6	-	-	11.2
Gasoline [27]	-	-	43~47	85-88	15-12	-	-	-

* by difference

[a] biodiesel standard – ASTM D6751

For a better understanding of the upgraded elemental data, a van Krevelen plot was used as shown in Figure 7.6. H/C and O/C ratios of bio-oil were 1.61 and 0.12 that were distilled into fraction 2 of H/C (1.68) and O/C (0.05) toward the direction of a decarboxylation reaction. The ratios of upgrades located in ranges at a steeper decarboxylation slope from distillates due to the initial distillation that was already dehydrated. The hydrogen enrichment and oxygen removals during the hydrotreating process upgraded the microalgae fuel of ratios (H/C: 1.73 – 1.74 and O/C: 0.034 – 0.035) even closer to the ratios of petro fuels. Previous upgrading studies showed similar ranges of ratios. Bai et al. [221] reported H/C (1.64) and O/C (0.027) from Pd/C upgrading with a mixture of water and pretreated microalgae oil at 400 ^{o}C, Maguyon [219] showed H/C (1.55) and O/C (0.058) from zeolite upgrading with microalgae oil at 250 ^{o}C, and Capunitan and Capareda [218] obtained H/C (1.51) and O/C (0.102) from Ru/C upgrading with distilled corn stover bio-oil at 300 ^{o}C.

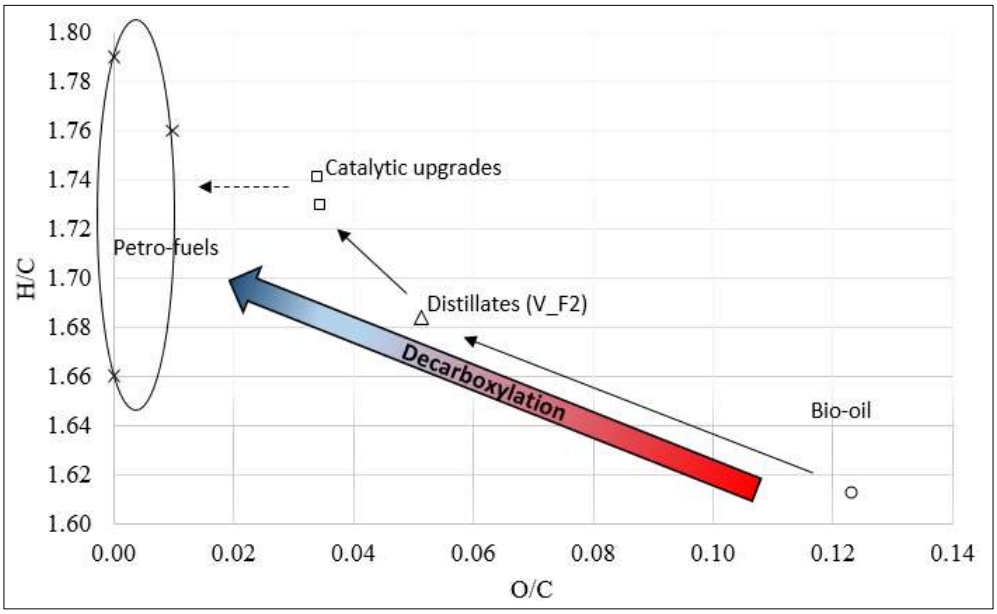

Figure 7.6. Van Krevelen diagram of bio-oil, distillate, upgrades and petro-fuels.

The upgraded microalgae bio-oil chemical compounds were also analyzed for a further understanding of the chemical transitions by GCMS. The compounds were sorted into several functional chemical groups of saturated hydrocarbons (paraffin and naphthene), unsaturated hydrocarbons (olefin and aromatic), N-containing (aromatic N. and nitrile), O-containing (ketone and other oxygenates), and others. For a better comparison, chemical compositions of bio-oil and vacuum fractionates were also categorized as shown in Figure 7.7.

Significant chemical transitions were made from unsaturated hydrocarbons to saturated hydrocarbons after the distillation and hydrotreatment of raw bio-oil. The relative percent of paraffin and olefin after distillation of raw bio-oil increased, and that of the ketone and nitrile decreased. An increase in saturated hydrocarbons and a decrease in ketone after distillation resulted in a better stabilized biofuel, while the unsaturated

hydrocarbon (olefin) was still high. A commercial 5% Pd/C and a developed 10% Ni/AC catalyst were used for further upgrading the distillate (Fraction 2). The same tendency of chemical group transitions were recognized as; a further increase in saturated hydrocarbons and aromatics, and a decrease in olefin and nitrogen/oxygen containing compounds. However, the degree of chemical group changes were different with the two catalysts as a higher amount of saturated hydrocarbons with a Pd/C catalyst were obtained compared to the amount with a Ni/AC catalyst, whereas a lower olefin and nitrile with Pd/C catalyst was obtained. The four most abundant chemicals from catalyst upgrading were undecane ($C_{11}H_{24}$), dodecane ($C_{12}H_{26}$), tridecane ($C_{13}H_{28}$), and hexadecane ($C_{16}H_{34}$), which comprised 54.2 – 56.5%.

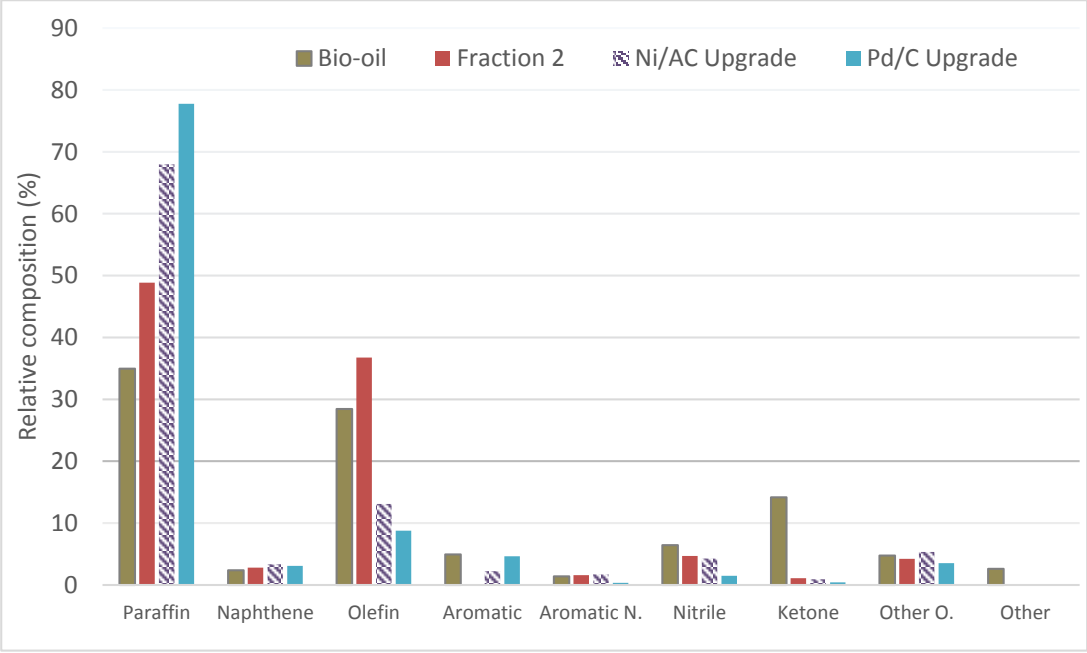

Figure 7.7. Chemical groups of upgraded bio-fuel analyzed by GC-MS.

The four major chemical groups of paraffin, olefin, total aromatics, and nitrile were further analyzed based on carbon numbers as indicated in Figure 7.8. The carbon ranges were decided based on the aviation fuel ($C_8 – C_{16}$) lower boiling point of 126 ^oC and upper boiling point of 287 ^oC [102]. The paraffin group, as indicated previously, showed the most amount in a range of $C_8 – C_{16}$ that the paraffin distillate (47%) increased to 65% with Ni/AC and 73% with Pd/C. On the other hand, the olefin distillate (21%) of the $C_8 – C_{16}$ range decreased to 11% with Ni/AC and 7% with Pd/C. The unsaturated hydrocarbon of olefin was converted into saturated hydrocarbons through a hydrogenation reaction with an H_2 [222]. Similar to the increase in paraffin, the aromatics with a range of $C_8 – C_{16}$ increased almost twice the original percent from both catalyzed bio-oils. The upgrade with an Ni/AC catalyst was prone to cracking as more of $< C_8$ aromatics were determined. The combination reactions of cracking, methylation, alkylation, and dealkylation incurred for the changes of chemical compositions over catalytic conversions [223]. A better removal of the nitrile group with Pd/C was made over all the different carbon ranges compared to removal with Ni/AC that showed an increased nitrile composition with a lower carbon number range.

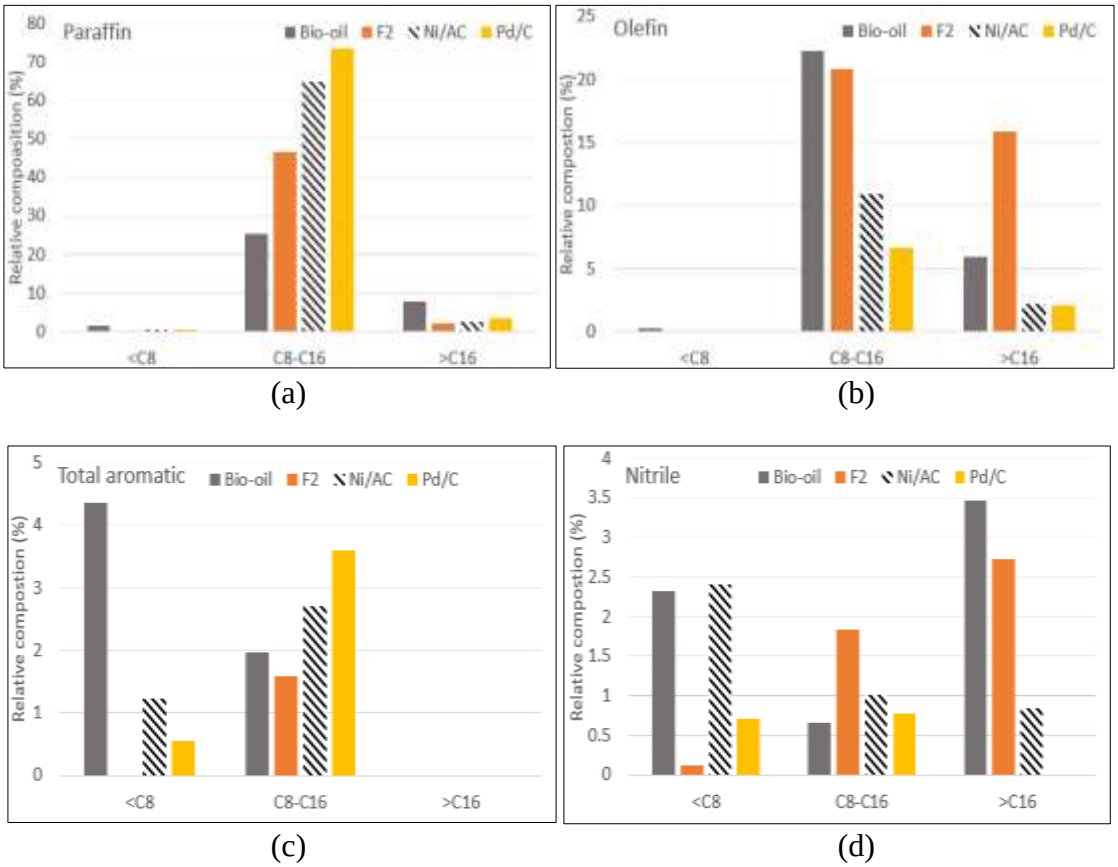

Figure 7.8. Carbon number distributions of distilled and upgraded bio-oil based on the chemical groups.

The catalysts used in the hydrotreatment of bio-oil were investigated. The nitrogen and sulfur of both the catalysts were substantially increased. Especially, the increase of sulfur in the catalysts helped in the removal of sulfur from bio-oil, as indicated in Table 7.5 and Table 7.6. Approximately 2% of the sulfur of bio-oil was decreased to 0.04% after upgrading, while that of the catalysts increased from 0.05% to 2.21% for Ni/AC and 0.07% to 0.60% for Pd/C. A higher sulfur was ionized on the Ni/AC catalyst than the Pd/C, which may require a reduction process to remove the

element. However, the over 2000 times cheaper price of nickel than palladium may compensate for a further step in a more intense recycling process.

Table 7.6. Elemental data for catalysts used after bio-oil upgrading.

VD F2 upgrading	C	H	N	S
RSAC 750	67.5	1.09	0.54	0.052
Used Ni/AC	66.1	3.36	2.39	2.210
Pd/C 5%	73.5	1.47	0.19	0.071
Used Pd/C	82.2	2.28	1.53	0.600

7.4. Conclusions

Bio-char, one of the major products from the thermochemical conversion process of pyrolysis, and gasification was utilized and upgraded to activated carbon. A KOH chemical activation was applied at different activation temperatures to find an optimum condition for the largest surface area and micropores. Then the performance of activated carbon was evaluated for adsorption and capacitance materials and the metal support for catalytic bio-oil upgrading.

The largest surface area and the most micropores were found at the activation temperature of 750 ^{o}C; as much as 1330 m^2/g composed of most micropores and some mesopores. Up to 95% of the acetaminophen and ibuprofen pollutants in an aqueous solution was removed using activated carbon after a 24 hour contact time. The activated carbon as a supercapacitor showed both EDLC (electrical double layer capacitor) and pseudocapacitance natures. The highest specific capacitance was obtained from RSAC at 93 F/g, followed by commercial carbon at 42 F/g and AJAC at 35 F/g, which value

showed a modest specific capacitance. The nickel impregnated on the activated carbon also successfully improved the vacuum distilled microalgae bio-oil by 42% deoxygenation and 86% desulfurization. The upgraded bio-oil product was recovered with a 63 – 72% yield. The H/C and O/C ratios of upgraded bio-oil from raw oil was close to the petro-based fuels. The paraffin and aromatic contents were increased after upgrading, while the olefin and nitrile compounds decreased and cracked to form smaller carbon chains.

8. CONCLUSION AND FUTURE WORK

8.1. Overall Conclusion

Three thermochemical processes of torrefaction, pyrolysis, and gasification were applied to convert the wastes into other forms of products. Many wastes were utilized to understand their conversion and product properties. The applied wastes used in this study included agricultural residues of rice straw and cotton stalk, aquatic waste of microalgae, and animal/human wastes of sewage sludge and dairy manure, which can be converted into clean energy sources and other value added products. Before the main thermochemical process, all the biomass wastes require a pre-process such as chopping, drying, separating or else. Sand mixed dairy manure directly from a dairy was intensively investigated to be used for gasification process. Also, the produced bio-char and bio-oil has been gone through value-adding stages of hydrotreatment of bio-oil and activation of bio-char for adsorbent material, capacitance material, and catalyst.

Dairy manure mixed with sand was improved by removing sand to be able to use as a fuel source. First, the manure and sand particle size was understood with pretreatment conditions of Dry_Gr, Dry_NGr, 10%_Gr, and 22%_Gr. Based on the results of the ash content and the recovered manure yield after sieving, the conditions of of Dry_Gr and 10%_Gr were suggested for a scaling-up process with a sieve mesh-40. The four stages of pilot process were designed and completed as air drying, burner drying, grinding, and sand separating. The as-received dairy manure after the four stages was recovered by 25 wt% with ash contents between 40 and 50% from the initial ash

content of 72%. The mineral analysis of the processed manure predicted low potential to induce the bed agglomeration and slagging problems due to large amount of silicate. However, a longer exposure time on the bed with the dairy manure resulted a bed agglomeration. Finally, the gasification was successfully operated with the processed dairy manure with LHV of 3.3 MJ/Nm^3.

Enriched-air fluidized bed gasification with the processed dairy manure were operated based on the surface methodology to investigate the effect of temperature, ER_m and oxygen concentration on the syngas compositions and LHVs. The most significant condition on all of the syngas compositions and LHVs was a temperature term. The next significant term on the syngas compositions was ER_m on H_2, and oxygen concentration on CO and CO_2. The carbon conversion efficiency was affected mainly by ER_m. The highest LHV of syngas with enriched air gasification was obtained as 8.0 MJ/Nm^3 at the operating condition of 800 ^oC-0.25-40% (temperature-ER_m-oxygen), while the maximum LHV from the air gasification was 5.7 MJ/Nm^3 at the condition of 800 ^oC-0.1-21%. A higher carbon conversion efficiency of 45 – 90% was obtained than the cold gas efficiency of 19 – 63%. The empirical equations obtained from the bench-scale experiments were predicted the composition of syngas from a fluidized bed pilot-scale TAMU gasifier to perform the economic analysis within 10% error.

Torrefaction study was conducted with two agricultural wastes of rice straw for straw type and cotton stalks for woody type. The conditions of temperature (210 – 290 ^oC) and residence times (20 – 60 min) were applied to find the product yields and characteristics products in a batch reactor. The highest HHV of 28.6 MJ/kg was obtained

from rice straw at the temperature of 290 ºC, which can be a substitute for brown coal and peat. The maximum solid energy densification for RS was 1.48, which was higher than that for CS at 1.37. The weight reduction by 52% for RS and 63% for CS at 290 ºC with the energy recovery was over 70 – 80% can alleviate the difficulties of storage and transportation. The liquid products were mostly composed of water and majority of acids that can be used for soil amendment. The empirical equations based on the response surface methodology would help predicting the main properties of char at conditions.

Pyrolysis with three reactors (an auger, a batch, and a fluidized bed) was performed to convert rice straw waste into three products at 500ºC. The main purpose of this work was done for a direct comparison of the effect of reactors on the product properties. The process of the auger and batch reactors as slow and intermediate pyrolysis resulted in higher yields of bio-char (45 -48 %) than the yield produced from a fluidized bed reactor. On the other hand, the largest quantity of bio-oil (43%) was obtained from a fast pyrolysis. A better HHV and element ratios of H/C and O/C of bio-oil was obtained from slow pyrolysis, and their majority chemicals were composed of phenols and aliphatic compounds. The auger reactor was found as an intermediate process reactor that showed better quality of bio-oil than a fluidized bed reactor and more or similar bio-oil quantity compared to that from a batch reactor. The bio-char represented a similar characteristics regardless of the production reactor as all of the elemental ratios from different reactors was ranged in 0.02 – 0.10 for O/C and 0.56 – 0.78 for H/C. This study will help select the type of pyrolysis reactor for appropriate product applications.

The applications of the main products of bio-char and bio-oil were further investigated. First, the rice straw bio-char from a batch reactor pyrolysis was used for the KOH chemical activation. The different activation temperatures were applied to investigate the changes of pore sizes and volumes. At 750 ^{o}C, the highest surface area (1331 m^2/g) and volume (0.522 cm^3/g) was obtained. The SEM, XRD, and EDX analyses on the activated carbon besides a BET analysis were implemented to understand the improved carbons. Then, the performance of the activated carbon was evaluated for the chemical adsorption and electrical capacitance. It removed over 95% acetaminophen and ibuprofen contamination from aqueous solution in 24 hours. The RSAC (rice straw activated carbon) showed 93 F/g specific capacitance property, which is equivalent to the commercially available supercapacitors of 70 – 120 F/g. The

The microalgae bio-oil was selected to be upgraded as the bio-oil showed a higher HHV compared to other bio-oil from rice straw, sewage sludge, and Beauty Leaf Tree de-oiled cake. The first upgrading was a vacuum distillation to fractionate the bio-oil into three fractions to remove most of heavy chemicals such as paraffin gum and wax. At the same time, the bio-oil can be improved by reduction in the oxygen content and viscosity and increase in HHV. The distillates then were gone through hydrotreatment using a commercial catalyst (Pd/C) and a developed catalyst (Ni impregnated on rice straw activated carbon). The oxygen content of upgraded bio-oil was reduced by 31% from distillate and 42% from raw bio-oil. The sulfur content was significantly reduced by 83%. A higher HHV was achieved at 41.4 MJ/kg. Both the

catalysts worked similar on the properties of bio-oil. Over 2000 times cheaper price of nickel would take an advantage over palladium.

8.2. Future Work

Based from the studies discussed above, further investigations on the following topics can be conducted as a continuing work. Especially, the author would like to finish some studies illustrated below; the development of adsorption material for contamination removal, LCA study, the development of solar assisted pyrolysis reactor, and engine operation studies.

- **Gasification**

- Steam operated gasification
- CO_2 and N_2 removal, and H_2 storing studies using different adsorption materials
- Engine operation studies and its emission level

- **Torrefaction**

- Pellet performance of torrefied chars
- Evaluation of moisture adsorption capacity
- Chemical extraction studies using various acid or base solutions

- **Pyrolysis**

- Designing a new solar assisted pyrolysis reactor

- Catalytic pyrolysis with a direct distillation condenser

- **Bio-char utilization**

- Production of activated carbon at the various conditions and biomass wastes
- Adsorption removal of volatile organic compound
- Supercapacitor application with different pore characterization

- **Bio-oil utilization**

- The emission changes and engine or combustor efficiencies with produced raw bio-oil, upgraded bio-oil, and mixed bio-oil with petro fuels.
- The effect of the aqueous phase on soil amendment
- Aqueous phase fuel upgrading

- **Processing integration, simulation, modelling and economics**

- Modelling and simulation studies using EES, ASPEN, and ANSYS Fluent
- Economic evaluation of each process or value added products
- LCA (life cycle assessment) of combined process cycles

REFERENCES

[1] J. Hull, The Second Industrial Revolution: The History of a Concept, Storia Della Storiografia. (1999) 81-90.

[2] R. Saxena, D. Adhikari, H. Goyal, Biomass-based energy fuel through biochemical routes: A review, Renewable and Sustainable Energy Reviews. 13 (2009) 167-178.

[3] W. Tsai, M. Lee, Y. Chang, Fast pyrolysis of rice husk: product yields and compositions, Bioresour. Technol. 98 (2007) 22-28.

[4] M.J. Prins, K.J. Ptasinski, F.J. Janssen, Torrefaction of wood: Part 2. Analysis of products, J. Anal. Appl. Pyrolysis. 77 (2006) 35-40.

[5] FAOSTAT, Food and agriculture organization of the United Nations, 2012 (2012).

[6] R. Bakker, H.W. Elbersen, R.P. Poppens, J.P. Lesschen, Rice Straw and Wheat Straw: Potential Feedstocks for the Biobased Economy, NL Energy and Climate Change, Utrecht, The Netherlands, 2013.

[7] R.L. Nelson, P.K. Thor, C.R. Heaton, A.F. Scheuring, O.E. Thompson, L. Garoyan, L. Horel, R.S. Bringhurst, V. Voth, R. Sharma, Rice straw burning: Alternative policy implications, Order. (1980).

[8] D. Bainbridge, Alternative Uses of Rice-Straw in California, No.94-330 (1997).

[9] D.A. Grantz, D.L. Vaughn, R.J. Farber, B. Kim, L. Ashbaugh, T. VanCuren, R. Campbell, D. Bainbridge, T. Zink, Transplanting native plants to revegetate abandoned farmland in the western Mojave Desert, J. Environ. Qual. 27 (1998) 960-967.

[10] G.M. Rogers, M.H. Poore, J.C. Paschal, Feeding cotton products to cattle, Veterinary Clinics of North America: Food Animal Practice. 18 (2002) 267-294.

[11] Arizona Crops. January 19, [USDA] Arizona Agricultural Statistics Service, Phoenix, Arizona, 1996.

[12] Z. Du, Y. Li, X. Wang, Y. Wan, Q. Chen, C. Wang, X. Lin, Y. Liu, P. Chen, R. Ruan, Microwave-assisted pyrolysis of microalgae for biofuel production, Bioresour. Technol. 102 (2011) 4890-4896.

[13] L. Gouveia, A.C. Oliveira, Microalgae as a raw material for biofuels production, J. Ind. Microbiol. Biotechnol. 36 (2009) 269-274.

[14] N. Ashwath, Evaluating Biodiesel Potential of Australian Native and Naturalised Plant Species, Rural Industries Research and Development Corporation, 2010.

[15] S.M.A. Rahman, H.H. Masjuki, M.A. Kalam, M.J. Abedin, A. Sanjid, H. Sajjad, Production of palm and Calophyllum inophyllum based biodiesel and investigation of blend performance and exhaust emission in an unmodified diesel engine at high idling conditions, Energy Conversion and Management. 76 (2013) 362-367.

[16] B.K. Venkanna, C. Venkataramana Reddy, Biodiesel production and optimization from Calophyllum inophyllum linn oil (honne oil) – A three stage method, Bioresour. Technol. 100 (2009) 5122-5125.

[17] V. SathyaSelvabala, D.K. Selvaraj, J. Kalimuthu, P.M. Periyaraman, S. Subramanian, Two-step biodiesel production from Calophyllum inophyllum oil: Optimization of modified β-zeolite catalyzed pre-treatment, Bioresour. Technol. 102 (2011) 1066-1072.

[18] W. Yang, T. Shimanouchi, M. Iwamura, Y. Takahashi, R. Mano, K. Takashima, T. Tanifuji, Y. Kimura, Elevating the fuel properties of Humulus lupulus, Plumeria alba and Calophyllum inophyllum L. through wet torrefaction, Fuel. 146 (2015) 88-94.

[19] W.E. Jokela, Nitrogen fertilizer and dairy manure effects on corn yield and soil nitrate, Soil Sci. Soc. Am. J. 56 (1992) 148-154.

[20] TNRCC, Two Total Maximum Daily Loads for Phosphorus in the North Bosque River, 2014 (2001).

[21] USDA, Milk cows and production by State and region, 2009-2013, 2014 (2013).

[22] D. Morse, R. Nordstedt, H. Head, H. Van Horn, Production and characteristics of manure from lactating dairy cows in Florida, Transactions of the ASAE (USA). (1994).

[23] G.W. Huber, S. Iborra, A. Corma, Synthesis of transportation fuels from biomass: chemistry, catalysts, and engineering, Chem. Rev. 106 (2006) 4044-4098.

[24] A. Dhungana, Torrefaction of biomass, Torrefaction of biomass. (2011) 12-13.

[25] H. Yang, R. Yan, H. Chen, C. Zheng, D.H. Lee, D.T. Liang, In-depth investigation of biomass pyrolysis based on three major components: hemicellulose, cellulose and lignin, Energy Fuels. 20 (2006) 388-393.

[26] T. Fisher, M. Hajaligol, B. Waymack, D. Kellogg, Pyrolysis behavior and kinetics of biomass derived materials, J. Anal. Appl. Pyrolysis. 62 (2002) 331-349.

[27] U. Arena, Process and technological aspects of municipal solid waste gasification. A review, Waste Manage. 32 (2012) 625-639.

[28] L. Devi, K.J. Ptasinski, F.J.J.G. Janssen, A review of the primary measures for tar elimination in biomass gasification processes, Biomass Bioenergy. 24 (2003) 125-140.

[29] H. Knoef, J. Ahrenfeldt, Handbook Biomass Gasification, BTG biomass technology group The Netherlands, 2005.

[30] A.K. Rajvanshi, Biomass gasification, Alternative energy in agriculture. 2 (1986) 82-102.

[31] A. Bridgwater, The technical and economic feasibility of biomass gasification for power generation, Fuel. 74 (1995) 631-653.

[32] P. Lv, Z. Xiong, J. Chang, C. Wu, Y. Chen, J. Zhu, An experimental study on biomass air–steam gasification in a fluidized bed, Bioresour. Technol. 95 (2004) 95-101.

[33] C. Von Fredersdorff, M.A. Elliott, Coal gasification, Chem.Coal Util., Suppl.Vol. 1963 (1963).

[34] F. Pinto, C. Franco, R.N. André, C. Tavares, M. Dias, I. Gulyurtlu, I. Cabrita, Effect of experimental conditions on co-gasification of coal, biomass and plastics wastes with air/steam mixtures in a fluidized bed system, Fuel. 82 (2003) 1967-1976.

[35] J. Fermoso, B. Arias, M. Plaza, C. Pevida, F. Rubiera, J. Pis, F. García-Peña, P. Casero, High-pressure co-gasification of coal with biomass and petroleum coke, Fuel Process Technol. 90 (2009) 926-932.

[36] J.J.R. Behainne, J.D. Martinez, Performance analysis of an air-blown pilot fluidized bed gasifier for rice husk, Energy for Sustainable Development. 18 (2014) 75-82.

[37] F.M. Guangul, S.A. Sulaiman, A. Ramli, Study of the effects of operating factors on the resulting producer gas of oil palm fronds gasification with a single throat downdraft gasifier, Renewable Energy. 72 (2014) 271-283.

[38] A.L. Maglinao, S.C. Capareda, H. Nam, Fluidized bed gasification of high tonnage sorghum, cotton gin trash and beef cattle manure: Evaluation of synthesis gas production, Energy Conversion and Management. 105 (2015) 578-587.

[39] USDOE-ENERGY.GOV, GASIFICATION- Pioneering gasification plants, 2015.

[40] USDOE-ENERGY.GOV, Gasification technology R&D, 2015.

[41] S. Chang, Z. Zhao, A. Zheng, F. He, Z. Huang, H. Li, Characterization of products from torrefaction of sprucewood and bagasse in an auger reactor, Energy Fuels. 26 (2012) 7009-7017.

[42] D. Medic, M. Darr, A. Shah, B. Potter, J. Zimmerman, Effects of torrefaction process parameters on biomass feedstock upgrading, Fuel. 91 (2012) 147-154.

[43] Y. Chen, H. Yang, Q. Yang, H. Hao, B. Zhu, H. Chen, Torrefaction of agriculture straws and its application on biomass pyrolysis poly-generation, Bioresour. Technol. 156 (2014) 70-77.

[44] J. Lee, Y. Kim, S. Lee, H. Lee, Optimizing the torrefaction of mixed softwood by response surface methodology for biomass upgrading to high energy density, Bioresour. Technol. 116 (2012) 471-476.

[45] N. Puy, R. Murillo, M.V. Navarro, J.M. López, J. Rieradevall, G. Fowler, I. Aranguren, T. García, J. Bartrolí, A.M. Mastral, Valorisation of forestry waste by pyrolysis in an auger reactor, Waste Manage. 31 (2011) 1339-1349.

[46] S. Sadaka, M. Sharara, G. Ubhi, Performance Assessment of an Allothermal Auger Gasification System for On-Farm Grain Drying, Journal of Sustainable Bioenergy Systems. 2014 (2014).

[47] A.J. Ashworth, S.S. Sadaka, F.L. Allen, M.A. Sharara, P.D. Keyser, Influence of Pyrolysis Temperature and Production Conditions on Switchgrass Biochar for Use as a Soil Amendment, BioResources. 9 (2014) 7622-7635.

[48] L. Ingram, D. Mohan, M. Bricka, P. Steele, D. Strobel, D. Crocker, B. Mitchell, J. Mohammad, K. Cantrell, C.U. Pittman Jr, Pyrolysis of wood and bark in an auger reactor: physical properties and chemical analysis of the produced bio-oils, Energy Fuels. 22 (2007) 614-625.

[49] A.E. Pütün, E. Apaydın, E. Pütün, Rice straw as a bio-oil source via pyrolysis and steam pyrolysis, Energy. 29 (2004) 2171-2180.

[50] R. Xiao, X. Chen, F. Wang, G. Yu, Pyrolysis pretreatment of biomass for entrained-flow gasification, Appl. Energy. 87 (2010) 149-155.

[51] J. Park, Y. Lee, C. Ryu, Y. Park, Slow pyrolysis of rice straw: Analysis of products properties, carbon and energy yields, Bioresour. Technol. 155 (2014) 63-70.

[52] M.S.Z. Gui, S.A. Jourabchi, H.K. Ng, S. Gan, Comparison of the Yield and Properties of Bio-Oil Produced by Slow and Fast Pyrolysis of Rice Husks and Coconut Shells, 625 (2014) 626-629.

[53] H. Nam, A. Maglinao, S. Capareda, Oxygen gasification and its syngas upgrading in a fluidized-bed reactor using sand mixed dairy manure, (2015).

[54] A. Pattiya, S. Suttibak, Influence of a glass wool hot vapour filter on yields and properties of bio-oil derived from rapid pyrolysis of paddy residues, Bioresour. Technol. 116 (2012) 107-113.

[55] Y. Huang, W. Chen, P. Chiueh, W. Kuan, S. Lo, Microwave torrefaction of rice straw and pennisetum, Bioresour. Technol. 123 (2012) 1-7.

[56] S.S. Lam, R.K. Liew, C.K. Cheng, H.A. Chase, Catalytic microwave pyrolysis of waste engine oil using metallic pyrolysis char, Applied Catalysis B: Environmental. 176 (2015) 601-617.

[57] S.S. Lam, A.D. Russell, H.A. Chase, Pyrolysis using microwave heating: a sustainable process for recycling used car engine oil, Ind Eng Chem Res. 49 (2010) 10845-10851.

[58] S.S. Lam, H.A. Chase, A review on waste to energy processes using microwave pyrolysis, Energies. 5 (2012) 4209-4232.

[59] G. Duman, C. Okutucu, S. Ucar, R. Stahl, J. Yanik, The slow and fast pyrolysis of cherry seed, Bioresour. Technol. 102 (2011) 1869-1878.

[60] A. Ross, J. Jones, M. Kubacki, T. Bridgeman, Classification of macroalgae as fuel and its thermochemical behaviour, Bioresour. Technol. 99 (2008) 6494-6504.

[61] V. Pasangulapati, K.D. Ramachandriya, A. Kumar, M.R. Wilkins, C.L. Jones, R.L. Huhnke, Effects of cellulose, hemicellulose and lignin on thermochemical conversion characteristics of the selected biomass, Bioresour. Technol. 114 (2012) 663-669.

[62] H. Nam, A.L. Maglinao Jr., S.C. Capareda, D.A. Rodriguez-Alejandro, Enriched-air fluidized bed gasification using bench and pilot scale reactors of dairy manure with sand bedding based on response surface methods, Energy. 95 (2016) 187-199.

[63] H. Nam, A.L. Maglinao, S.C. Capareda, Fluidized bed air gasification using low heating value sand-bedded dairy manure and sludge pellets, (2015).

[64] S. Schimmelpfennig, B. Glaser, One step forward toward characterization: some important material properties to distinguish biochars, J. Environ. Qual. 41 (2012) 1001-1013.

[65] J. Rouquerol, F. Rouquerol, P. Llewellyn, G. Maurin, K.S. Sing, Adsorption by Powders and Porous Solids: Principles, Methodology and Applications, Academic press, 2013.

[66] J. Wang, S. Kaskel, KOH activation of carbon-based materials for energy storage, Journal of Materials Chemistry. 22 (2012) 23710-23725.

[67] A. Ahmadpour, D. Do, The preparation of active carbons from coal by chemical and physical activation, Carbon. 34 (1996) 471-479.

[68] J. Maciá-Agulló, B. Moore, D. Cazorla-Amorós, A. Linares-Solano, Activation of coal tar pitch carbon fibres: physical activation vs. chemical activation, Carbon. 42 (2004) 1367-1370.

[69] F. Rodríguez-Reinoso, Production and applications of activated carbons, Handbook of porous solids. (2002) 1766-1827.

[70] J.R. Baseri, P. Palanisamy, P. Sivakumar, Preparation and characterization of activated carbon from Thevetia peruviana for the removal of dyes from textile waste water, Adv.Appl.Sci.Res. 3 (2012) 377-383.

[71] T. Otowa, R. Tanibata, M. Itoh, Production and adsorption characteristics of MAXSORB: high-surface-area active carbon, Gas separation & purification. 7 (1993) 241-245.

[72] E. Raymundo-Piñero, P. Azaïs, T. Cacciaguerra, D. Cazorla-Amorós, A. Linares-Solano, F. Béguin, KOH and NaOH activation mechanisms of multiwalled carbon nanotubes with different structural organisation, Carbon. 43 (2005) 786-795.

[73] T. Adinaveen, L.J. Kennedy, J.J. Vijaya, G. Sekaran, Surface and porous characterization of activated carbon prepared from pyrolysis of biomass (rice straw) by two-stage procedure and its applications in supercapacitor electrodes, Journal of Material Cycles and Waste Management. 17 (2015) 736-747.

[74] S. Hwang, W.M. Choi, S.K. Lim, Hydrogen storage characteristics of carbon fibers derived from rice straw and paper mulberry, Mater Lett. 167 (2016) 18-21.

[75] E.Y.L. Teo, L. Muniandy, E. Ng, F. Adam, A.R. Mohamed, R. Jose, K.F. Chong, High surface area activated carbon from rice husk as a high performance supercapacitor electrode, Electrochim. Acta. 192 (2016) 110-119.

[76] R. Gottipati, Preparation and Characterization of Microporous Activated Carbon from Biomass and its Application in the Removal of Chromium (VI) from Aqueous Phase. (2012).

[77] C.T. Yavuz, J.T. Mayo, W.W. Yu, A. Prakash, J.C. Falkner, S. Yean, L. Cong, H.J. Shipley, A. Kan, M. Tomson, D. Natelson, V.L. Colvin, Low-field magnetic separation of monodisperse Fe3O4 nanocrystals, Science. 314 (2006) 964-967.

[78] de Luna, Mark Daniel G, E.D. Flores, D.A.D. Genuino, C.M. Futalan, M. Wan, Adsorption of Eriochrome Black T (EBT) dye using activated carbon prepared from waste rice hulls—Optimization, isotherm and kinetic studies, Journal of the Taiwan Institute of Chemical Engineers. 44 (2013) 646-653.

[79] A. Mashayekh-Salehi, G. Moussavi, Removal of acetaminophen from the contaminated water using adsorption onto carbon activated with NH4Cl, Desalination and Water Treatment. (2015) 1-13.

[80] H. Liu, W. Ning, P. Cheng, J. Zhang, Y. Wang, C. Zhang, Evaluation of animal hairs-based activated carbon for sorption of norfloxacin and acetaminophen by comparing with cattail fiber-based activated carbon, J. Anal. Appl. Pyrolysis. 101 (2013) 156-165.

[81] A.S. Mestre, J. Pires, J.M.F. Nogueira, A.P. Carvalho, Activated carbons for the adsorption of ibuprofen, Carbon. 45 (2007) 1979-1988.

[82] E. Frackowiak, F. Béguin, Carbon materials for the electrochemical storage of energy in capacitors, Carbon. 39 (2001) 937-950.

[83] Y. Hu, H. Liu, Q. Ke, J. Wang, Effects of nitrogen doping on supercapacitor performance of a mesoporous carbon electrode produced by a hydrothermal soft-templating process, Journal of Materials Chemistry A. 2 (2014) 11753-11758.

[84] L. Wei, M. Sevilla, A.B. Fuertes, R. Mokaya, G. Yushin, Hydrothermal Carbonization of Abundant Renewable Natural Organic Chemicals for High-Performance Supercapacitor Electrodes, Advanced Energy Materials. 1 (2011) 356-361.

[85] X. Li, C. Han, X. Chen, C. Shi, Preparation and performance of straw based activated carbon for supercapacitor in non-aqueous electrolytes, Microporous and Mesoporous Materials. 131 (2010) 303-309.

[86] D. Bhattacharjya, J. Yu, Activated carbon made from cow dung as electrode material for electrochemical double layer capacitor, J. Power Sources. 262 (2014) 224-231.

[87] D. Kalpana, S. Cho, S. Lee, Y. Lee, R. Misra, N. Renganathan, Recycled waste paper—A new source of raw material for electric double-layer capacitors, J. Power Sources. 190 (2009) 587-591.

[88] Q. Zhang, J. Chang, T. Wang, Y. Xu, Review of biomass pyrolysis oil properties and upgrading research, Energy conversion and management. 48 (2007) 87-92.

[89] D. Mohan, C.U. Pittman, P.H. Steele, Pyrolysis of wood/biomass for bio-oil: a critical review, Energy Fuels. 20 (2006) 848-889.

[90] J.P. Diebold, A Review of the Chemical and Physical Mechanisms of the Storage Stability of Fast Pyrolysis Bio-Oils, National Renewable Energy Laboratory Golden, CO, 2000.

[91] P. Grange, E. Laurent, R. Maggi, A. Centeno, B. Delmon, Hydrotreatment of pyrolysis oils from biomass: reactivity of the various categories of oxygenated compounds and preliminary techno-economical study, Catalysis today. 29 (1996) 297-301.

[92] A. Bridgewater, Advances in thermochemical biomass conversion, (1994).

[93] J.A. Capunitan, S.C. Capareda, Characterization and separation of corn stover bio-oil by fractional distillation, Fuel. 112 (2013) 60-73.

[94] A. Oasmaa, E. Kuoppala, Fast pyrolysis of forestry residue. 3. Storage stability of liquid fuel, Energy Fuels. 17 (2003) 1075-1084.

[95] P.M. Mortensen, J. Grunwaldt, P.A. Jensen, K. Knudsen, A.D. Jensen, A review of catalytic upgrading of bio-oil to engine fuels, Applied Catalysis A: General. 407 (2011) 1-19.

[96] F. de Miguel Mercader, M.J. Groeneveld, S.R. Kersten, C. Geantet, G. Toussaint, N.W. Way, C.J. Schaverien, K.J. Hogendoorn, Hydrodeoxygenation of pyrolysis oil fractions: process understanding and quality assessment through co-processing in refinery units, Energy & Environmental Science. 4 (2011) 985-997.

[97] P.J. de Wild, W.J.J. Huijgen, H.J. Heeres, Pyrolysis of wheat straw-derived organosolv lignin, J. Anal. Appl. Pyrolysis. 93 (2012) 95-103.

[98] G.W. Huber, A. Corma, Synergies between Bio-and Oil Refineries for the Production of Fuels from Biomass, Angewandte Chemie International Edition. 46 (2007) 7184-7201.

[99] J. Wildschut, F.H. Mahfud, R.H. Venderbosch, H.J. Heeres, Hydrotreatment of fast pyrolysis oil using heterogeneous noble-metal catalysts, Ind Eng Chem Res. 48 (2009) 10324-10334.

[100] N. Muradov, B. Fidalgo, A.C. Gujar, N. Garceau, A. T-Raissi, Production and characterization of Lemna minor bio-char and its catalytic application for biogas reforming, Biomass Bioenergy. 42 (2012) 123-131.

[101] Y. Wang, J. Sun, H. Zhang, Z. Chen, X. Lin, S. Zhang, W. Gong, M. Fan, In-situ catalyzing gas conversion using char as a catalyst/support during brown coal gasification, Energy Fuels. (2015).

[102] J.G. Speight, Handbook of Petroleum Product Analysis in Chapter 6 Page 105, John Wiley & Sons, 2015.

[103] USDA, Dairy 2007: Facility Characteristics and Cow Comfort on U.S. Dairy Operations, 2014 (2010).

[104] K.N. Galvão, O. Eizenberg, Comparing Waterbeds and Sand Beds for Cows: A Study at the UF/IFAS Dairy Unit, VM194 (2013).

[105] A. Wedel, Sand-Manure Separation for Anaerobic Digestion Pretreatment, (2014).

[106] C.H. Burton, The potential contribution of separation technologies to the management of livestock manure, Livestock Science. 112 (2007) 208-216.

[107] A.W. Wedel, Method and apparatus for the separation of manure and sand. (1999).

[108] D. DeWaard, Systems and methods for extracting sand from raw slurry material, Systems and methods for extracting sand from raw slurry material. (2013).

[109] M.B. Vanotti, J.M. Rice, A. Ellison, P. Hunt, F. Humenik, C. Baird, Solid-liquid separation of swine manure with polymer treatment and sand filtration, Trans. ASAE. 48 (2005) 1567-1574.

[110] R.W. Bryers, Fireside slagging, fouling, and high-temperature corrosion of heat-transfer surface due to impurities in steam-raising fuels, Progress in energy and combustion science. 22 (1996) 29-120.

[111] D. Vamvuka, D. Zografos, Predicting the behaviour of ash from agricultural wastes during combustion, Fuel. 83 (2004) 2051-2057.

[112] T.R. Miles, T.R. Miles Jr, L.L. Baxter, R.W. Bryers, B.M. Jenkins, L.L. Oden, Boiler deposits from firing biomass fuels, Biomass Bioenergy. 10 (1996) 125-138.

[113] A.L. Maglinao Jr, S. Capareda, Predicting Fouling and Slagging Behavior of Dairy Manure (DM) and Cotton Gin Trash (CGT) During Thermal Conversion, Transactions of the ASABE. 53 (2010) 903-909.

[114] A.L. Maglinao Jr, Development of a Segregated Municipal Solid Waste Gasification System for Electrical Power Generation, TEXAS A&M UNIVERSITY, 2013.

[115] ASME Research Committee on Corrosion and Deposits from Combustion Gases, E. Winegartner, Coal fouling and slagging parameters, (1974).

[116] D. Bapat, S. Kulkarni, V. Bhandarkar, Design and operating experience on fluidized bed boiler burning biomass fuels with high alkali ash. (1997).

[117] Y. Niu, Y. Zhu, H. Tan, S. Hui, Z. Jing, W. Xu, Investigations on biomass slagging in utility boiler: Criterion numbers and slagging growth mechanisms, Fuel Process Technol. 128 (2014) 499-508.

[118] H. Nam, S. Capareda, Experimental investigation of torrefaction of two agricultural wastes of different composition using RSM (response surface methodology), Energy. 91 (2015) 507-516.

[119] J.A. Capunitan, S.C. Capareda, Assessing the potential for biofuel production of corn stover pyrolysis using a pressurized batch reactor, Fuel. 95 (2012) 563-572.

[120] D.F. Jacobs, V.R. Timmer, Fertilizer-induced changes in rhizosphere electrical conductivity: relation to forest tree seedling root system growth and function, New Forests. 30 (2005) 147-166.

[121] B. Phillion, W. Bunting, Growth of spruce seedlings at various soluble fertilizer salt levels, Tree Planters' Notes. 34 (1983) 31-33.

[122] M. Beauregard, M. Gauthier, C. Hamel, T. Zhang, T. Welacky, C. Tan, M. St-Arnaud, Various forms of organic and inorganic P fertilizers did not negatively affect soil-and root-inhabiting AM fungi in a maize–soybean rotation system, Mycorrhiza. 23 (2013) 143-154.

[123] Y. Niu, H. Tan, S. Hui, Ash-related issues during biomass combustion: Alkali-induced slagging, silicate melt-induced slagging (ash fusion), agglomeration, corrosion, ash utilization, and related countermeasures, Progress in Energy and Combustion Science. 52 (2016) 1-61.

[124] Y. Hu, S. Cheng, P. Sun, J. Xie, H. Zhang, Research on fusion behavior of ash from mixedly burning biomass with coal, Thermal Power Generation. 40 (2011) 8-12.

[125] H. Liu, Y. Feng, S. Wu, D. Liu, The role of ash particles in the bed agglomeration during the fluidized bed combustion of rice straw, Bioresour. Technol. 100 (2009) 6505-6513.

[126] H.J.M. Visser, The Influence of Fuel Composition on Agglomeration Behaviour in Fluidised-Bed Combustion, Energy research Centre of the Netherlands ECN Delft, 2004.

[127] B. Goodrich, S. Mukhtar, S. Capareda, Characterization and transport analysis of dairy biomass for co-firing in coal-based power plants. ASABE Paper No. 084068, St.Joseph.Mich.: ASABE. (2008).

[128] S. Capareda, S. Mukhtar, C. Engler, L. Goodrich, Energy usage survey of dairies in the Southwestern United States, Appl. Eng. Agric. 26 (2010) 667-675.

[129] A. Ghaly, A comparative study of anaerobic digestion of acid cheese whey and dairy manure in a two-stage reactor, Bioresour. Technol. 58 (1996) 61-72.

[130] G. Gordillo, K. Annamalai, Adiabatic fixed bed gasification of dairy biomass with air and steam, Fuel. 89 (2010) 384-391.

[131] S.S. Thanapal, K. Annamalai, J.M. Sweeten, G. Gordillo, Fixed bed gasification of dairy biomass with enriched air mixture, Appl. Energy. 97 (2012) 525-531.

[132] H. Wu, M.A. Hanna, D.D. Jones, Fluidized-bed gasification of dairy manure by Box-Behnken design, Waste Manag. Res. 30 (2012) 506-511.

[133] IMERYS Refractory Minerals, Mulgrain® Grains and Flours, (2015).

[134] J. Wang, G. Cheng, Y. You, B. Xiao, S. Liu, P. He, D. Guo, X. Guo, G. Zhang, Hydrogen-rich gas production by steam gasification of municipal solid waste (MSW) using NiO supported on modified dolomite, Int J Hydrogen Energy. 37 (2012) 6503-6510.

[135] I. Narvaez, A. Orio, M.P. Aznar, J. Corella, Biomass gasification with air in an atmospheric bubbling fluidized bed. Effect of six operational variables on the quality of the produced raw gas, Ind Eng Chem Res. 35 (1996) 2110-2120.

[136] S. Chamoli, ANN and RSM approach for modeling and optimization of designing parameters for a V down perforated baffle roughened rectangular channel, Alexandria Engineering Journal. in press (2015).

[137] F. Vejahati, H. Katalambula, R. Gupta, Entrained-flow gasification of oil sand coke with coal: Assessment of operating variables and blending ratio via response surface methodology, Energy Fuels. 26 (2011) 219-232.

[138] L. Han, Q. Wang, Y. Yang, C. Yu, M. Fang, Z. Luo, Hydrogen production via CaO sorption enhanced anaerobic gasification of sawdust in a bubbling fluidized bed, Int J Hydrogen Energy. 36 (2011) 4820-4829.

[139] J. Gil, M.P. Aznar, M.A. Caballero, E. Francés, J. Corella, Biomass gasification in fluidized bed at pilot scale with steam-oxygen mixtures. Product distribution for very different operating conditions, Energy Fuels. 11 (1997) 1109-1118.

[140] E. Azzone, M. Morini, M. Pinelli, Development of an equilibrium model for the simulation of thermochemical gasification and application to agricultural residues, Renewable Energy. 46 (2012) 248-254.

[141] K.P. Raman, W.P. Walawender, L. Fan, Gasification of feedlot manure in a fluidized bed reactor. The effect of temperature, Industrial & Engineering Chemistry Process Design and Development. 19 (1980) 623-629.

[142] Z. Zainal, A. Rifau, G. Quadir, K. Seetharamu, Experimental investigation of a downdraft biomass gasifier, Biomass Bioenergy. 23 (2002) 283-289.

[143] J. Gil, J. Corella, M.P. Aznar, M.A. Caballero, Biomass gasification in atmospheric and bubbling fluidized bed: effect of the type of gasifying agent on the product distribution, Biomass Bioenergy. 17 (1999) 389-403.

[144] J. Herguido, J. Corella, J. Gonzalez-Saiz, Steam gasification of lignocellulosic residues in a fluidized bed at a small pilot scale. Effect of the type of feedstock, Ind Eng Chem Res. 31 (1992) 1274-1282.

[145] T. Jayah, L. Aye, R. Fuller, D. Stewart, Computer simulation of a downdraft wood gasifier for tea drying, Biomass Bioenergy. 25 (2003) 459-469.

[146] H. Ghassemi, R. Shahsavan-Markadeh, Effects of various operational parameters on biomass gasification process; a modified equilibrium model, Energy Conversion and Management. 79 (2014) 18-24.

[147] A. Shah, R. Srinivasan, S. D Filip To, E.P. Columbus, Performance and emissions of a spark-ignited engine driven generator on biomass based syngas, Bioresour. Technol. 101 (2010) 4656-4661.

[148] S.C. Capareda, Introduction to Biomass Energy Conversions, CRC Press, Taylor & Francis, Boca Raton, Florida, 2014.

[149] Y. Zhang, A. Ghaly, B. Li, Physical properties of corn residues, American Journal of Biochemistry and Biotechnology. 8 (2012) 44.

[150] W.J. Hill, W.G. Hunter, A Review of Response Surface Methodology: A Literature Survey, Technometrics. 8 (1966) 571-590.

[151] N. Worasuwannarak, T. Sonobe, W. Tanthapanichakoon, Pyrolysis behaviors of rice straw, rice husk, and corncob by TG-MS technique, J. Anal. Appl. Pyrolysis. 78 (2007) 265-271.

[152] G. Chen, D. Leung, Experimental investigation of biomass waste,(rice straw, cotton stalk, and pine sawdust), pyrolysis characteristics, Energy Sources. 25 (2003) 331-337.

[153] K. Ragland, D. Aerts, A. Baker, Properties of wood for combustion analysis, Bioresour. Technol. 37 (1991) 161-168.

[154] A. Ross, J. Jones, M. Kubacki, T. Bridgeman, Classification of macroalgae as fuel and its thermochemical behaviour, Bioresour. Technol. 99 (2008) 6494-6504.

[155] A. Sluiter, B. Hames, R. Ruiz, C. Scarlata, J. Sluiter, D. Templeton, D. Crocker, Determination of structural carbohydrates and lignin in biomass, Laboratory analytical procedure. (2008).

[156] G. Garrote, H. Domínguez, J.C. Parajó, Autohydrolysis of corncob: study of non-isothermal operation for xylooligosaccharide production, J. Food Eng. 52 (2002) 211-218.

[157] B.C. Saha, Hemicellulose bioconversion, Journal of Industrial Microbiology and Biotechnology. 30 (2003) 279-291.

[158] J.S. Bak, J.K. Ko, I. Choi, Y. Park, J. Seo, K.H. Kim, Fungal pretreatment of lignocellulose by Phanerochaete chrysosporium to produce ethanol from rice straw, Biotechnol. Bioeng. 104 (2009) 471-482.

[159] C. Ververis, K. Georghiou, N. Christodoulakis, P. Santas, R. Santas, Fiber dimensions, lignin and cellulose content of various plant materials and their suitability for paper production, Industrial Crops and Products. 19 (2004) 245-254.

[160] P. Binod, M. Kuttiraja, M. Archana, K.U. Janu, R. Sindhu, R.K. Sukumaran, A. Pandey, High temperature pretreatment and hydrolysis of cotton stalk for producing sugars for bioethanol production, Fuel. 92 (2012) 340-345.

[161] P. Bergman, A. Boersma, R. Zwart, J. Kiel, Torrefaction for biomass co-firing in existing coal-fired power stations, Energy Centre of Netherlands, Report No.ECN-C-05-013. (2005).

[162] H. Yang, R. Yan, H. Chen, D.H. Lee, C. Zheng, Characteristics of hemicellulose, cellulose and lignin pyrolysis, Fuel. 86 (2007) 1781-1788.

[163] G. Wang, Y. Luo, J. Deng, J. Kuang, Y. Zhang, Pretreatment of biomass by torrefaction, Chinese Science Bulletin. 56 (2011) 1442-1448.

[164] G.N. Inari, M. Petrissans, P. Gerardin, Chemical reactivity of heat-treated wood, Wood Sci. Technol. 41 (2007) 157-168.

[165] J. Shankar Tumuluru, S. Sokhansanj, J.R. Hess, C.T. Wright, R.D. Boardman, REVIEW: A review on biomass torrefaction process and product properties for energy applications, Industrial Biotechnology. 7 (2011) 384-401.

[166] E. Kurkela, P. Ståhlberg, Air gasification of peat, wood and brown coal in a pressurized fluidized-bed reactor. I. Carbon conversion, gas yields and tar formation, Fuel Process Technol. 31 (1992) 1-21.

[167] P. Binod, M. Kuttiraja, M. Archana, K.U. Janu, R. Sindhu, R.K. Sukumaran, A. Pandey, High temperature pretreatment and hydrolysis of cotton stalk for producing sugars for bioethanol production, Fuel. 92 (2012) 340-345.

[168] D. Stewart, G.J. McDougall, A. Baty, Fourier-transform infrared microspectroscopy of anatomically different cells of flax (Linum usitatissimum) stems during development, J. Agric. Food Chem. 43 (1995) 1853-1858.

[169] C.G. Boeriu, D. Bravo, R.J. Gosselink, J.E. van Dam, Characterisation of structure-dependent functional properties of lignin with infrared spectroscopy, Industrial crops and products. 20 (2004) 205-218.

[170] P. Rousset, C. Aguiar, N. Labbé, J. Commandré, Enhancing the combustible properties of bamboo by torrefaction, Bioresour. Technol. 102 (2011) 8225-8231.

[171] Y. Yi, M. Ha, J. Lee, C. Chung, New role of chromium fluoride: its catalytic action on the synthesis of hydroxymethylfurfural in ionic liquid using raw plant biomass and characterization of biomass hydrolysis, Chem. Eng. J. 180 (2012) 370-375.

[172] R.H. White, M. Dietenberger, Wood products: thermal degradation and fire, (2001).

[173] Q. Liu, S. Wang, Y. Zheng, Z. Luo, K. Cen, Mechanism study of wood lignin pyrolysis by using TG–FTIR analysis, J. Anal. Appl. Pyrolysis. 82 (2008) 170-177.

[174] D. Shen, S. Gu, A.V. Bridgwater, Study on the pyrolytic behaviour of xylan-based hemicellulose using TG–FTIR and Py–GC–FTIR, J. Anal. Appl. Pyrolysis. 87 (2010) 199-206.

[175] EIA, T. Bridgwater, Biomass Pyrolysis, Report T34 (2007) 4.

[176] R. Lou, S. Wu, G. Lv, D. Guo, Pyrolytic products from rice straw and enzymatic/mild acidolysis lignin (EMAL), BioResources. 5 (2010) 2184-2194.

[177] C. Song, A. Pawłowski, J. Ji, S. Shan, Y. Cao, Catalytic pyrolysis of rice straw and product analysis, Environ. Prot. Eng. 40 (2014).

[178] S. Li, X. Chen, A. Liu, L. Wang, G. Yu, Study on co-pyrolysis characteristics of rice straw and Shenfu bituminous coal blends in a fixed bed reactor, Bioresour. Technol. 155 (2014) 252-257.

[179] I. Eom, J. Kim, S. Lee, T. Cho, H. Yeo, J. Choi, Comparison of pyrolytic products produced from inorganic-rich and demineralized rice straw (Oryza sativa L.) by fluidized bed pyrolyzer for future biorefinery approach, Bioresour. Technol. 128 (2013) 664-672.

[180] R. Li, Z. Zhong, B. Jin, X. Jiang, C. Wang, A. Zheng, Influence of reaction conditions and red brick on fast pyrolysis of rice residue (husk and straw) in a spout-fluid bed, The Canadian Journal of Chemical Engineering. 90 (2012) 1202-1211.

[181] M. Carrier, T. Hugo, J. Gorgens, H. Knoetze, Comparison of slow and vacuum pyrolysis of sugar cane bagasse, J. Anal. Appl. Pyrolysis. 90 (2011) 18-26.

[182] F. Karaosmanoğlu, E. Tetik, E. Göllü, Biofuel production using slow pyrolysis of the straw and stalk of the rapeseed plant, Fuel Process Technol. 59 (1999) 1-12.

[183] B.S. Santos, Liquid-phase processing of fast pyrolysis bio-oil using platinum/HZSM-5 catalyst, ProQuest Dissertations and Theses. (2013).

[184] Y.J. Bae, C. Ryu, J. Jeon, J. Park, D.J. Suh, Y. Suh, D. Chang, Y. Park, The characteristics of bio-oil produced from the pyrolysis of three marine macroalgae, Bioresour. Technol. 102 (2011) 3512-3520.

[185] M.C.C. Maguyon, S.C. Capareda, Evaluating the effects of temperature on pressurized pyrolysis of< i> Nannochloropsis oculata based on products yields and characteristics, Energy Conversion and Management. 76 (2013) 764-773.

[186] R. Manurung, D.A.Z. Wever, J. Wildschut, R.H. Venderbosch, H. Hidayat, J.E.G. van Dam, E.J. Leijenhorst, A.A. Broekhuis, H.J. Heeres, Valorisation of Jatropha curcas L. plant parts: Nut shell conversion to fast pyrolysis oil, Food Bioprod. Process. 87 (2009) 187-196.

[187] S. Czernik, A. Bridgwater, Overview of applications of biomass fast pyrolysis oil, Energy Fuels. 18 (2004) 590-598.

[188] A.A. Boateng, D.E. Daugaard, N.M. Goldberg, K.B. Hicks, Bench-scale fluidized-bed pyrolysis of switchgrass for bio-oil production, Ind Eng Chem Res. 46 (2007) 1891-1897.

[189] H. Zhang, R. Xiao, H. Huang, G. Xiao, Comparison of non-catalytic and catalytic fast pyrolysis of corncob in a fluidized bed reactor, Bioresour. Technol. 100 (2009) 1428-1434.

[190] C. Wang, Z. Du, J. Pan, J. Li, Z. Yang, Direct conversion of biomass to bio-petroleum at low temperature, J. Anal. Appl. Pyrolysis. 78 (2007) 438-444.

[191] M. Asadullah, M.A. Rahman, M.M. Ali, M.S. Rahman, M.A. Motin, M.B. Sultan, M.R. Alam, Production of bio-oil from fixed bed pyrolysis of bagasse, Fuel. 86 (2007) 2514-2520.

[192] E. Salehi, J. Abedi, T. Harding, Bio-oil from sawdust: pyrolysis of sawdust in a fixed-bed system, Energy Fuels. 23 (2009) 3767-3772.

[193] R.K. Singh, K.P. Shadangi, Liquid fuel from castor seeds by pyrolysis, Fuel. 90 (2011) 2538-2544.

[194] C. Lievens, D. Mourant, M. He, R. Gunawan, X. Li, C. Li, An FT-IR spectroscopic study of carbonyl functionalities in bio-oils, Fuel. 90 (2011) 3417-3423.

[195] L.J. Bellamy, Advances in Infrared Group Frequencies *The Infra-Red Spectra of Complex Molecules*, 3rd ed., Chapman and Hall; New York: Wiley, London, 1975.

[196] D.W. Mayo, F.A. Miller, R.W. and Hannah, Course Notes on the Interpretation of Infrared and Raman Spectra, John Wiley & Sons: Hoboken, New Jersey, 2004.

[197] M. Asadullah, S. Zhang, C. Li, Evaluation of structural features of chars from pyrolysis of biomass of different particle sizes, Fuel Process Technol. 91 (2010) 877-881.

[198] E.A. Teiseh, S. Capareda, Maximizing the concentrations of hydrogen, carbon monoxide and methane produced from the pyrolysis of a MixAlco process derived sludge, J. Anal. Appl. Pyrolysis. 102 (2013) 76-82.

[199] C.A. Mullen, A.A. Boateng, N.M. Goldberg, I.M. Lima, D.A. Laird, K.B. Hicks, Bio-oil and bio-char production from corn cobs and stover by fast pyrolysis, Biomass Bioenergy. 34 (2010) 67-74.

[200] A. Dutta, M. Talmadge, J. Hensley, M. Worley, D. Dudgeion, D. Barton, P. Groenendijk, D. Ferrari, E.M. Searcy, C.T. Wright, J.R. Hess, Process design and

economics for conversion of lignocellulosic biomass to ethanol -Thermochemical pathway by indirect gasification and mixed alcohol synthesis, Contract. 303 (2011) 275-3000.

[201] S. Capareda, Renewable Energy and Environmental Sustainability Using Biomass from Animal Production Systems
Task-D: Biomass Handling Methods, DE-FG36-05GO85003 (2011).

[202] M.M. El-Halwagi, Sustainable Design through Process Integration, Elsevier, 225 wyman Street, Waltham, MA 02451 USA, 2012.

[203] C. Berrueco, J. Recari, B.M. Güell, G. del Alamo, Pressurized gasification of torrefied woody biomass in a lab scale fluidized bed, Energy. 70 (2014) 68-78.

[204] M.A. Palma, J.W. Richardsonb, B.E. Robersonc, Outlawe, Luis A Riberad Joe, C. Munsterf, Economic feasibility of a mobile fast pyrolysis system for sustainable bio-crude oil production, Supporters and Partners. 14 (2011) 1-16.

[205] EIA, ELECTRICITY DATA BROWSER, 2015 (2015).

[206] A. Tremel, D. Becherer, S. Fendt, M. Gaderer, H. Spliethoff, Performance of entrained flow and fluidised bed biomass gasifiers on different scales, Energy Conversion and Management. 69 (2013) 95-106.

[207] U. Arena, F. Di Gregorio, M. Santonastasi, A techno-economic comparison between two design configurations for a small scale, biomass-to-energy gasification based system, Chem. Eng. J. 162 (2010) 580-590.

[208] T. Kuhlbusch, P. Crutzen, Toward a global estimate of black carbon in residues of vegetation fires representing a sink of atmospheric CO2 and a source of O2, Global Biogeochem. Cycles. 9 (1995) 491-501.

[209] J. Kim, G. Sparovek, R.M. Longo, W.J. De Melo, D. Crowley, Bacterial diversity of terra preta and pristine forest soil from the Western Amazon, Soil Biol. Biochem. 39 (2007) 684-690.

[210] J. Gaskin, C. Steiner, K. Harris, K. Das, B. Bibens, Effect of low-temperature pyrolysis conditions on biochar for agricultural use, Transactions of the ASABE. 51 (2008) 2061-2069.

[211] J. Zhang, K. Yanagisawa, S. Yao, H. Wong, Y. Qiu, H. Zheng, Large-scale controllable preparation and performance of hierarchical nickel microstructures by a seed-mediated solution hydrogen reduction route, Journal of Materials Chemistry A. 3 (2015) 7877-7887.

[212] B. Xing, H. Guo, L. Chen, Z. Chen, C. Zhang, G. Huang, W. Xie, J. Yu, Lignite-derived high surface area mesoporous activated carbons for electrochemical capacitors, Fuel Process Technol. 138 (2015) 734-742.

[213] J.T. Yu, A.M. Dehkhoda, N. Ellis, Development of biochar-based catalyst for transesterification of canola oil, Energy Fuels. 25 (2010) 337-344.

[214] H. Nam, S.C. Capareda, N. Ashwath, J. Kongkasawan, Experimental investigation of pyrolysis of rice straw using bench-scale auger, batch and fluidized bed reactors, Energy. 93, Part 2 (2015) 2384-2394.

[215] W. Wu, M. Yang, Q. Feng, K. McGrouther, H. Wang, H. Lu, Y. Chen, Chemical characterization of rice straw-derived biochar for soil amendment, Biomass Bioenergy. 47 (2012) 268-276.

[216] N. Prakongkep, R.J. Gilkes, W. Wiriyakitnateekul, A. Duangchan, T. Darunsontaya, The Effects of Pyrolysis Conditions on the Chemical and Physical Properties of Rice Husk Biochar, International Journal of Material Science. (2013).

[217] N. Basri, B. Dolah, Physical and electrochemical properties of supercapacitor electrodes derived from carbon nanotube and biomass carbon, Int.J.Electrochem.Sci. 8 (2013) 257-273.

[218] J.A. Capunitan, S.C. Capareda, Hydrotreatment of corn stover bio-oil using noble metal catalysts, Fuel Process Technol. 125 (2014) 190-199.

[219] M. Maguyon, Technical Feasibility Study on Biofuels Production from Pyrolysis of Nannochloropsis oculata and Algal Bio-oil Upgrading, (2013).

[220] S. Vitolo, M. Seggiani, P. Frediani, G. Ambrosini, L. Politi, Catalytic upgrading of pyrolytic oils to fuel over different zeolites, Fuel. 78 (1999) 1147-1159.

[221] X. Bai, P. Duan, Y. Xu, A. Zhang, P.E. Savage, Hydrothermal catalytic processing of pretreated algal oil: a catalyst screening study, Fuel. 120 (2014) 141-149.

[222] D.R. Vardon, B.K. Sharma, H. Jaramillo, D. Kim, J.K. Choe, P.N. Ciesielski, T.J. Strathmann, Hydrothermal catalytic processing of saturated and unsaturated fatty acids to hydrocarbons with glycerol for in situ hydrogen production, Green Chem. 16 (2014) 1507-1520.

[223] S. Ilias, R. Khare, A. Malek, A. Bhan, A descriptor for the relative propagation of the aromatic-and olefin-based cycles in methanol-to-hydrocarbons conversion on H-ZSM-5, Journal of Catalysis. 303 (2013) 135-140.